ABSTRACT

XIAOJUN, MEI. Hyperfast Correlated Dynamics of Radiation Damage and Recovery in Materials. (Under the direction of Dr. Jacob Eapen.)

The response of solid-state materials to radiation is governed through a host of mechanisms that have time scales ranging from femtoseconds to seconds and years. Metastable liquid-like regions that typically last for several picoseconds and more are commonly observed in ultra-fast experiments and simulations. In this investigation, we make quantitative predictions on correlated dynamical motion of the atoms as the liquid-like state is formed and condensed following an ion or neutron impact. Simulations on three materials – copper, silicon and argon – that have very different bond structures reveal an anisotropic and heterogeneous dynamical structure. Of utmost importance are the dynamical correlations during the recovery period, which corresponds to the condensation of the liquid-like state.

Using molecular dynamics simulations and with the appropriate non-equilibrium shock physics formalism, the dynamical metrics of the liquid-like state are evaluated through the density correlator and van Hove self-correlation function, as well as through defect, thermodynamic and hydrodynamic field data, following a confined ion/neutron impact. These correlation functions can also be experimentally accessed or inferred from the state-of-the-art ultrafast pump-probe experimental methods. The hopping mechanism from the van-Hove self-correlation, the fractal-like condensation and the fast decay of the density correlator attest to a rapid defect recovery in copper. In contrast, silicon portrays dynamically heterogeneous regions that resist recovery to the underlying lattice structure, and exhibits a non-decaying density correlator that is strikingly analogous to that of a supercooled liquid.

Ion hammering and pump-probe experiments allude to a liquid-liquid phase transition in silicon – from a high density liquid to a low density liquid – before silicon is amorphized; the inference, however, is based on indirect interpretations. The simulations presented in this dissertation demonstrate a transitioning to a more complex and rich dynamical structure with a fascinating directional anisotropy that is very different from that in quasi-equilibrium conditions. Thus large-scale simulations, as presented in this work, would be of immense value in interpreting the results from experiments performed at ultra/hyperfast timescales.

Lastly, a fundamental understanding of the dynamical attributes of defect recovery is generally unknown; the various defect models currently in use do not account for the dynamical recovery. Insights garnered from our work can however, be advantageously employed in developing realistic models for defect recovery. Although the structural aspects of tolerance of materials to radiation have been elucidated before, the current work throws light on the incipient dynamical interactions that control the structural transformation in a radiation environment.

Hyperfast Correlated Dynamics of Radiation Damage and Recovery in Materials

by
Xiaojun Mei

A dissertation submitted to the Graduate Faculty of
North Carolina State University
in partial fulfillment of the
requirements for the degree of
Doctor of Philosophy

Nuclear Engineering

Raleigh, North Carolina

2013

APPROVED BY:

Dr. Jacob Eapen Chair, Advisory Committee	Dr. K. L. Murty Member, Advisory Committee
Dr. Mohamed Bourham Member, Advisory Committee	Dr. Keith Gubbins Member, Advisory Committee

DEDICATION

To my dear parents.

To my beloved wife, Mengying.

To my lovely son, Daniel.

BIOGRAPHY

Born in Chaohu, China in 1987, Xiaojun Mei received his Bachelor's degree in Physics from the University of Science and Technology, China in 2008. Following his graduation, he joined the Department of Nuclear Engineering at the North Carolina State University in Fall 2008. Since then he has been focusing on molecular simulations of radiation damage and recovery in materials using statistical-mechanical principles under the supervision of Dr. Jacob Eapen. His deep interest in mathematical and statistical methods has motivated him to purse graduate studies in the same area; he received a Master of Science degree in Statistics from the Department of Statistics in 2011. He intends to work in the field of computational and statistical sciences in his professional career.

ACKNOWLEDGEMENTS

At the outset, I would like to express my heartfelt appreciation to Prof. Jacob Eapen for his unstinting support and guidance throughout my graduate studies. He has been very patient and encouraging during the time I spent under his supervision.

I am immensely indebted to my advisory committee members – Prof. K. L. Murty, Prof. Mohamed Bourham and Prof. Keith Gubbins, for their insightful comments and encouragement on my dissertation work.

I would like to record my sincere gratitude to all the members of Prof. Jacob Eapen's RADIANT research group for their support and refreshing sense of optimism. In particular, I would like to thank Dr. Prithwish Nandi, who assisted me on defect analysis and for reviewing part of my PhD dissertation. It was a great pleasure to share the stimulating company of Dr. Walid Mohamed, Ajay Annamareddy, Anant Raj, Jin Wang and William Lowe.

My sincere appreciation goes to all who helped me at the department – in particular, I want to thank Ms. Ganga Atukorala, Ms. Hermine Kabbendjan and Mr. Robert Green for helping me with the curricular and administrative matters over the last five years.

Finally, I would like to express my love and gratitude to my wife for her kindness, encouragement and consistent support.

TABLE OF CONTENTS

LIST OF FIGURES

Chapter 1. Introduction

Radiation is ubiquitous in nature; it is the most dominant mode of energy transport in the universe. Radiation includes electromagnetic waves or photons, as well as particles with finite rest mass such as electrons, ions and neutrons. When radiations interact with condensed matter, its atomic structure gets altered. Prolonged exposure to radiation generally results in the formation of macroscale defects that adversely affect the performance of materials. Several energy-related applications where radiation plays an active role are briefly reviewed next.

1.1 Radiation Applications

(i) Nuclear Energy: High energy neutrons, of the order of 1 MeV, are generated from fission process that takes place in the fuel elements of nuclear reactors. Because they are electrically neutral, neutrons have a large mean free path that is of the order of 1 centimeter. Thus fast neutrons escape from the core of the nuclear reactors and interact with the structural elements such as the reactor or pressure vessel and piping units. Over time the structural elements degrade and lose their integrity [1]. The fuel, after its serviceable lifetime in a reactor, is stored as spent fuel, first under water and then in dry storage casks. Because of radioactive decay, the spent fuel matrix is continuously subjected to β radiation from the fission products and α radiation from the actinides. A fundamental understanding of the radiation damage processes and those which aid in recovery or healing is essential to develop radiation and accident tolerant materials for nuclear energy. A comprehensive account of radiation damage in nuclear materials is given in [2].

(ii) Materials Processing: Several materials processing techniques such as pulsed laser deposition (PLD) [3, 4], physical vapor deposition (PVD), plasma and magnetron sputtering [5], focused ion beams [6] and plasma enhanced chemical vapor deposition (PECVD) generate a radiation environment. The materials properties are generally dependent on the interactions of energetic particles (including photons) with the materials surface [6]. Of particular interest, is the ability to manufacture stress-free, defect-free thin films for a variety of applications. It is often desirable and many times required to achieve high deposition rates say, to synthesize thicker films or to speed up production processes. Such processes demand higher energetic fluxes that generally tend to increase the non-uniformities, generate larger debris and considerably degrade the material quality [6]. As

noted by Freund and Suresh [7], attendant residual stresses put a limit on to quality and reliability of thin films even when they are not designed or required to be load-bearing. It therefore, remains a challenge to generate high quality films at a faster rate without the detrimental effects of anisotropy, imperfections and the attendant intrinsic, thermal and interfacial stresses. A fundamental understanding of the energy transfer mechanisms, which can control the surface transport and recombination is thus required [8].

(iii) Solar Energy: Even though energy density from solar radiations is considerably lower than that in nuclear radiations, solar cells are severely tested by rapidly varying and large temperature loads [9]. The highest photovoltaic efficiency (of approximately 35%) has been attained with epitaxially grown compound semiconductor multi-junction structures that collect light across the solar spectrum. However, these compounds are also extremely sensitive to material defects, which are generated during material synthesis as well as from radiation exposure to sun. Solar concentrators, which are designed to operate at temperatures as high as 3000 °C [9, 10], present new materials-related challenges. Space-based solar systems are further bombarded by fluxes of electrons and protons trapped in the electromagnetic field of earth [11, 12]. Thus there is a demonstrated need to discover, design and synthesize new materials for solar energy systems that are intrinsically insensitive to defects [9].

1.2 Dynamical Characteristics of Early Radiation Interactions

As discussed earlier, the response of materials to radiations is governed through several mechanisms that have time scales ranging from femtoseconds to years [8, 13-31]; a schematic is depicted in Fig. 1.1. Metastable liquid-like regions, which typically last for several picoseconds and more, are ubiquitously observed in ultra-fast experiments [32-35] and simulations [13, 16-19, 23, 26-30]. At low fluences, short-pulsed laser irradiation on thin films causes local melting and evaporation followed by ablation at high fluences, which can be described as photomechanical (front surface) spallation [16] or fragmentation [24] – the ejection of large liquid droplets from induced stresses, and phase explosion – the hyperfast decomposition of superheated material into a mixture of vapor and liquid droplets [16]. These mechanisms are regarded to be dependent on the local heat flux, and hence they can occur simultaneously. Heterogeneous and homogeneous melting processes compete depending on the pulse duration [36, 37]. A two-stage melting process is revealed from optical third

harmonic light experiments and molecular dynamics (MD) simulations [29]; in the first stage homogeneous melting takes place, which lasts for few picoseconds, followed by a relatively longer period of 25-30 ps, during which the melt interface propagates into the bulk. Such staggered melt processes are also identified in several molecular simulations [16, 17]. Shock waves are instrumental in the energy transfer – during the incipient isochoric heating from the incident photons, compressive shock waves are generated. On reflection from the free surface the compressive wave becomes a tensile or rarefaction wave that propagates through the melt region and causes cavitation (voids) as well as spallation/fragmentation [16, 17, 28].

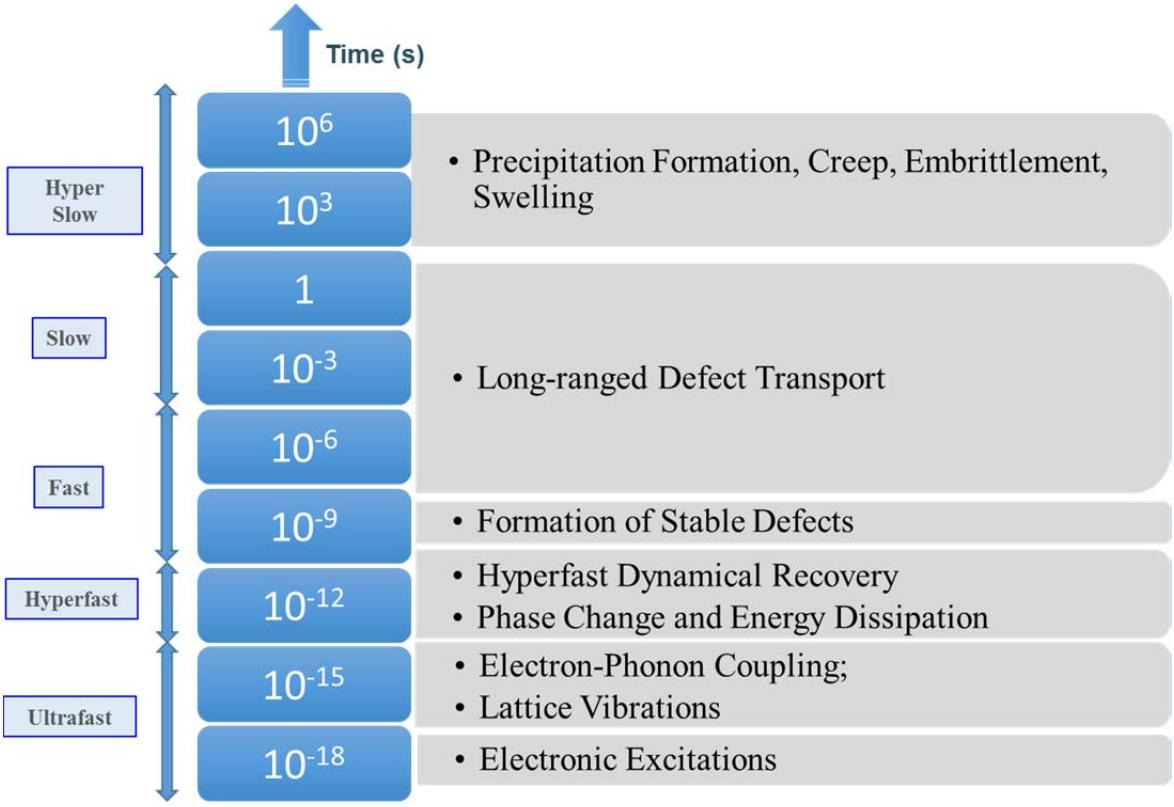

Figure 1.1 Timescales for materials response in a radiation environment. This dissertation focuses on statistical-mechanical analyses of the dynamics during the early interaction processes, which are characterized by phase change, energy dissipation and dynamic defect recovery at the hyperfast timescales.

Ions, neutrons and gamma photons distinguish themselves with their ability to penetrate deeper into the bulk region; fast neutron penetration far exceeds that of the ions and causes significant damage to

fuel and structural elements in nuclear reactors over time. While laser energy is transferred through the electronic excitation and the subsequent electron-phonon coupling, the ions and neutrons can transfer their kinetic energy directly to the nucleus. A two temperature model that explicitly accounts for the ion and electron temperatures, therefore, is typically employed to describe the energy absorption and dissipation processes [16, 25] in laser interactions; the electronic coupling and transport, however, is conveniently neglected for ion and neutron interactions, especially at low energies [38, 39].

Despite the differences in the energy transfer mechanisms, ion and neutron interactions share similar dynamical features to those of the laser interactions. Due to the rather low atomic number density or flux, ions and neutrons interact with one target nuclei at a time generating a three dimensional thermal spike lasting several picoseconds, following an ultrafast ballistic period. In MD simulations, the primary knock-on atom (PKA) mimics the nucleus that absorbs the ion/neutron energy; it transfers the energy to the surrounding atoms through a series of cascading collisions. Thermal spikes, which are created at energies 1 *keV* and higher [21], introduce a superheated disordered region that is often likened to a liquid state, an analogy stemming from the similarities in the structure and diffusional properties of the cascade core region [40]. Induced stresses and morphology changes during the thermal spike period from ion bombardment are attributed to the radiation-induced viscous relaxation in metallic and amorphous thin films [22, 41]. It is now established that the stress evolution is governed by the initial stress state, and there is a competition between tensile and compressive stresses, the former generated by the liquid-like regions and the latter by the accumulation of ion-induced interstitials [13]. Anisotropic diffusion, depending on the stress states, and non-trivial coherent displacement of atoms are also observed in thin films following ion irradiation [13, 42].

1.3 Motivation for Current Research

While the evidence for a metastable liquid-like state is compelling, its dynamical characteristics have not been explored in detail thus far. A liquid state has rich and defining attributes that primarily manifest from strongly correlated dynamics; recent evidence from metastable supercooled liquids portrays an intriguing structural arrest emerging from spatially correlated regions of mobile and immobile atoms, which is defined as dynamical heterogeneity [43]. Much of our current understanding of the early radiation damage processes is gleaned from large scale, non-equilibrium

molecular dynamics (NEMD) simulations. However, most simulations in the past have focused on the formation and identification of defects that arise in a radiation environment. In this work, we make quantitative predictions on correlated dynamical motion of the atoms as the liquid-like state is formed and then condensed following an ion or neutron impact. Of utmost importance are *the dynamical correlations during the recovery period*, which determine the final defected state. The knowledge of the spatio-temporal characteristics immediately following radiation will be immensely valuable in designing accident and radiation tolerant materials for nuclear energy applications as well as for optimizing materials processing methods that use a radiation source.

In recent years, the advances in ultrafast experiments [32-35] allow experimental probing of the disordered dynamical structure at early timescales; however, such techniques are still in the development phase. Since the focus of this dissertation is on the development of time-resolved correlation functions that can describe the liquid-like disordered state following radiation, the key results from this work will be greatly beneficial in interpreting the data generated from the state-of-the-art ultrafast experiments. A fundamental understanding of the phase changes that occur with radiation will also be useful to interpret hyperfast/ultrafast irradiation experiments such as ion hammering that probe liquid-liquid phase transition – a relatively new area of physics.

Chapter 2. Theory

A central focus of the current work is to develop statistical-mechanical analysis methods for describing the materials response following radiation at the hyperfast timescales. This chapter discusses the theory of correlation functions that are used to characterize the dynamical response.

2.1 Liouville Equation

A 6*N*-dimensional phase space can be constructed from the 3*N* spatial coordinates and 3*N* momentum coordinates [44-49] for a system of *N* particles. A point in the phase space completely specifies the microscopic dynamical state and when the phase points become infinitely dense, there will be a continuum of phase points. The distribution function given by [50]

$$f_N(\mathbf{p}_1, \mathbf{p}_2, \dots, \mathbf{p}_N, \mathbf{r}_1, \mathbf{r}_2, \dots, \mathbf{r}_N) \equiv f_N(\mathbf{p}, \mathbf{r}, t) \tag{2.1}$$

describes the fraction of phase points in an infinitesimal element of the phase space. From the conservation property of the distribution function, the evolution equation of the phase points can be expressed as [50]

$$\frac{\partial f_N}{\partial t} = \nabla \cdot (f_N \mathbf{u}) \tag{2.2}$$

where **u** denotes the time derivative of the momenta and spatial coordinates, and is given by

$$\mathbf{u} = (\dot{\mathbf{p}}_1, \dot{\mathbf{p}}_2, \dots, \dot{\mathbf{p}}_N, \dot{\mathbf{r}}_1, \dot{\mathbf{r}}_2, \dots, \dot{\mathbf{r}}_N) \tag{2.3}$$

In a conservative system, the distribution function is a constant along a trajectory in the phase space. Using Hamilton's equations of motion, the following can be derived [50].

$$\dot{\mathbf{p}}_i = -\frac{\partial H_i}{\partial \mathbf{r}_i}, \qquad \dot{\mathbf{r}}_i = \frac{\partial H_i}{\partial \mathbf{p}_i} \tag{2.4}$$

The Liouville equation, which is the evolution of f_N, can be written as [50]

$$\frac{\partial f_N}{\partial t} + \{H, f_N\}_{PB} = 0 \tag{2.5}$$

Where H denotes the Hamiltonian – the sum of the potential and kinetic energies in the absence of external fields, and PB refers to Poisson bracket, which is given by

$$\{H, f_N\}_{PB} \equiv \sum_{j=1}^{N} \frac{\partial H}{\partial \mathbf{p}_j}\frac{\partial f_N}{\partial \mathbf{r}_j} - \frac{\partial H}{\partial \mathbf{r}_j}\frac{\partial f_N}{\partial \mathbf{p}_j} \tag{2.6}$$

The Liouville equation can be also written as [50]

$$\frac{\partial f_N}{\partial t} = -iLf_N \tag{2.7}$$

where L is the Liouville operator, which in Cartesian coordinates is given by

$$L \equiv -i\left[\sum_{k=1}^{N} \frac{\mathbf{p}_k}{m_k} g\nabla_{\mathbf{r}k} + \sum_{k=1}^{N} \mathbf{F}_k g\nabla_{\boldsymbol{p}k}\right] \tag{2.8}$$

where $\nabla_{\mathbf{r}k}$ and $\nabla_{\boldsymbol{p}k}$ are the gradients with respect to spatial and the momentum coordinates respectively. $\mathbf{F}_k$ is total force on the k^{th} particle. The formal solution to the Liouville equation is given by [50]

$$f_N(\mathbf{p}, \mathbf{r}, t) = \mathrm{e}^{-iLt} f_N(\mathbf{p}, \mathbf{r}, 0) \tag{2.9}$$

2.2 Time Correlation Functions

The correlation function of two dynamical variables A and B is given by [51]

$$C_{AB}(t) \equiv \int d\mathbf{\Gamma} f_N^0 B^* e^{iLt} A \equiv \langle A(t)B^* \rangle \tag{2.10}$$

where f_N^0 is the equilibrium distribution function that corresponds to the steady unperturbed equations of motion with no explicit time dependence; the star corresponds to the complex conjugate. Classical time correlations are not dependent on a particular choice of time and hence, they are functions of

only the differences in time – also known as the stationary property. The correlation function can now be written as [51]

$$C_{AB}(t) = \int d\mathbf{\Gamma} f_N^0(\tau) B^* e^{iLt} A \tag{2.11}$$

$$= \int d\mathbf{\Gamma} (e^{-iLt} f_N^0) B^* e^{iLt} A \tag{2.12}$$

$$= \int d\mathbf{\Gamma} f_N^0 (e^{iLt} B^*) \left(e^{iL(t+\tau)} A\right) \tag{2.13}$$

$$= \int d\mathbf{\Gamma} f_N^0 (e^{iLt} B^*) \left(e^{iL(t+\tau)} A\right) \tag{2.14}$$

Without loss of generality, τ can be set to zero. Then the correlation function can be written as

$$C_{AB}(t) \equiv \int d\mathbf{\Gamma} f_N^0 A(t) B(0) \equiv \langle A(t) B(0) \rangle \tag{2.15}$$

where the pointed brackets denote the ensemble average. When the same variable is considered, the resulting expression becomes the auto-correlation function

$$C_{AA}(t) \equiv \int d\mathbf{\Gamma} f_N^0 A(t) A(0) \equiv \langle A(t) A(0) \rangle \tag{2.16}$$

Originally developed by Boltzmann and Maxwell, the ergodic hypothesis postulates an equivalence between the ensemble average and the time average of an observable. It is expressed as

$$C_{AB}(t) \equiv \int d\mathbf{\Gamma} f_N^0 A(t) B(0) \equiv \langle A(t) A(0) \rangle \Leftrightarrow \lim_{t \to \infty} \frac{1}{\tau} \int_0^\infty dt A(t) B(0) \tag{2.17}$$

Time correlation functions have a similar status as that of the partition functions in equilibrium statistical mechanics [50]. The partition function is unique for a particular ensemble but separate time correlations functions exist, which correspond to different non-equilibrium states. Unlike the partition function, time correlation functions – strictly speaking, their mathematical analogue in frequency space – are directly accessible to experiments such as neutron and x-ray scattering [52].

2.2.1 Space-Time Correlation Functions

The density field at a spatial point **r** and at a time *t* can be expressed as [50, 53]

$$\rho(\mathbf{r},t)=\sum_i \delta\big(\mathbf{r}-\mathbf{r}_i(t)\big) \tag{2.18}$$

The above describes the local density in terms of an infinitesimal region of space at **r** measured at time *t*. While the number of atoms entering and leaving the small volume is fluctuating, the total number of atoms in the system is conserved. To describe the fluctuations and structural probabilities from a macroscopic point of view, a density-density time correlation function can be constructed [47, 54, 55]

$$\begin{aligned} G(\mathbf{r},t) &\equiv \frac{1}{\rho}\langle \rho(\mathbf{r},t)\,\rho(\mathbf{0},0)\rangle \\ &= \frac{1}{N}\Big\langle \sum_i \sum_j \delta\big[\mathbf{r}+\mathbf{r}_i(0)-\mathbf{r}_j(t)\big]\Big\rangle \end{aligned} \tag{2.19}$$

The function above is also known as the van Hove correlation function, where δ is the Dirac delta and the angular brackets represent the time average. $G(\mathbf{r},t)$ is a dynamic quantity that is proportional to the probability of an atom being is at position **r** at time *t* given that an atom was at the origin $\mathbf{r}=0$ at initial time $t=0$. van Hove correlation function can be divided into two parts [53]. Terms having $i=j$ give the self-correlation function $G_s(\mathbf{r},t)$ [50], for which the atom at $(\mathbf{r},t)$ is the same atom that occupied at the origin $(\mathbf{r}=0,t=0)$. The terms having $i\neq j$ yield the distinct correlation function $G_d(\mathbf{r},t)$, for which the atom at $(\mathbf{r},t)$ differs from the atom that occupied at the origin $(\mathbf{r}=0,t=0)$. Thus, the van Hove correlation function can be rewritten as [53]

$$G(\mathbf{r},t)=G_s(\mathbf{r},t)+G_d(\mathbf{r},t) \tag{2.20}$$

The self-correlation function, also known as van Hove self-correlation function, is formally defined as

$$G_s(\mathbf{r},t)=\frac{1}{N}\Big\langle \sum_{j=i} \delta\big[\mathbf{r}+\mathbf{r}_j(0)-\mathbf{r}_j(t)\big]\Big\rangle \tag{2.21}$$

At each instant, normalization gives [50]

$$\int G_s(\mathbf{r},t)d\mathbf{r} = 1 \tag{2.22}$$

At long times and large distances, the position of an atom is unrelated to its original position and therefore, the atom is equally probable to be found anywhere in the system. From the above normalization we can find the value G_s which is seen to collapse from δ (at $t = 0$) to zero. During this period, the shape of self–van Hove correlation function may be assumed as Gaussian-like (under equilibrium conditions). We shall discuss more on the variation of the shapes of van Hove correlation function in the later chapters of this dissertation.

The distinct correlation function, also known as the distinct van Hove correlation function, is defined as [50, 53]

$$G_d(\mathbf{r},t) = \frac{1}{N}\langle \sum_i \sum_{j\neq i} \delta[\mathbf{r} + \mathbf{r}_j(0) - \mathbf{r}_i(t)]\rangle \tag{2.23}$$

The normalization is given by

$$\frac{1}{N}\int G_d(\mathbf{r},t)d\mathbf{r} = 1 - \frac{1}{N} \tag{2.24}$$

$G_d(\boldsymbol{r},0)$ is proportional to the radial distribution function and given by [53]

$$G_d(\boldsymbol{r},0) = \rho g(\boldsymbol{r}) \tag{2.25}$$

At long times and large separations when the position of one atom is unrelated to the earlier position of another atom [53]

$$\lim_{\boldsymbol{r}\to\infty} G_d(\boldsymbol{r},t) = \lim_{t\to\infty} G_d(\boldsymbol{r},t) = \rho \tag{2.26}$$

In the analysis of radiation dynamics, we employ van Hove self-correlation function as a metric to monitor the dynamical characteristics of the formation of disordered zones and the dynamical recovery to a defected state. It is well-known that $G_s(\mathbf{r},t)$ is related to the self-diffusion of the atoms [52]; very recently, however, it has been established that $G_s(\mathbf{r},t)$ is a reliable indicator for dynamical heterogeneity (DH) [60] – the manifestation of spatially correlated regions of mobile and immobile

atoms in highly frustrated states, typically associated with glassy and supercooled systems [43, 56-59]. Interestingly, the exponential decay in $G_s(\mathbf{r},t)$ – the signature for the presence of faster moving atoms – is also observed in jammed conditions such as in granular media, as well as in foams and colloids [60, 61]. Thus, time-resolved $G_s(\mathbf{r},t)$ is an excellent metric to assess whether materials deform and recover in a dynamically heterogeneous manner under radiation.

2.2.2 Correlators in Reciprocal Space

It is often necessary to focus attention on the correlation functions in the reciprocal space. The density correlator, which is defined as the spatial Fourier transform of the van Hove correlation function, is given by [47, 53, 55].

$$F(\mathbf{k},t) = \int G(\mathbf{r},t)\exp(-i\mathbf{k}\cdot\mathbf{r})\,d\mathbf{r} \tag{2.27}$$

The above expression, also known as the intermediate scattering function, is equivalent to the correlation between the number density at time t and that at time origin $t = 0$ [53, 55]:

$$F(\mathbf{k},t) = \frac{1}{N}\langle\rho(\mathbf{k},t)\rho(-\mathbf{k},0)\rangle \tag{2.28}$$

The density correlator is experimentally accessible through neutron and x-ray scattering experiments; it measures the dynamical structure at different wave vectors. Both structure and dynamics can be gleaned through the density correlator – the former gives the details of the position of atoms/defects while the latter gives information on the mobility of atoms/defects that is critical to quantifying the recovery stage following radiation. The density correlator can be evaluated, in principle, from time-resolved ultrafast pump-probe experimental methods [32, 62]. Our investigations, therefore, quantify a metric that can be experimentally accessed, and they would also serve in interpreting results from ultrafast experiments.

A temporal Fourier transform of $F(\mathbf{k},t)$ results in the dynamic structure factor $S(\mathbf{k},\omega)$ as shown next [53, 55].

$$S(\mathbf{k},\omega) = \frac{1}{2\pi}\int_{-\infty}^{\infty} F(\mathbf{k},t)\exp(i\omega t)\,dt \tag{2.29}$$

The static structure factor $S(\mathbf{k})$ can be obtained from the integration of $S(\mathbf{k},\omega)$ over all frequencies as shown by [53]

$$S(\mathbf{k}) = \int_{-\infty}^{\infty} S(\mathbf{k},\omega)d\omega = F(\mathbf{k},0) \tag{2.30}$$

Similarly, from the spatial Fourier transform of the self–van Hove correlation function, the self-density correlator [47] can be obtained.

$$F_s(\mathbf{k},t) = \int G_s(\mathbf{r},t)\exp(-i\mathbf{k}\cdot\mathbf{r})\,d\mathbf{r} \tag{2.31}$$

The formal definition of $F_s(\mathbf{k},t)$ is the sum of the correlations between number density of one atom at time *t* and that at time origin over all atoms

$$F_s(\mathbf{k},t) = \frac{1}{N}\langle\sum_i \rho_i(\mathbf{k},t)\rho_i(-\mathbf{k},0)\rangle \tag{2.32}$$

where, $\rho_i(\mathbf{k},t) = \exp(-i\mathbf{k}\cdot\mathbf{r}_i(t))$ (2.33)

At $t = 0$, $F_s(\mathbf{k},0) = 1$, due to the fact that all atoms are located at their original positions. The self-dynamic structure factor $S_s(\mathbf{k},\omega)$, which is defined as the temporal Fourier transform of the self-density correlator, is given by

$$S_s(\mathbf{k},\omega) = \frac{1}{2\pi}\int_{-\infty}^{\infty} F_s(\mathbf{k},t)\exp(i\omega t)\,dt \tag{2.34}$$

Similar to the definition for the density correlator, an energy correlation function can be defined as

$$E(\mathbf{k},t) = \frac{1}{N}\langle\sum_i\sum_j E_iE_j\exp\big(i\mathbf{k}\cdot[\mathbf{r}_i(t)-\mathbf{r}_j(0)]\big)\rangle \tag{2.35}$$

where E_i is the sum of kinetic and potential energy of an atom *i*. This correlation function has been employed to assess the crossovers in supercooled silicon [63].

2.3 Non-Equilibrium Microscopic Thermodynamic Variables and Fluxes

In the simulations of radiation cascades, a momentum impulse on a primary knock-on atom (PKA) introduces a highly non-equilibrium shock-like environment. Thermodynamic variables and fluxes are evaluated in local regions of the simulation system and they are measured in a co-moving frame – a local frame of reference that is moving with the local macroscopic shock velocity [64-67]. For any sub-region k, the macroscopic temperature is given by

$$T^k = \frac{1}{3N^k k_B} \sum_{i=1}^{N^k} m_i [\mathbf{u}_i - \langle \mathbf{v} \rangle^k]^2 \tag{2.36}$$

where T and N are the temperature and the number of atoms in sub-region k, respectively, k_B is the Boltzmann constant, and $\mathbf{u}_i$ is the velocity of atom i in sub-region k. The average macroscopic velocity $\mathbf{v}$ of the sub-region k is determined as

$$\langle \mathbf{v} \rangle^k = \frac{1}{N} \sum_{i=1}^{N_k} \mathbf{u}_i \tag{2.37}$$

The macroscopic pressure in the sub-region k is given by

$$P^k = \frac{1}{3V^k} \sum_{i=1}^{N^k} \left(m_i \left| \mathbf{u}_i - \langle \mathbf{v} \rangle^k \right|^2 + \sum_{j>i}^{N^k} \mathbf{f}_{ij} \mathbf{r}_{ij} \right) \tag{2.38}$$

where V^k is the volume of the sub-region k, and $\mathbf{f}_{ij}$ and $\mathbf{r}_{ij}$ are the pairwise force and distance vector between two atoms, i and j, respectively. The mass ($\mathbf{J}_m$), momentum ($\mathbf{J}_p$) and heat ($\mathbf{J}_q$) fluxes, analogously, are evaluated as

$$\mathbf{J}_m^k = \frac{1}{N^k} \sum_{i=1}^{N^k} m_i \left(\mathbf{u}_i - \langle \mathbf{v} \rangle^k \right) \tag{2.39}$$

$$\mathbf{J}_p^k = \frac{1}{N^k} \sum_{i=1}^{N^k} m_i \mathbf{u}_i \left(\mathbf{u}_i - \langle \mathbf{v} \rangle^k \right) \tag{2.40}$$

$$\mathbf{J}_q^k = \frac{1}{V^k}\sum_{j=1}^{N^k}\left[e_j\left(\mathbf{u}_j - \langle\mathbf{v}\rangle^k\right) + \sum_{j>i}^{N^k}\mathbf{r}_{ij}\left(\mathbf{f}_{ij}\cdot\left[\mathbf{u}_j - \langle\mathbf{v}\rangle^k\right]\right)\right] \tag{2.41}$$

where e_j is the sum of the kinetic and potential energy of an atom j. Additional smoothening of the thermodynamic and field variables [65] can be performed through kernel and statistical estimators; however, bin or sub-region averaging has been observed to be adequate for extracting the field information with sufficient smoothness. While the kinetic energy and the momentum of an atom can be uniquely defined, the potential energy can only be defined for a system of atoms. We assume that the potential energy can be represented pairwise, and it is shared among the two atoms. While there is no rigorous justification, the pair-wise partitioning is useful for the microscopic theoretical development.

Equations (2.36)-(2.41) assume the Boltzmann equipartition of energy. At very short times, following the radiation impact, i.e., at extreme non-equilibrium conditions, the equipartition does not hold true. Thus even scalar quantities such as temperature will have directional dependence [67-71]. The components of the temperature and pressure tensors in the sub-region k are given by

$$T_{\alpha\alpha}^k = \frac{1}{N^k k_B}\sum_{i=1}^{N^k} m_i[u_i^\alpha - \langle v_\alpha\rangle^k]^2 \qquad \alpha = \{x, y, z\} \tag{2.42}$$

where α denotes a specific direction. The total temperature is defined as one third of the trace, which is expressed as

$$T^k = \frac{1}{3}\left(T_{xx}^k + T_{yy}^k + T_{zz}^k\right) \tag{2.43}$$

The pressure tensor components and the scalar pressure in the sub-region k are given by

$$P_{\alpha\beta}^k = \frac{1}{V^k}\sum_{i=1}^{N^k}\left(m_i\left(u_i^\alpha - \langle v_\alpha\rangle^k\right)\left(u_i^\beta - \langle v_\beta\rangle^k\right) + \sum_{j>i}^{N^k} f_{ij}^\alpha r_{ij}^\beta\right) \quad \alpha, \beta = \{x, y, z\} \tag{2.44}$$

$$P^k = \frac{1}{3}\left(P_{xx}^k + P_{yy}^k + P_{zz}^k\right) \tag{2.45}$$

Chapter 3. Molecular Dynamics (MD) Simulations

In this chapter, the underpinning and nuances of non-equilibrium molecular dynamics simulations for investigating the early stages of radiation interactions are discussed.

3.1 Introduction

The molecular dynamics (MD) simulation method is one of the most widely used computer-based simulation techniques to investigate the properties of materials [72-74]. Using MD simulations, one can perform numerical thought experiments that mimic realistic conditions. The advantage of such an approach is that it is possible to perform many experiments by simply changing the initial conditions/parameters; it is also possible to simulate extreme conditions such as a neutron impact. Using MD simulations, one can obtain the temporal evolution of the trajectory of a many-body system acting under an inter-atomic potential. The method is deterministic in nature, which means that it is possible to compute the trajectory of a system if all the initial conditions and the interaction forces are known. The interaction forces can be derived either from first-principles simulations, in which case, one can speak of *ab initio* MD, or from effective potentials that are derived from experiments or *ab initio* simulations. Unfortunately, *ab initio* MD simulations are computationally expensive, and hence, their application is usually limited to situations where the number of atoms is $O(100)$; in addition, *ab initio* MD simulation time rarely exceeds a few picoseconds. Therefore, classical MD simulations (using effective potentials) are employed in this investigation with interatomic potentials that are benchmarked to several equilibrium properties.

The classical MD technique is based on the Newton's second law of motion. For an isolated system of N atoms with position $\{\mathbf{r}_i\}$ and momentum $\{\mathbf{p}_i\}$, the total energy of the system can be expressed as [47]

$$H(\mathbf{r}_1, \mathbf{r}_2, \dots, \mathbf{r}_N, \mathbf{p}_1, \mathbf{p}_2, \dots, \mathbf{p}_N) = \frac{1}{2}\sum_i \frac{\mathbf{p}_i^2}{m_i} + U(\mathbf{r}_1, \mathbf{r}_2, \dots, \mathbf{r}_N) \tag{3.1}$$

where m_i is the mass of the i^{th} atom. The first term represents the sum of the kinetic energy of N atoms and U describes the potential energy of the system. The equation of motion of the i^{th} atom is given by

$$\frac{d\mathbf{p}_i}{dt} = \mathbf{F}_i - \frac{\partial H}{\partial \mathbf{r}_i} = -\frac{\partial U}{\partial \mathbf{r}_i} \tag{3.2}$$

With a prior knowledge of the appropriate initial conditions, the Newton's equations of motion for the system of atoms can be solved by numerical integration methods. Several numerical algorithms have been developed in the past, among which Verlet and Velocity-Verlet [75] are most widely used in the community. In the Verlet algorithm, the velocity and force acting upon each atom are obtained from the difference of $\mathbf{r}_i(t+\delta t)$ and $\mathbf{r}_i(t-\delta t)$. At the beginning of a simulation, i.e., at $t = 0$, the configuration $\mathbf{r}_i(0)$ is taken as the initial coordinates of the *N*-atom system. The configuration at a later time, as given by $\mathbf{r}_i(\delta t) = \mathbf{r}_i(0) + \mathbf{v}_i(0)\delta(t) + \frac{\mathbf{F}_i(0)}{2m_i}(\delta t)^2$, can only be calculated if the initial velocity of each atom in the system is known. Therefore, to start a MD simulation, it is necessary to initialize the system velocities. In this dissertation, the initial velocities are chosen from a Maxwellian distribution corresponding to a temperature *T*. The velocity of the center-of-mass is subtracted from the initial velocities to ensure that the simulation box does not drift in space. Velocity-Verlet algorithm, which has the energy conserving or symplectic property, is used in the current work.

3.2 Interatomic Potentials for Equilibrium States

MD simulations depend on the fidelity of the interatomic potentials; for a *N*-atom system, the potential energy can be expressed as [76]

$$U(\mathbf{r}^N) = \sum_i U^{(1)}(\mathbf{r}_i) + \sum_{\substack{i,j \\ i<j}} U^{(2)}(\mathbf{r}_i, \mathbf{r}_j) + \sum_{\substack{i,j,k \\ i<j<k}} U^{(3)}(\mathbf{r}_i, \mathbf{r}_j, \mathbf{r}_k) + \cdots \tag{3.3}$$

where, the first term represents the external potential which depends on the coordinates of each atom, the second term represents the pair term, followed by the three body term and so on.

An interatomic potential is called a pair potential when it depends only on the pair separation distance $\mathbf{r}_{ij} = \mathbf{r}_i - \mathbf{r}_j$. The potential energy of a system of atoms that interact among themselves via a pair potential is given by [76]

$$U^{(2)} = \sum_{\substack{i,j \\ i<j}} u_{ij}(r_{ij}) \tag{3.4}$$

Central pair potentials have some inherent deficiencies in describing complex systems; for example, they are seen to yield wrong predictions for transition metals, including bond energies that depend on the local bonding environment, and a zero value for the Cauchy pressure (i.e. $C_{12} = C_{44}$). These discrepancies for the metallic system are related to the inability of the pair potentials to handle the many body interactions [77] and can be overcome by using an embedded atom method (EAM) potential [78] which implicitly includes the many body interactions.

In this dissertation, three materials: argon (Ar), silicon (Si) and copper (Cu) that have very different bond structures are simulated. A Lennard-Jones potential [55] is used for simulating Ar; it is described by a pairwise potential and is expressed as

$$u(r_{ij}) = \begin{cases} 4\epsilon\left[\left(\frac{\sigma}{r_{ij}}\right)^{12} - \left(\frac{\sigma}{r_{ij}}\right)^{6}\right], & r_{ij} < r_C \\ 0, & r_{ij} \geq r_C \end{cases} \tag{3.5}$$

where, ϵ governs the strength of the interaction, σ defines the length scale and r_C is the cut-off distance of the potential. Ar has been well-studied in the last several decades; the parameters for the LJ potential for Ar are ε =0.997 kJ/mol, σ = 3.405 Å and $r_C = 3.0$ Å. Stillinger-Weber (SW) potential is used to simulate Si; it is described by a three body potential introduced by Frank H. Stillinger and Thomas A. Weber [79]. The potential contains of two parts, the first part is a pair-wise potential, while the second part is constituted by a three-body potential. The pair potential is expressed as

$$u_2(r_{ij}) = \begin{cases} A\left(Br_{ij}^{-p} - r_{ij}^{-q}\right)\exp\left[\left(r_{ij} - a\right)^{-1}\right], & r_{ij} < a \\ 0, & r_{ij} \geq a \end{cases} \tag{3.6}$$

where A, B, p, and a are positive constants. $r = a$ is the cut-off radius and the same cut-off value is applied for the three body interaction u_3, which is expressed as

$$u_3(\mathbf{r}_i, \mathbf{r}_j, \mathbf{r}_k) = h(r_{ij}, r_{ik}, \theta_{jik}) + h(r_{ji}, r_{jk}, \theta_{ijk}) + h(r_{ki}, r_{kj}, \theta_{ikj}) \tag{3.7}$$

where θ_{jik} is the angle between $\mathbf{r}_j$ and $\mathbf{r}_k$ subtended at vertex i. The function h belongs to a two-parameter family, which has the following form

$$h(r_{ij}, r_{ik}, \theta_{jik}) = \lambda \exp\left[\gamma(r_{ij} - a)^{-1} + \gamma(r_{ik} - a)^{-1}\right] \times \left(cos\theta_{jik} + \frac{1}{3}\right)^2 \quad (3.8)$$

SW potential is widely used in the simulation of Si and is demonstrated to reproduce the properties in solid, liquid and supercooled states [80-84]. In addition, SW predictions are shown to be in close agreement to those obtained from *ab initio* simulations [85, 86].

In the simulations of copper, embedded atom method (EAM) interatomic potential is employed. The root of the formalism lies in the density functional theory. Conceptually, this method is based on the notion that the energetics of an atom placed in the environment of a solid depends on the electron density of the host atoms .For a single component system, the potential energy is given by

$$u = \sum_{i=1}^{N-1} \sum_{j=i+1}^{N} \varphi(r_{ij}) + \sum_{i=1}^{N} \Phi(\varrho_i) \quad (3.9)$$

where r_{ij} is the distance between atoms i and j , $\Phi(\varrho_i)$is the energy required to embed an atom in the position i of the host matrix. ρ_i is the electronic density at the position $\boldsymbol{r}_i$ due to all other atoms in the host at position $\boldsymbol{r}_j$. The first term in the above expression is a repulsive pair potential, whereas the second term describes the many-body interaction. Note that the potential is environment dependent, since a change in the coordination of an atom will result in a different electron density and therefore, will change the bond energy [87]. The embedding function, the electron density and the pair potentials can be obtained either from *ab initio* simulations or from a fitting to experimental properties such as the atomic volume, the elastic constants or the ground state structure [88]; this formalism also has enabled the development of interatomic potentials for alloys [89]. One of the drawbacks of an EAM potential is that the properties near the melting point of a material are not well predicted; this problem has been overcome recently by Sturgeon and Laird [90], who reproduced the melting point quite accurately for Al. Recently, Mendelev and co-workers tested several EAM potentials for bulk materials in both solid and liquid states and developed the ABCHM potential for Cu [91]. In the present work, the ABCHM potential have been employed for the simulations of Cu; good agreement is observed with data reported from several experimental investigations.

3.3 Interatomic Potentials for Non-Equilibrium States

The potentials outlined in the previous section yield a good description if the inter-atom distances do not deviate far from those at equilibrium conditions. However, in simulations of displacement cascades following radiation, the atoms can approach very close to each other, usually within a separation distance of 1 Å. At such instances, the equilibrium potentials fail to correctly describe the interactions. In order to overcome this difficulty, a ZBL potential [92], which is a screened Coulombic potential [93], is employed for all the materials that are investigated in this dissertation. The idea is to stitch the ZBL potential with the pairwise part of the equilibrium potential such that there is a smooth transitioning without any discontinuity in the forces. In the current work, the potential for Ar, which is pairwise, is stitched with the ZBL directly. For Cu and Si that are described by many-body potentials, the ZBL potential is added to the pairwise part of the many body potential. A Fermi function f_F, is employed as described below for a smooth interpolation; the combined pairwise potential is expressed as [94]

$$V_{ij} = \left(1 - f_F(r_{ij})\right) V_{ij}^{ZBL} + f_F(r_{ij}) V_{ij}^{Eq} \tag{3.10}$$

where, V_{ij} is the summed pairwise potential, V_{ij}^{ZBL} is ZBL potentail, and V_{ij}^{Eq} is the pairwise potential in equilibrium. The function $f_F(r_{ij})$ is expressed as [94]

$$f_F(r_{ij}) = \frac{1}{1 + e^{-A_F(r_{ij} - r_C)}} \tag{3.11}$$

In the expression for $f_F(r_{ij})$, there are two adjustable parameters: A_F and r_C. A_F controls how sharp the transition is between the two potentials, while r_C is the cutoff radius for the ZBL potential. The ZBL potential is described as

$$V_{ij}^{ZBL} = \frac{1}{4\pi\epsilon_0} \frac{Z_1 Z_2 e^2}{r_{ij}} \phi(r_{ij}/a) \tag{3.12}$$

Note that the ZBL potential has two terms – the first one is the Coulombic repulsive term, with Z_1 and Z_2 denoting the number of protons in each nuclei, while the second part is the universal screening function, where a is a function of Bohr radius a_0 that can be cast in the form of

$$a = \frac{0.8854 a_0}{Z_1^{0.23} + Z_2^{0.23}} \tag{3.13}$$

The screening function $\phi(x)$ can be written as

$$\phi(x) = 0.1818 e^{-3.2x} + 0.5099 e^{-0.9423x} + 0.2802 e^{-0.4029x} + 0.02817 e^{-0.2016x} \tag{3.14}$$

For single component systems, $Z_1 = Z_2 = Z$; then the equation (3.12) and (3.13) can be simplified as

$$V_{ij}^{ZBL} = \frac{1}{4\pi\epsilon_0} \frac{Z^2 e^2}{r_{ij}} \phi(r_{ij}/a) \tag{3.15}$$

$$a = \frac{0.4427 a_0}{Z^{0.23}} \tag{3.16}$$

The two parameters A_F and r_C are chosen such that they yield accurate thermodynamic and dynamic properties in the equilibrium states. The parameters are listed in Table 3.1.

Table 3.1 ZBL parameters (A_F, r_C)

Parameter/Material	**Argon**	**Silicon**	**Copper**
$\boldsymbol{A_F}$ (Å^{-1})	16	14	16
$\boldsymbol{r_C}$ (Å)	1	1	1

3.4 Propensity and Displacement in Isoconfigurational Ensemble

Isoconfigurational ensemble has been developed in the past to ascertain the dynamical behavior in disordered media such as glasses and supercooled liquids [95-100]. In such an ensemble, several copies of the same configuration are allowed to evolve in time, however, with different initial momenta drawn from a Maxwell-Boltzmann distribution. The dynamical variables for each atom are then averaged over the different copies. A graphical representation of this ensemble is shown in Figure 3.1:

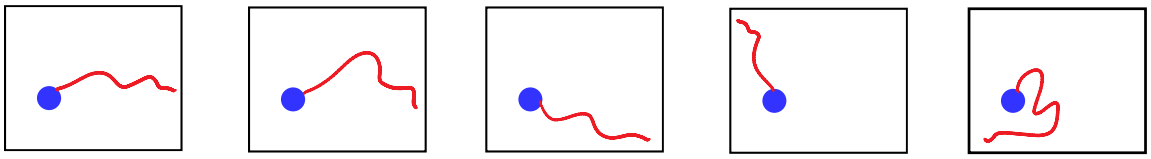

Figure 3.1 An isoconfigurational ensemble

The idea of using isoconfigurational ensemble is to follow the trajectory of each atom individually and then get the averaged trajectory over different copies with different initial momenta. This can be expressed as

$$\langle r_i(t)\rangle_{ic} = \frac{1}{M}\sum_{k=1}^{M} r_i(k,t) \tag{3.17}$$

where, M is the number of intial ensembles; $r_i(k,t)$ is the instant trajectory of atom i from ensemble k at time t.

The isoconfigurational ensemble has been used to calculate the 'propensity' in equilibrium simulations and displacement probabilities for radiation cascade simulations. The concept of propensity has been first introduced by Widmer-Cooper [95]. There are two kinds of propensity – the first one is the dynamic propensity, while the other is known as the coordination propensity. In this dissertation, we only refer to the dynamic propensity. The dynamic propensity of an atom i at a time, t, is defined as the mean squared-displacement of that particular atom:

$$\langle \Pi(t) \rangle_{ic} = \frac{1}{M} \sum_{k=1}^{M} [\mathbf{r}_i(k,0) - \mathbf{r}_i(k,t)]^2 \tag{3.18}$$

Recent work on supercooled and glass-forming liquids show that propensity is a reliable metric to identify dynamical heterogeneity (DH) from MD simulations [95-98, 101, 102]. In the current work, we have also employed dynamic propensity to demonstrate the difference between different supercooled states of liquid silicon.

Similarly, we have employed a directional displacement metric to measure the correlated dynamics in a radiation environment. The displacement metric is expressed as:

$$\langle D_{i,x}(t) \rangle_{ic} = \frac{1}{M} \sum_{k=1}^{M} [x_i(k,t) - x_i(k,0)] \tag{3.19}$$

where, $x_i(k,t)$ is the position in one of the three directions of atom i in ensemble k at time t. We have observed that the displacement distributions do not differ significantly with different starting configurations. Typically, one hundred isoconfigurational copies having different momenta are needed to generate statistically significant displacements in radiation cascade simulations. To visualize the displacements of each atom in an iso-configurational, a displacement map is constructed by assigning a sphere of radius (R_s) to the initial position of the atoms where R_s is given by [103]

$$R_s = R_{min} \exp\{|(R_i - N/2)/(1 - N/2)| log(R_{max}/R_{min})\} \tag{3.20}$$

$R_{\min}$ and $R_{\max}$ take the values 0.01 Å and 0.5 Å, respectively, R_i is a sorted integer rank of the displacement values, and N is the total number of atoms in the simulation. The spatial correlations of the displacements at different times can be visualized in real space and they give rich clues to the dynamical behavior of the atoms [100]. We use this visualization metric to demonstrate dynamical recovery process in Cu, Si and Ar, which are discussed in more detail in the following chapters.

3.5 Non-Equilibrium MD Radiation Cascade Simulations and Boundary Control

In order to simulate radiation cascades, we have chosen a cubic simulation box containing about 500,000 atoms for Cu and Si; a smaller system of 70,000 atoms was chosen for Ar. All of these calculations were done using periodic boundary conditions (PBC). We have also performed cascade simulation on a bigger system of four million atoms to test whether the dynamics depends on the size of the simulation cell. Since the simulations with a larger system of 4 million atoms showed no significant difference in the relaxation/correlation dynamics, following radiation impact, we have used the aforesaid number of atoms (approximately, half a million for Cu/Si, and 70,000 for Ar) for all the simulations. In all these simulations, primary knock-on atom (PKA) is introduced near the center of the simulation box along the <100> crystallographic direction as shown in Figure 3.2 (left). The knock-on energy of the PKA is chosen such that it is approximately 100 times more than the average displacement energy. For Si and Cu, the initial knock-on energy is 3 keV whereas for Ar, it is chosen as 100 eV. The dynamical effects of different PKA energies are also investigated by varying the PKA energy from 1 keV to 50 keV. An 'inner box' as shown in Figure 3.2 (right), typically encompassing 20,000 atoms, is employed to probe the local dynamical/structural relaxation in the disordered zone. The 'inner box' is further divided into a 'fore' region that is ahead of the knock and a 'wake' region, which is behind the knock.

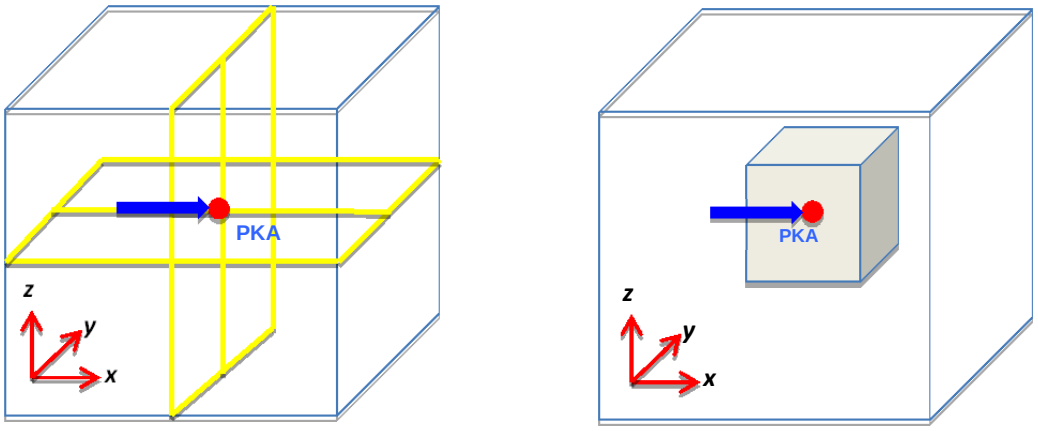

Figure 3.2 (Left) MD simulation box depicting the primary knock-on atom (PKA). An impulse along the (1 0 0) direction, which is parallel to the *x*-axis, is given to the PKA. (Right) An 'inner box', which is further divided into 'fore' and 'wake' regions, is employed to evaluate the local dynamical and structural changes near the PKA.

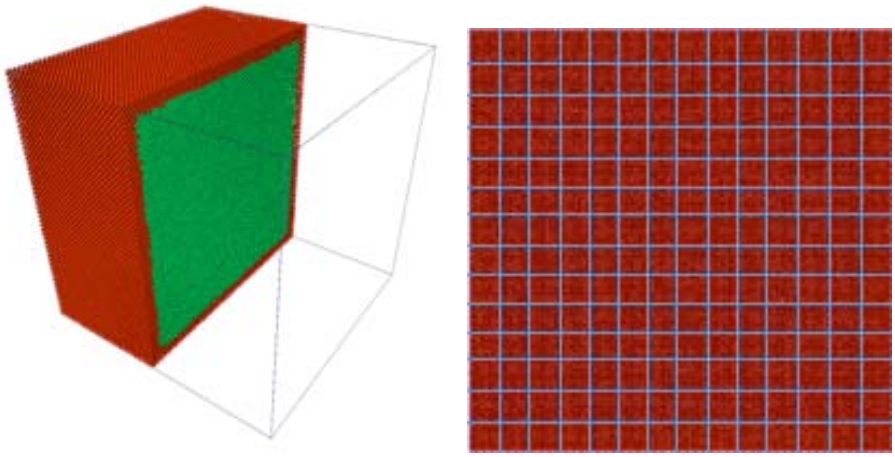

Figure 3.3 Method of temperature control at the boundary layers

At the beginning of each simulation, the initial atomic configuration is equilibrated for 20 picoseconds (ps), approximately, at the specified temperature (300 K for Cu and Si, and 18 K for solid Ar) such that when the PKA is introduced, the equilibrium phonon modes are well-established. Since atomic vibrations occurs with a timescale of ~ 1 ps, 20 ps is regarded to be long enough for equilibration. The equilibration is performed in a NVE ensemble where the number of atoms (N), volume of the simulation box (V) and the energy of the system (E) are kept constant. In the simulation of displacement cascade, excess energy is brought into the simulation cell by the PKA; the excess energy of the PKA leads to the production of displacement cascade. To drain out this energy, it is necessary to couple a heat bath at the outer layers of the simulation box. To model this heat bath, the temperatures of all the atoms at the outermost six layers of the boundaries are controlled with a damped Nose-Hoover thermostat [104-106]. These six layers, with a layer depth of around 3 to 5 times the lattice constant, at the boundary are designated as the 'exterior' region shown in red in Figure 3.3 (left), whereas the other atoms contained within the rest part of the simulation box are designated as the 'interior' region without any temperature control. To reduce the excess energy and momentum more efficiently, we have divided each boundary layer into several sub-boxes as shown in Figure 3.3 (right), and applied temperature control for each sub-box in the six layers. This ensures constant temperature at all local areas. Since the local pressure in the boundary layers is correlated to temperature, this method also helps to keep the local pressure at each sub-region close to zero and avoid spurious reflection of pressure waves into the simulation box. We have observed from the case studies that our method of thermostatting at boundaries efficiently absorb the excess energy and

momentum from the system without affecting the dynamical structure of the cascade core. For equilibration the system, a time step of 10^{-3} ps is found to be satisfactory for integrating the Newton's equation of motion. Upon radiation impact, owing to the fact that in the collision phase, the PKA and recoiled atom are subjected to high velocities, a time step of 10^{-4} ps is used for the first picosecond followed by a time step of 10^{-3} ps for the remainder of the simulations.

3.6 Field Construction

Field data are constructed based on average molecular motion; they are low-order moments of the *N* atom distribution. Two thin slivers with a thickness of 6 atomic layers are chosen – the first one is a thin section in the *yz* plane, normal to the knock and the other in the *yx* plane, parallel to the knock. The chosen layers, which include the PKA, are then further divided into sub-regions as shown in Fig. 3.4, and the microscopic variables are averaged within each sub-region. The averaged variables are construed to be the two-dimensional representation of the continuum field data [65].

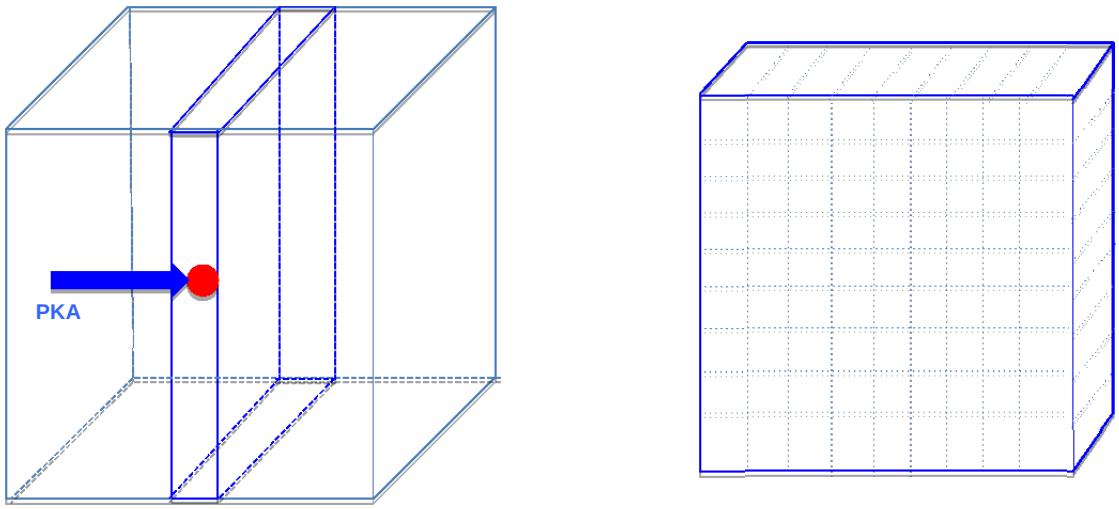

Figure 3.4 Field construction on a plane normal to radiation impact

Chapter 4. Liquid-Liquid Phase Transition in Silicon

4.1 Introduction

As elucidated in the next chapter, silicon portrays a supercooled-like behavior following radiation. In this chapter, we investigate the supercooled state of silicon using equilibrium simulations. Experiments on hyperfast melting induced by laser excitation [35] and ion irradiation [107] have lent plausible evidence for liquid polymorphism [108, 109] or liquid–liquid (L–L) phase transition in silicon (Si). Hypothesized long before by Rapoport with a two species model [110] and demonstrated experimentally in recent years in phosphorous [111], yttria–alumina melt [112], and water [113-115], polymorphism in pure liquids is a subject of several recent investigations and is increasingly regarded to have technological implications such as in the biomolecular systems [116-118]. Observing the L–L phase change experimentally in Si under quasi–equilibrium conditions is particularly challenging as the transition occurs in the deeply supercooled states. Several experiments using levitation techniques however, lead to differing interpretation on the evolution of liquid structure as Si is cooled from above the melting point [119-123]. Coexistence of metallic and covalent bonds, often considered as a marker for L–L phase transition in Si, observed recently by Okada et al. [124] using x–ray Compton scattering at relatively high temperatures (1787K) suggests the possibility of a L–L transition at lower temperatures.

The first persuasive evidence for polymorphism in Si presented by Sastry and Angell [124] shows a first order phase transition from a fragile, high density liquid (HDL) to a strong, low density liquid (LDL) at 1060K and zero pressure using classical molecular dynamics (MD) simulations with Stillinger–Weber (SW) potential. A more recent investigation with SW potential places the liquid–liquid critical point at $T_c \approx 1120$K and $p_c \approx -0.6$Gpa [125]. *Ab–initio* simulations, generally agree on the transition temperature with Jakse and Pasturel [126] reporting the L–L transition to occur at 1150K, and Ganesh and Widom [127] reporting a critical temperature and pressure of 1232K and –1.2GPa, respectively.

As a central measure that characterizes the supercooled states [128] and one which is often used as a marker for glass transition, viscosity is generally not computed directly with simulations [129, 130]; often it is inferred from the structural relaxation time evaluated through density correlators with the

tacit assumption that viscous and density relaxation times are equivalent. While experimental methods face formidable challenges for the supercooled states of some materials such as Si, viscosity remains arguably one of the most important supercooled properties with Angell's strong/fragile and fragile–to–strong classification emanating from the viscosity dependence on temperature [131, 132].

In the current study, we investigate the relaxation of stress and space–time correlators of liquid Si with MD simulations using Stillinger–Weber potential [84]. Our principal objective is to identify the dynamic transitions or crossovers, akin to experimental analysis, and derive a mechanistic understanding of the evolution of supercooled states of Si by probing the relaxation behavior of three autocorrelators, stress, density and energy – the three fundamental quantities that have associated conservation laws. Using the Green-Kubo formalism, we determine the viscosity from the time integral of stress autocorrelators for different temperatures and identify *two* dynamic transitions or crossovers. The low temperature transition is particularly interesting as it corresponds to either a HDL–LDL phase transition [84], or a HDL–HDL crossover without a significant change in the liquid structure, depending on the cooling rate. We also show that there is a structural motif for the low temperature transition (both HDL and LDL) while there is none for the higher transition at the higher temperature. The two transitions are further confirmed through observations on *decoupling* of stress, density and energy relaxation, and a pronounced dynamical heterogeneity [43] evaluated through an isoconfigurational analysis on propensity [95, 97, 99]. Finally we delineate an intriguing collapse of dynamical heterogeneity and a return to partial homogeneity across the HDL–LDL transition that indicates a dynamic mechanism of relieving the frustration in supercooled states while attaining a more thermodynamically favorable state.

4.2 Time Correlators and Molecular Dynamics Simulations

The viscosity (η) variation with temperature is first employed to locate the dynamic transitions or crossovers. The viscosity is computed by evaluating the time integral of the shear stress autocorrelator which is given by

$$\eta = \frac{V}{3k_BT}\int_0^\infty dt \left\langle \sum_{x<y} \tau_{xy}(t)\tau_{xy}(0) \right\rangle \tag{4.1}$$

where τ is the shear stress, V is the system volume, T is the temperature and k_B is the Boltzmann constant with x and y denoting two orthogonal directions. The components of the shear stress tensor (τ) components are evaluated as

$$\tau_{xy} = \frac{1}{V}\left[\sum_j m_j v_j^x v_j^y + \frac{1}{2}\sum_{i\neq j} r_{ij}^x r_{ij}^y\right] \tag{4.2}$$

where v, r, and F stand for velocity, position and force, respectively, the indices i and j denote two atoms in the system, and V is the system volume. The dynamic crossovers are further confirmed by investigating decoupling observed in the density, stress and energy autocorrelators. The density and energy autocorrelators, $F(\mathbf{k},t)$ and $E(\mathbf{k},t)$, as discussed before, are given by [47]:

$$F(\mathbf{k},t) = \frac{1}{N}\langle\sum_{i=1}^{N}\sum_{j=1}^{N} e^{i\mathbf{k}\cdot[\mathbf{r}_i(t)-\mathbf{r}_j(0)]}\rangle \tag{4.3}$$

$$E(\mathbf{k},t) = \frac{1}{N}\langle\sum_{i=1}^{N}\sum_{j=1}^{N} E_i E_j e^{i\mathbf{k}\cdot[\mathbf{r}_i(t)-\mathbf{r}_j(0)]}\rangle \tag{4.4}$$

where $\mathbf{k}$ and $\mathbf{r}$ are the wavevector and position vector, respectively, and E_i is the sum of kinetic and potential energy of an atom i, and N is the total number of atoms. Among these, density relaxation has been investigated the most primarily because a wave-vector dependent density correlator is regarded an apposite slow variable in the mode coupling theory (MCT) [133]. Other correlators such as temperature field [134], stress as shown in Eqn (4.1) and energy as shown in Eqn. (4.4), are also appropriate slow variables, and in general, the differences in their relaxation behavior have not been investigated in the past for supercooled liquids. We will focus on the relaxation behavior of stress, density and energy autocorrelators, and show that they exhibit subtle but discernible changes across the dynamic crossovers.

The autocorrelators are evaluated using MD simulations which are performed with 1728 atoms using periodic boundary conditions. Stillinger–Weber potential is used to describe the interactions between the atoms and the three–body interactions are split pair–wise for computing the shear stress tensor components as shown in Eqn. (4.2). Velocity-Verlet scheme is used to integrate the equations of motion with a typical time step of 0.3 fs. The viscosity evaluations are averaged over 20,000

independent (overlapped) sets of correlation data for each temperature; such a large number of independent averages are employed to reduce the statistical noise and to capture the subtle changes in the variation of viscosity with temperature which signify the dynamic transitions. Two cooling rates (16.7 K/ps and 8.8 K/ns) are employed to generate two structures in Si – HDL and LDL. As observed by Sastry and Angell [84], we detect a HDL–LDL phase transition near 1006 K with the lower cooling rate of 8.8 K/ns along the characteristic drop in enthalpy signifying a thermodynamic phase change. With a higher cooling rate, on the other hand, the system continues to be in HDL state with the system however, undergoing a HDL–HDL crossover at 1006 K. The next sections will contrast the dynamic behavior of the two structures at different temperatures.

4.3 Dynamic Transitions from Viscosity

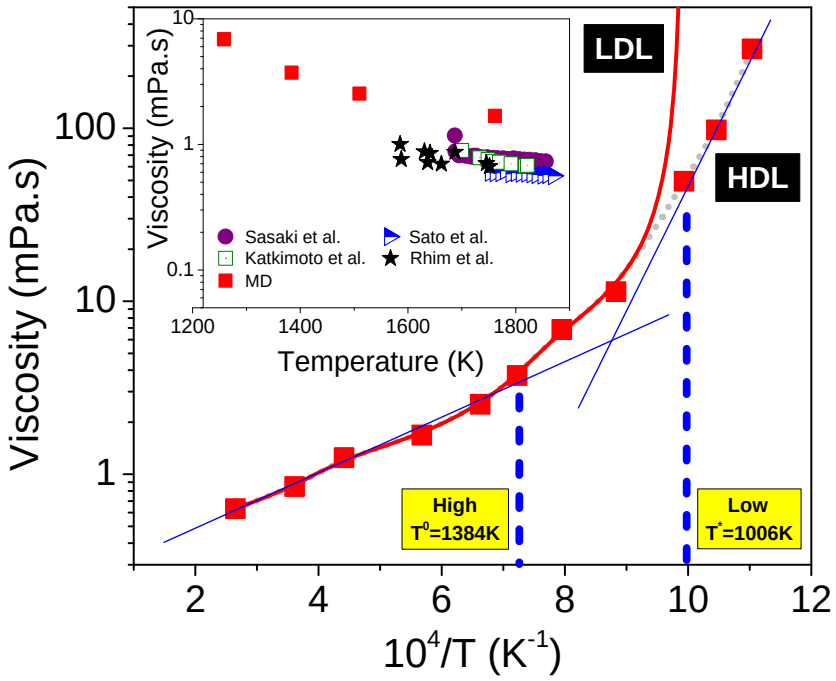

Figure 4.1 Viscosity of supercooled Si and two transition temperatures marked as 'High' (≈1384 K) and 'Low' (≈1006 K). The HDL–HDL dynamic crossover is validated with observations on cage dynamics (Figure 4.2), attendant decoupling in density/stress/energy relaxations (Figures 4.3 and 4.4), and the evolution of dynamic heterogeneity (Figures 4.5 and 4.6). (Inset) A comparison of MD simulation results with experimental data [134-137] showing a modest over–prediction with SW potential.

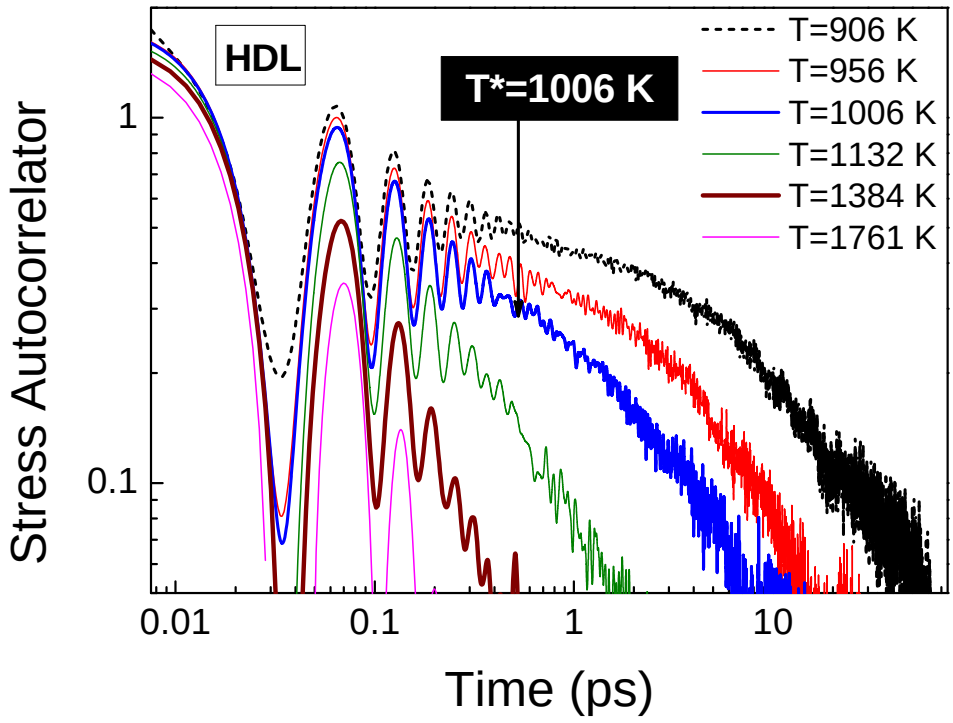

Figure 4.2 Stress autocorrelators (arbitrary units) for HDL at different temperatures.

Figure 4.1 shows the viscosity variation for temperatures ranging from 3774 K to 906 K. The inset shows a comparison of the viscosities computed by MD and experimental data in the liquid and supercooled regime [135-138]. While the MD simulations over-predicts the viscosity, considering the many-body nature of the bonding in Si and the difficulties in conducting controlled experiments at higher temperature for supercooled silicon, the agreement and observed trend is reasonable. From the change in the slope of the viscosity variation we can identify two dynamic transitions, one at 1384 K and the other at 1006 K, which are identified as 'High' and 'Low' in Figure 4.1. The high temperature transition (1384 K) corresponds to the departure from homogeneous dynamics which is further quantified in Figures 4.3 and 4.4. At the low temperature transition (1006 K), the smaller cooling rate (8.8 K/ns) results in a HDL–LDL phase transition with an extremely large increase in the viscosity. With a much faster cooling rate of 16.7 K/ps, we uncover a HDL–HDL crossover at 1006 K without any notable change in the liquid structure and with a modest increase in the viscosity. Thus we discover the existence of a second transition temperature at which supercooled Si, depending on the cooling rate, either undergoes a HDL–LDL phase transition, or experience a HDL–HDL crossover.

Since HDL–LDL phase transition is well–characterized in prior investigations [84, 126], the next sections therefore, will focus on the dynamic nature of the HDL–HDL crossover with the higher cooling rate.

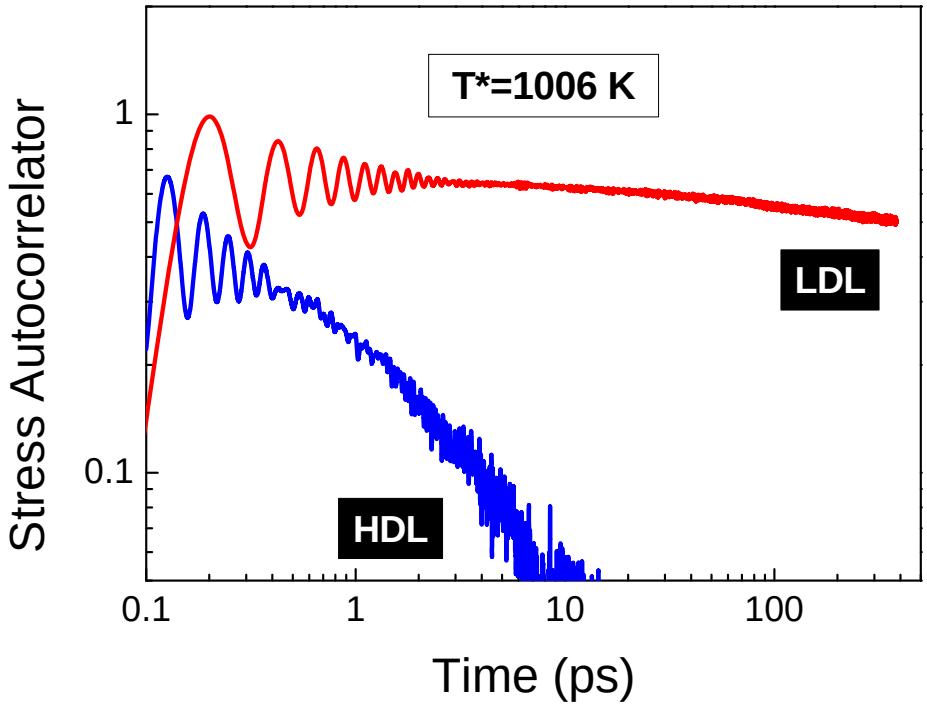

Figure 4.3 Comparison of stress autocorrelators (arbitrary units) for HDL and LDL at 1006K.

4.4 Structural Motifs for the Dynamic Transitions

It is compelling to inquire whether the observed transitions have a structural motif. There are conflicting reports on the structural changes as silicon is supercooled from high temperatures [119-123]. In this investigation we use the ratio (R^{WA}) of the first non–zero minimum in the radial distribution function (g_{min}) to the first peak value (g_{max}), a measure of local packing, to probe any accompanying structural changes with supercooling. Wendt and Abraham [139] originally proposed this ratio to detect liquid–glassy/amorphous transition by monitoring the change of slope in R^{WA} for different thermodynamic states. For Lennard–Jones systems, the liquid–glassy/amorphous transition occurs when R^{WA} becomes 0.14, approximately. Subsequent investigations show a more universal

applicability of this assessment even though the magnitude of R^{WA} is observed to be strongly system dependent [140-145].

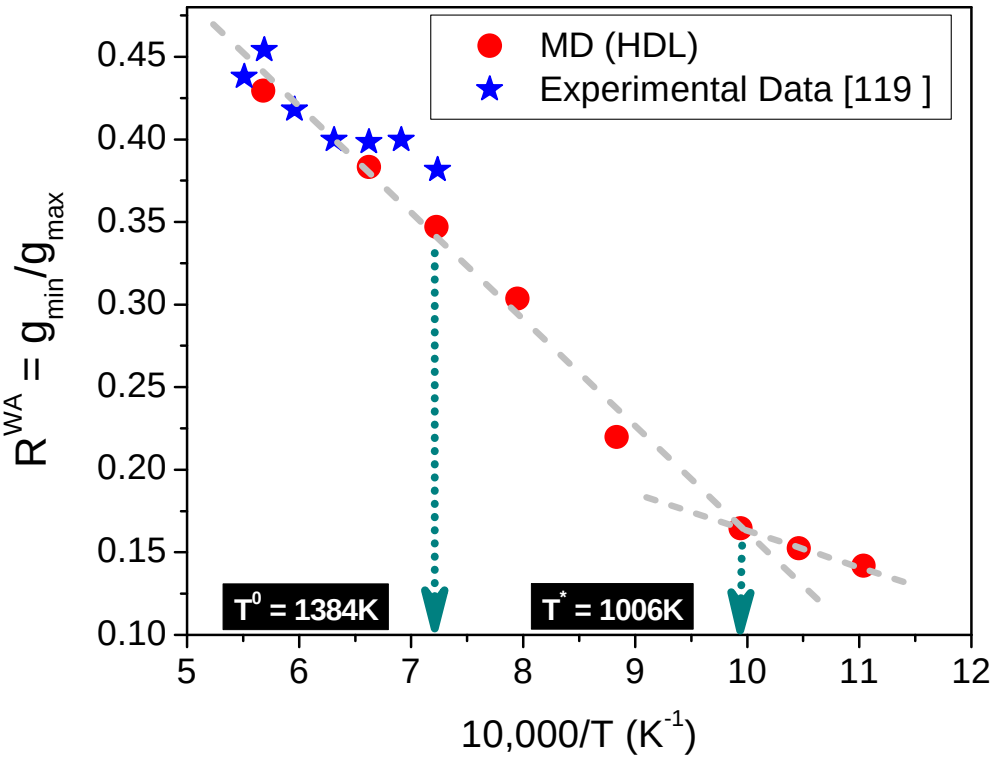

Figure 4.4 Wendt and Abraham ratio (R^{WA}) for HDL at different temperatures. For LDL, R^{WA} drops to 0.027 at 1006K (not shown).

Wendt and Abraham ratio (R^{WA}) shows a near–linear decrease with decreasing temperature for HDL (see Figure 4.4) with a pronounced change in slope at a temperature of 1006 K where the HDL–HDL crossover occurs. The slope change interestingly occurs at $R^{WA} \approx 0.15$ which is very close to the ratio originally proposed by Wendt and Abraham. At the same temperature (1006 K) R^{WA} drops by more than a factor of five to 0.0277 for the LDL state which signifies a definitive structural change associated with the coordination number switching to ~4 [84]. Thus the transitions at 1006 K are attested by identifiable structural metrics, a subtle change for HDL and a more vivid change for LDL. Equally intriguing is the lack of discernible structural change at 1384K even though there are clear dynamic changes at this temperature (to be illustrated further in the next section). Thus the high

temperature crossover is strictly dynamic in origin without any apparent structural changes. Also shown in the plot are experimental data from Kim et al. deconvoluted from structure function obtained from x–ray diffraction on levitated samples [119]. The fidelity of SW potential is again affirmed (though it has been frequently reported otherwise) by the close agreement with the experimental data.

4.5 Decoupling of Stress, Density and Energy Correlators

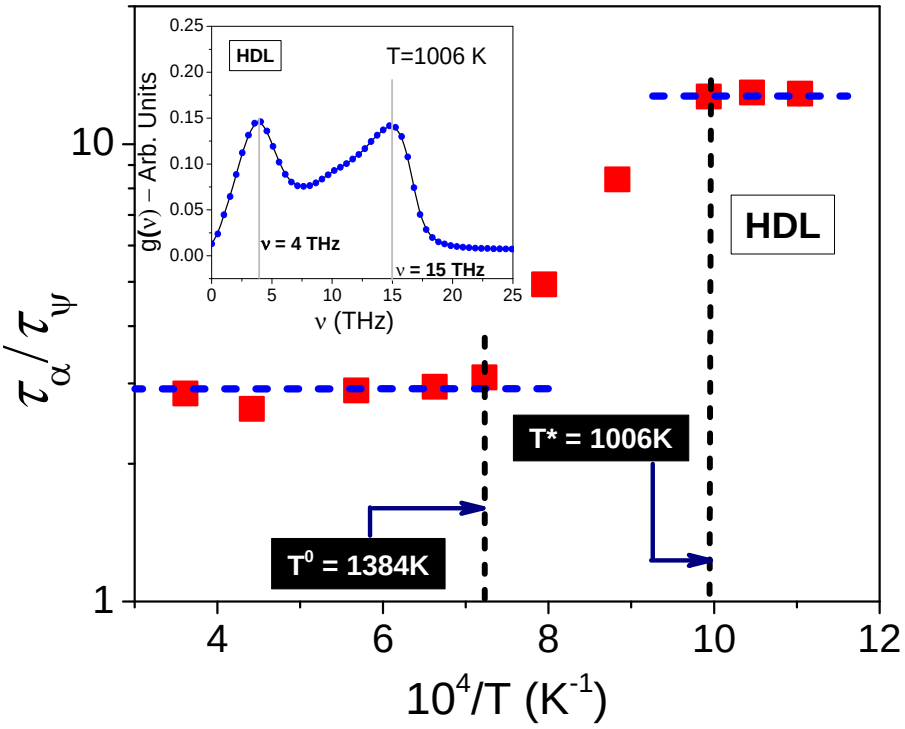

Figure 4.5 The ratio of structural relaxation time with a wavevector of 0.34 Å^{-1} to the viscous relaxation time (τ_α/τ_ψ) for HDL. (Inset) VDOS for HDL at 1006K showing two prominent frequencies, 4 THz and 15 THz.

We will now illuminate the differences between the relaxation behavior of three fundamental correlators – stress, density and energy [47]. While the density correlator is related to diffusion of atoms in the limit of zero frequency and wavevector, the energy correlator, correspondingly, is related to the thermal energy transfer that includes contribution from diffusion and quasi–vibratory modes.

The structural relaxation time (τ_α), defined as the time needed for the density correlator to decay to $1/e$ of its original value, and the viscous relaxation time (τ_ψ), defined analogously, is compared for HDL in Figure 4.5. The dynamics at chosen wavevector of 0.34 $Å^{-1}$ is representative of that of the long wavelength, hydrodynamic limit. At high temperatures (greater than 1384 K), the ratio τ_α/τ_ψ is close to 3 which suggests that the relaxation behavior has the same underlying mechanism for both density and stress. At low temperatures (less than 1006 K), τ_α is more than one order higher than τ_ψ indicating a decoupling of relaxation mechanisms, also manifested as a breakdown in the Stokes–Einstein relationship. Noticeably the crossover temperatures (1384 K and 1006 K) in Figure 4.3 correlate strongly with the two viscous transition temperatures depicted in Figure 4.1. And furthermore the transition temperatures depicted in Figure 4.5 remain unchanged when the viscous relaxation time is determined based on a lower decay value (1/5 instead of $1/e$). For the low temperature transition, the emerging quasi–vibratory modes can relax the stresses faster than through atomic diffusion or configurational change which is the dominant mechanism at the high temperature liquid and vapor states. An additional vibrational mode can be observed through the emergence of a low frequency peak (4 THz) in the vibrational density of states (VDOS) which is computed from the Fourier transform of the velocity autocorrelation function. We mention here that the two dominant frequencies 4 and 15 THz observed in the current work compare favorably with a recent *ab initio* simulation [146] which reports 3 THz and 13 THz, respectively, for HDL at 1050 K.

Next we contrast the energy relaxation with density relaxation at different temperatures. We have observed that energy and density relax almost identically at higher temperatures (and at higher wavevectors). However as temperature is decreased an intriguing decoupling takes places at short wavevectors as shown in Figure 4.6 which shows the relaxation behavior at 956 K for two wavevectors, 2.78 $Å^{-1}$ and 0.34 Å-1, with the former corresponding to the position of the first peak of the structure function at 1540 K, and the latter approaching the hydrodynamic limit. For the longer wavevector, both energy and density autocorrelators relax almost identically resulting in relaxation times that are virtually indistinguishable. A similar behavior is observed at all temperatures indicating the dominant role of local dynamics at short wavelengths. For the shorter wavevector, on the other hand, there is a noticeable decoupling between the correlators. Energy at long wavelengths is transferred by diffusion as well as through vibrations; the former is the dominant mode in dilute systems while the latter is predominant in the solid states. For supercooled states, energy transfer is mostly through diffusion and hence at higher temperatures the energy and density relaxation are almost identical (results not shown). However, as the temperature decreases quasi–vibratory modes

emerge (see inset in Figure 4.5) which provide additional pathways for transferring energy. Thus energy autocorrelator relaxes faster relative to density relaxation in the hydrodynamic limit resulting in shorter relaxation times.

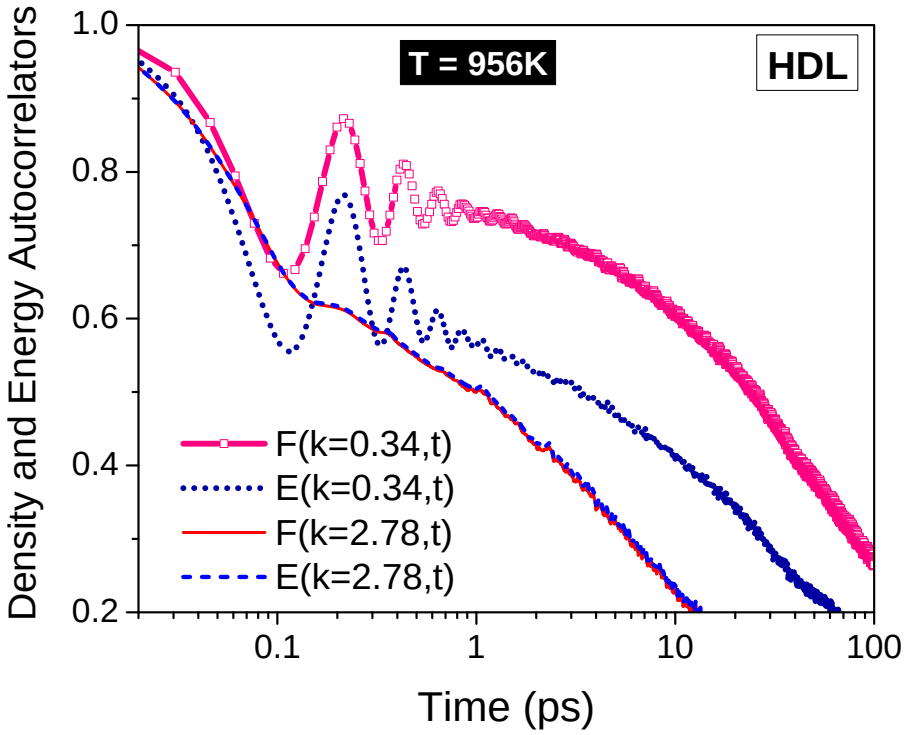

Figure 4.6 Density and energy correlators at 956K for different wavevectors. A wavevector of value 2.78 $Å^{-1}$ is near the first peak in the structure function at 1540K.

The energy relaxation times (evaluated from the energy correlator) are next contrasted with the structural relaxation times for HDL in Figure 4.7. For larger wavenumbers the relaxation behavior is almost identical for energy and density, at all temperatures. However, for smaller wavenumbers, a change is first observed at around 1384 K, the temperature corresponding to the first dynamic crossover. As can be also noticed, the difference between the relaxation times becomes amplified with a marked change in slope at the second transition temperature of 1006 K. Thus further evidence for the transitions identified in Figure 4.1 are provided through the decoupling observed in the stress, density and energy correlators.

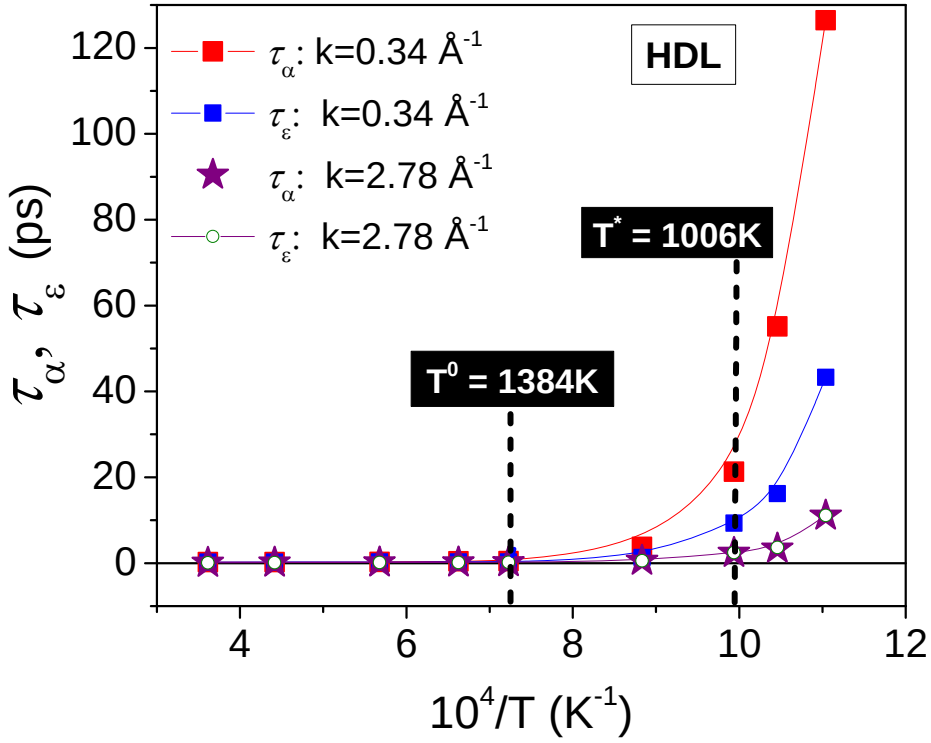

Figure 4.7 Variation of energy (E) relaxation time (τ_ε) and density (F) relaxation time (τ_α) with temperature for HDL.

4.6 Collapse of Dynamical Heterogeneity

There is growing evidence that the structural arrest in supercooled liquids emanates from the emergence of spatially correlated regions of mobile and immobile atoms defined as dynamical heterogeneity [43]. We use the concept of dynamic propensity which is defined as the mean square displacement of an atom averaged over an isoconfigurational ensemble [95, 98, 100] to distinguish the spatially distributed mobile and immobile domains. In Figure 4.8 we show the spatial propensity maps evaluated for HDL, LDL and crystal state for different simulation times and at different temperatures. The propensity map is constructing by assigning a sphere of radius [103]

$$R_s = R_{min} exp\{|(R_i - N/2)/(1 - N/2)| log(R_{max}/R_{min})\} \quad (4.5)$$

to the initial position of the atoms with R_{min} and R_{max} taking the values 0.02 Å and 1.68 Å, respectively. R_i is a sorted integer rank of the propensity values, and N is the total number of atoms in the simulation [103].

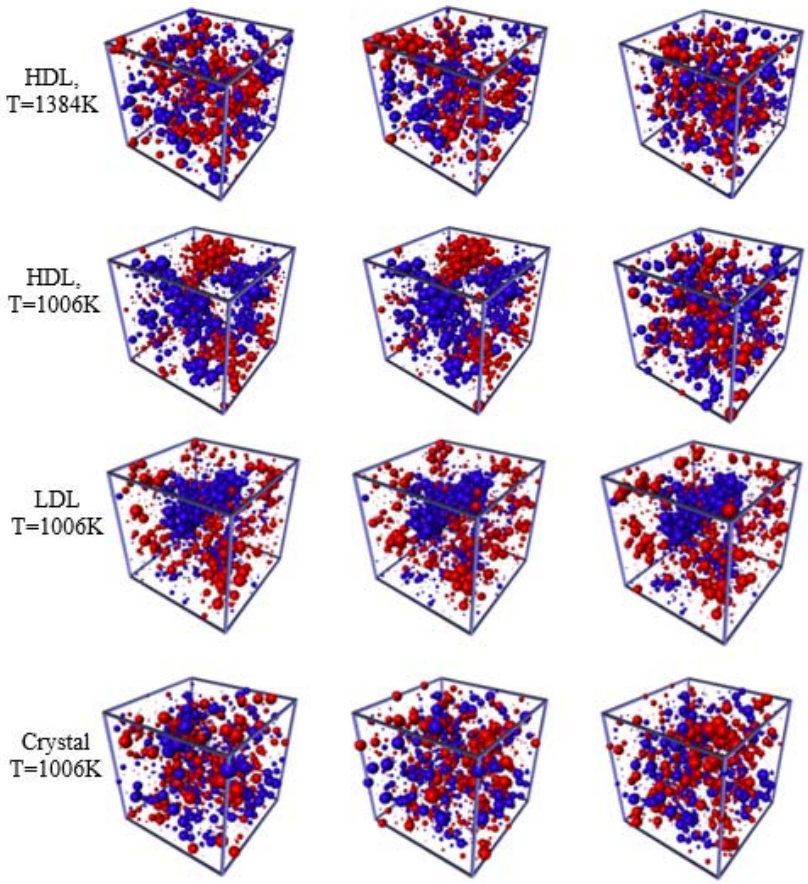

Figure 4.8 The evolution of spatial propensity [95, 98, 119] for the most mobile atoms (top 50%, blue) and the least mobile atoms (bottom 50%, red) for (i): HDL at 1384 K evaluated at different times τ = [0.2, 0.5, 4.5] ps (first panel from top), (ii): HDL at 1006 K evaluated at different times τ = [20, 60, 460] ps (second panel from top), (iii): LDL at 1006 K evaluated at different times τ = [20, 60, 460] ps (third panel from top), and (iv): crystal at 1006 K (fourth panel from top) evaluated at different times τ = [20, 60, 460] ps.

Incipient but dynamically unstable heterogeneity which collapses in picoseconds, observed near the first transition temperature (1384 K), becomes prominent and longer–lived with well–separated mobile and immobile regions for HDL at the second transition temperature (1006 K). The heterogeneous domains for HDL are stable for several tens of picoseconds and they mix over a

timescale which is *O*(100) ps. In striking contrast, the dynamical structure of LDL at 1006 K has a mixed character showing a few longer–lived monolithic groups of clusters of mobile atoms surrounded by a near–uniform spread of immobile atoms and small clusters that have a noticeable similarity with that of the crystalline state at the same temperature.

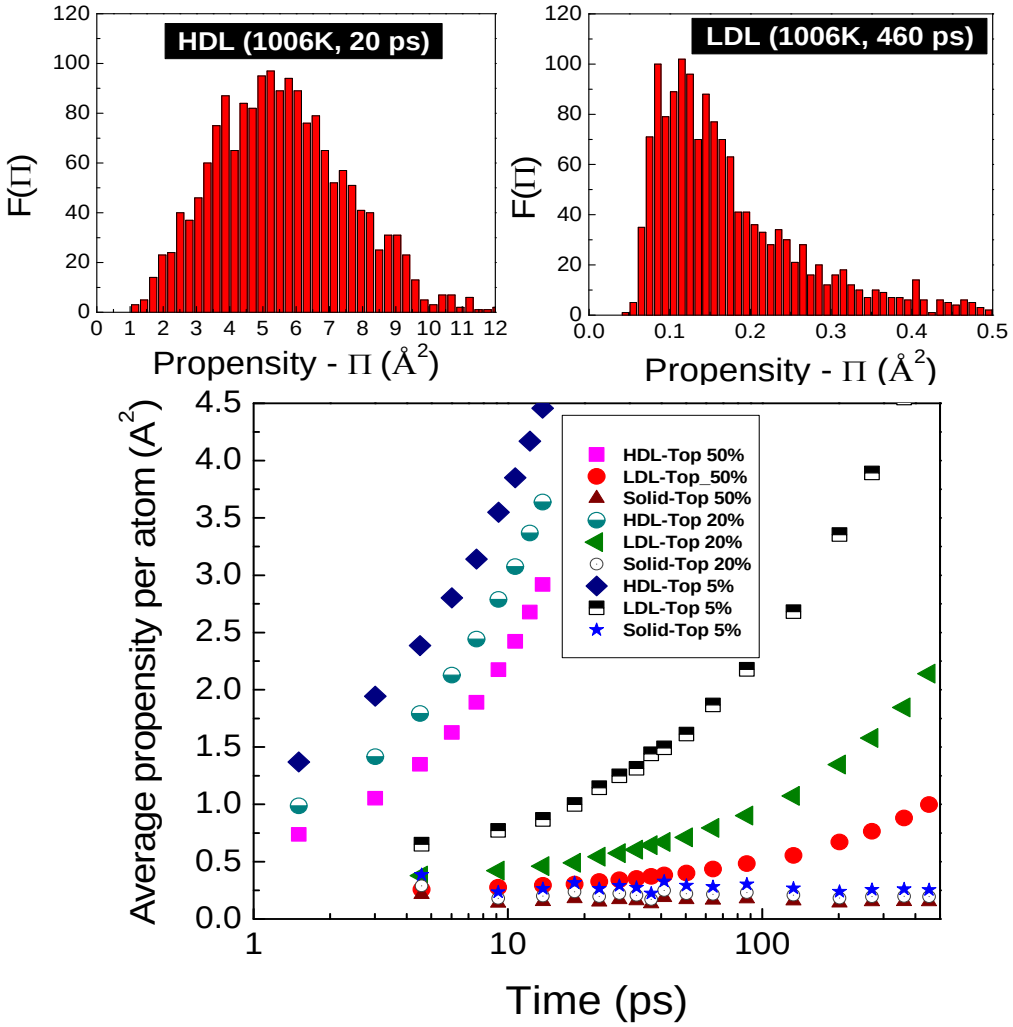

Figure 4.9 (top panel): Propensity distributions for HDL (left) and LDL (right) at 1006 K. (bottom panel): Temporal variation of propensity for HDL, LDL and solid (crystal) at 1006 K.

The propensity distributions portrayed in Figure 4.9 (top panel) contrasts the dynamical change, with the HDL showing a near symmetric distribution and the LDL portraying a skewed distribution with a longer tail which corresponds to the most mobile atoms that are clustered together. The smaller

clusters of the immobile atoms in LDL shows a distinct spatial uniformity in propensity which corresponds to the sharp rise in the distribution at $0.1Å^2$, approximately. The temporal variation of propensity (Figure 4.9, bottom panel) indicates that a relatively fewer set of atoms, which correlates to the tail of the distribution (Figure 4.9, top panel, LDL), are involved in the relaxation behavior in LDL, unlike in HDL. The dynamical uniformity in the most immobile atoms can be further gleaned from their temporal behavior which shows a dynamic formation and annihilation of immobile clusters in different spatial regions (second panel from top), a behavior also observed in the crystalline state for both immobile and mobile regions. Thus with the HDL–LDL phase transition, the large immobile clusters lose their definition and become dynamically dispersed throughout the domain.

4.7 Concluding Remarks

We provide evidence for the existence of two dynamic transitions or crossovers in supercooled Si with the high temperature transition ($T^0 \approx 1384$ K) signifying the onset of dynamic heterogeneity. At the low temperature transition ($T^* \approx 1006$ K), HDL has two pathways primarily dictated by the cooling rate – if the rate is sufficiently low, HDL can transition to LDL, a thermodynamically favorable state, or undergo a HDL–HDL crossover without a marked structural change if the rate is high enough. Given that the evolution of dynamic heterogeneity precedes the HDL–LDL transition, the partial collapse of dynamic heterogeneity in LDL can be construed as a mechanism that relieves the frustrated dynamics that exist before the transition. A similar behavior is also observed during a phase transition in supercooled liquid copper using MD simulations [147]. The crossover from heterogeneous to partly uniform or homogeneous dynamics is therefore a characteristic that can be unique to liquid–liquid phase transitions in the supercooled states.

Chapter 5. Radiation Damage and Recovery

5.1 Introduction

In this Chapter, we make quantitative predictions on correlated dynamical motion of the atoms as the liquid-like state is formed and then condensed following an ion or neutron impact. Of utmost importance are the dynamical correlations during the recovery period, which determine the final defected state. We have conducted non-equilibrium radiation cascade MD simulations on three materials that have very different bond structures – Copper, which is metallic and accurately described by an EAM potential [148] in both solid and liquid states; Silicon, which is covalently bonded and modeled through the Stillinger-Weber potential that shows excellent fidelity in reproducing the properties of solid, liquid and supercooled states [63]; and solid Argon, in which atoms interact through a weak Lennard-Jones dispersion force. At short distances, the atoms in all the three materials experience the screened Coulombic ZBL potential [93]. Through non-equilibrium shock physics formalism [64, 67], we assess the spatio-temporal evolution of the thermodynamic and defect/hydrodynamic fields in the early stages of relaxation following radiation impact as well as the deviation from equipartition, which is typically appraised in shock simulations but not in radiation cascades. Of particular significance is the use of an isoconfigurational ensemble [98] to track the mean displacements of targeted atoms such as the PKA. Isoconfigurational data are averaged over 100 independent runs with different momenta, while field and correlation functions are averaged over 5000 independent sets.

Following radiation impact, we show that materials respond by portraying an extended exponential tail in the van Hove self-correlation that signifies a dynamically heterogeneous recovery process. While a dendritic condensation of the mobile atoms in Cu and Ar are observed, long-lived spatial oscillations appear in Si. Surprisingly, the density correlator relaxes slower in the direction of momentum impulse than in the transverse directions; it decays quickly for Cu and Ar, but persists for a longer time in Si indicating a supercooled liquid-like behavior that is a precursor for amorphization.

5.2 Mean Displacement of the PKA and its Neighbors

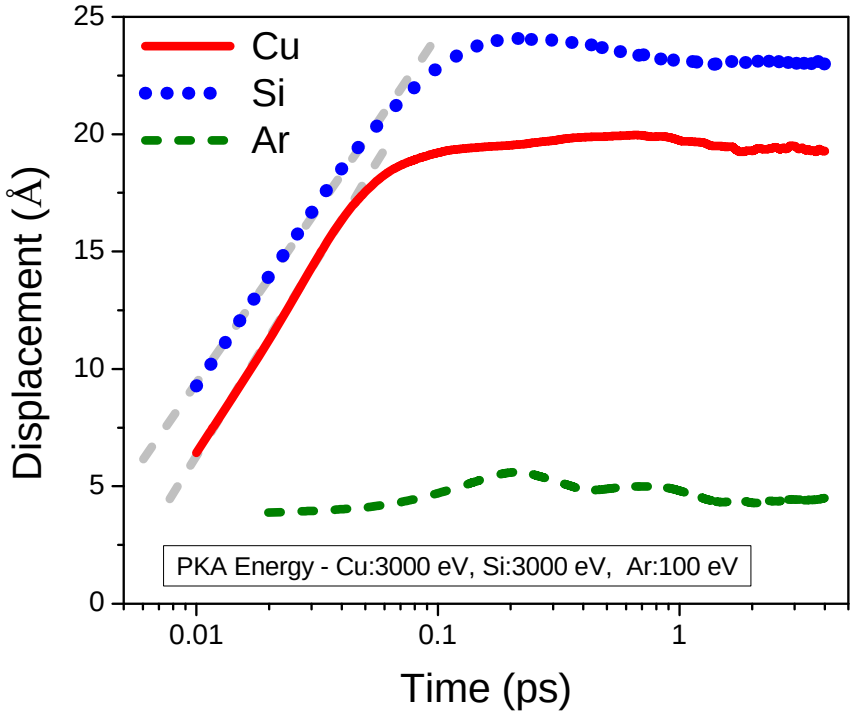

Figure 5.1 Temporal scaling behavior of the PKA. E_{PKA} = 3 keV for Cu and Si, and 100 eV for Ar; the ratio of PKA energy to the mean displacement energy is $O(100)$.

We will first briefly discuss a remarkable temporal and energy scaling behavior of the PKA using the isoconfigurational ensemble. The mean displacements of the PKA in Cu and Si evaluated through the isoconfigurational ensemble – depicted in Figure 5.1 – vary *logarithmically* with time during the hyperfast (or ballistic) timescales and then saturate somewhat abruptly, while in solid Ar, the change is initially linear followed by an undulatory trajectory after 0.2 ps. A logarithmic response is unusual in general dynamical systems as it arises from hierarchical or correlated serial constraints rather than independent parallel constraints [149]; it is observed in densification of powders [150], granular media [151], kinetics of amorphous phase transitions [152], and in slow aging of structural glasses, complex liquids and proteins [153]. Following the mechanical analogy, the PKA after receiving the knock energy distributes the excess kinetic energy preferentially to its nearest neighbors, who in turn redistributes to their neighbors in a sequential manner. Thus a hierarchical cage is built ahead of the

PKA as it traverses through the material with the faster atoms in the immediate vicinity of the PKA controlling the response of the slower atoms. Such a mechanical constraint is made possible in Cu and Si through the strong EAM and covalent bonds that have characteristic frequencies of ~7 and ~17 THz, respectively; in Ar the weaker LJ bonds, with a characteristic frequency of ~1 THz, allow slippage of atoms that inhibits the formation of a hierarchical cage. The maximum displacement would then exhibit *a slow logarithmic dependence on the PKA energy* as depicted in Figure 5.2.

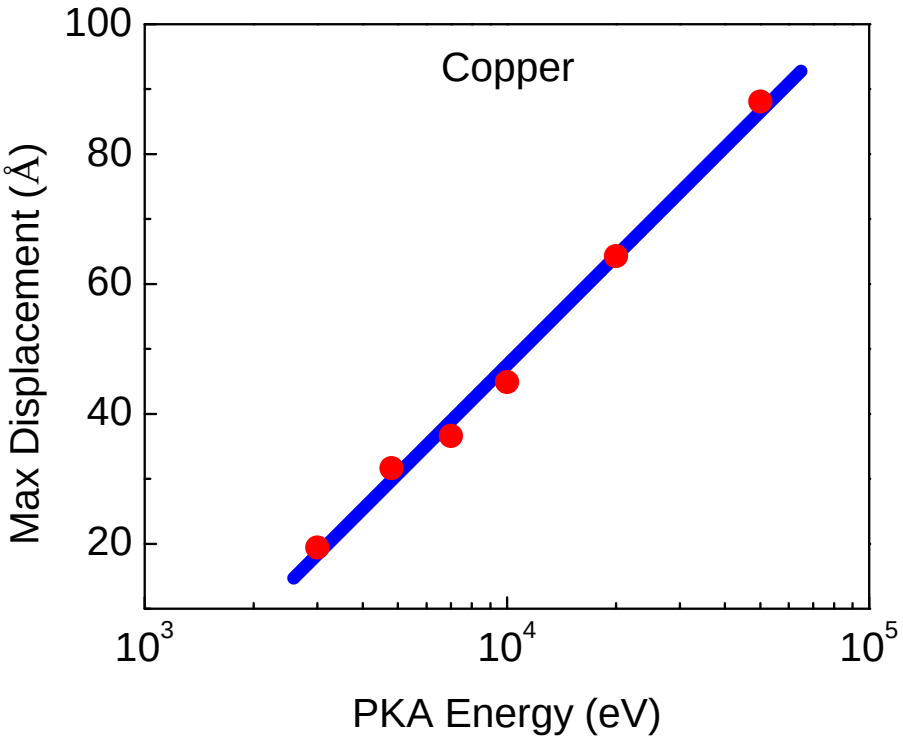

Figure 5.2 Displacement scaling with PKA energy

While sub-cascades become important at higher PKA energies, the mechanism for each sub-cascade still remains the same. Thus, the logarithmic scaling can be exploited to assess a realistic upper bound on the spatial extent of the cascade zone for materials with strong interatomic bonds. We have also observed that the absence of ZBL potential suppresses the local disordering and enhances the ballistic range of the PKA in Cu. The mean velocity of the PKA scales as the inverse of time ($1/t$) and diminishes very rapidly in the initial stages; the recoils generally have a wide distribution in range and commencement time, owing to the hierarchical dynamics.

Several of the PKA neighbors display a temporal and scaling behavior, which is similar to that of the PKA during the ballistic period. However, the range and the velocities of the neighbors are significantly smaller with the marginally displaced atoms engaging in correlated motion at later times. The displacements of 100 neighboring atoms around the PKA are depicted in Figures 5.3–5.5. Interesting differences can be observed among the three materials – in silicon and argon, several immediate neighbors who suffer significant displacements (1 Å or more) have a tendency to return closer to their original sites as evidenced by the rise and drop in the displacements, while in copper, this effect is less pronounced.

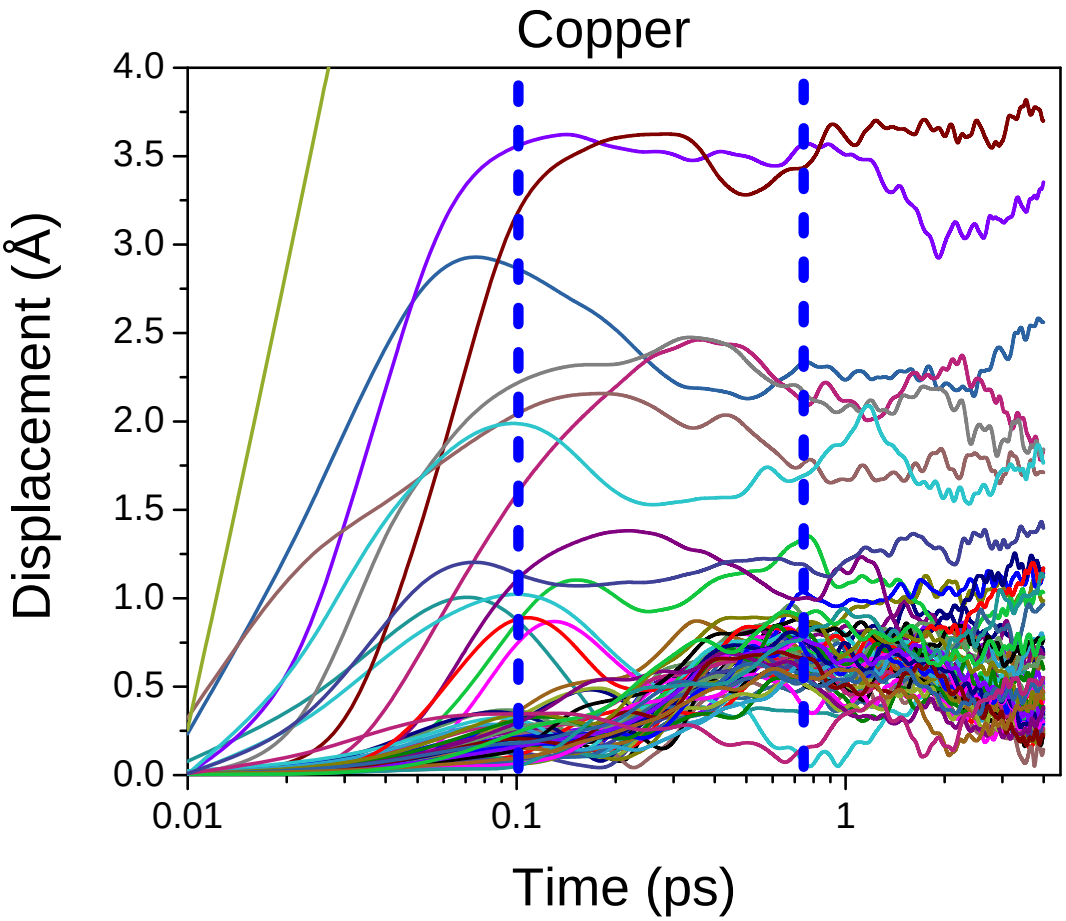

Figure 5.3 Mean displacements of PKA neighbors in copper. $E_{PKA} = 3$ keV.

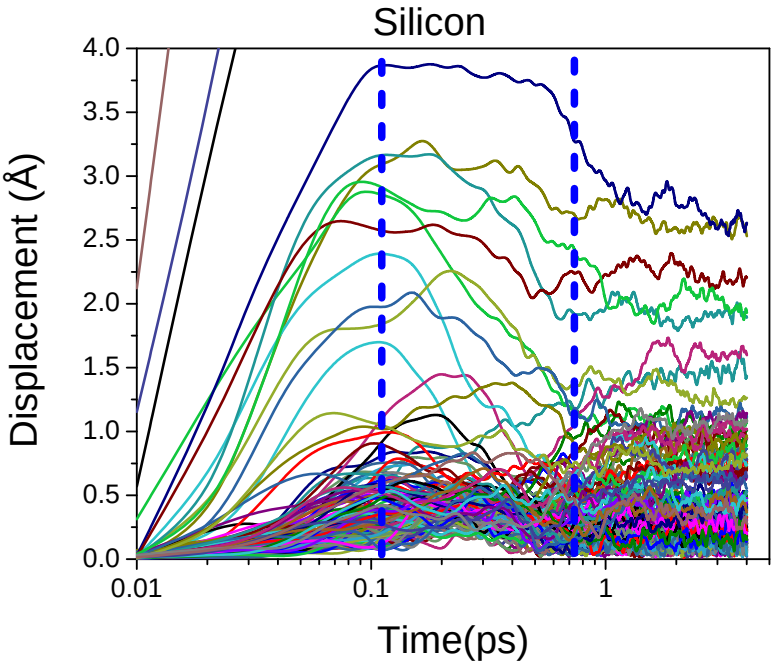

Figure 5.4 Mean displacements of PKA neighbors in silicon. E_{PKA} = 3 keV

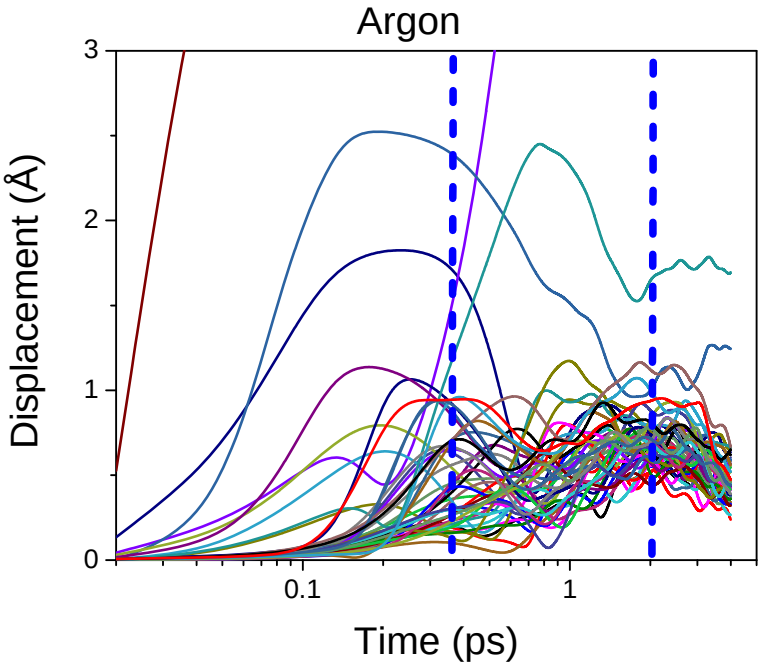

Figure 5.5 Mean displacements of PKA neighbors in argon. E_{PKA} = 100 eV.

The similarities are equally arresting – in all the three materials, there is a group of atoms which suffer small displacements of 1Å or less moving in a concerted manner. For copper, a displacement peak from these less mobile atoms are first observed at ~0.1 ps, which is approximately the time taken for the PKA to cease its motion, and later at ~0.8 ps, which corresponds to the attainment of local thermodynamic equilibrium (and peaking of defects). Analogously, for silicon, there is a discernible peak at ~0.1 ps followed by a burst of displacements at ~0.7 ps, which coincides with the drop and leveling of the displacements of the more mobile atoms (>1Å). For argon, the less mobile atoms have corresponding peaks at ~0.3 ps and 2 ps, respectively. There is no strong evidence for the logarithmic variation in time for the more mobile atoms of Ar, unlike in Cu and Si.

5.3 Non-Equilibrium Energy Distribution from Superpositioning of Two Equilibrium States

As illustrated before, a small group of atoms acquires a higher kinetic energy from the sub-casades. These atoms equilibrate very quickly among themselves in the ballistic/hyperfast stage (~0.1 ps), and therefore, a unique temperature Θ can be assigned to this group of most mobile atoms. Thermal energy transfer from the most kinetic atoms to the 'bulk' region will reduce Θ very rapidly and in the process the 'bulk' temperature T will increase; at longer times a *local* thermal equilibrium will be attained when $\Theta=T$. We have observed that the *non-equilibrium* energy distribution of the local knocked area can be described by a superpositioning of two *equilibrium* Maxwellian distributions, one corresponding to the most kinetic atoms with a temperature Θ, and the other representing the bulk region having a temperature T. First, we will write the two equilibrium Maxwell-Boltzmann distributions as

$$f_T(E)dE = 2\pi\left(\frac{1}{\pi k_B T}\right)^{3/2}\sqrt{E}exp\left(-\frac{E}{k_B T}\right)dE \tag{5.1}$$

$$f_\Theta(E)dE = 2\pi\left(\frac{1}{\pi k_B \Theta}\right)^{3/2}\sqrt{E}exp\left(-\frac{E}{k_B \Theta}\right)dE \tag{5.2}$$

where $\Theta \geq T$. We will next assume that the composite non-equilibrium energy distribution can be expressed as a linear combination given by

$$f(E)dE = \alpha f_T(E)dE + (1-\alpha)f_\Theta(E)dE \tag{5.3}$$

where α is a weight attached to the energy distribution of the 'bulk' region. There is no unique way to determine α; for example, it can be evaluated directly from the MD simulations at different times by tracking the energies of individual atoms. In our analysis, we have evaluated α by the following relationship

$$\alpha = \frac{p}{p+q} \tag{5.4}$$

$$p = \int_0^{E_0} f_T(E)dE \;\; q = \int_{E_0}^{\infty} f_\Theta(E)dE \tag{5.5}$$

where E_0 is the approximate (energy) boundary between the two distributions determined by the condition:

$$f_T(E_0) = f_\Theta(E_0) \tag{5.6}$$

We can show that

$$E_0 = \frac{3/2}{\frac{1}{k_B T} - \frac{1}{k_B \Theta}} ln\left(\frac{\Theta}{T}\right) \tag{5.7}$$

The temporal evolution of the two-temperature (T, Θ) distribution for different materials is shown in Figure 5.6. As evident, the two-temperature model captures the trend reasonably well except at very short times when the most kinetic atoms are yet to equilibrate among themselves. Strictly speaking, the non-equilibrium energy distribution is dependent on the advection or macroscopic velocities. However, the macroscopic velocities are prominent only in the ballistic/hyperfast times scales and hence, do not contribute significantly to the evolution of the energy distribution at later times.

Copper:

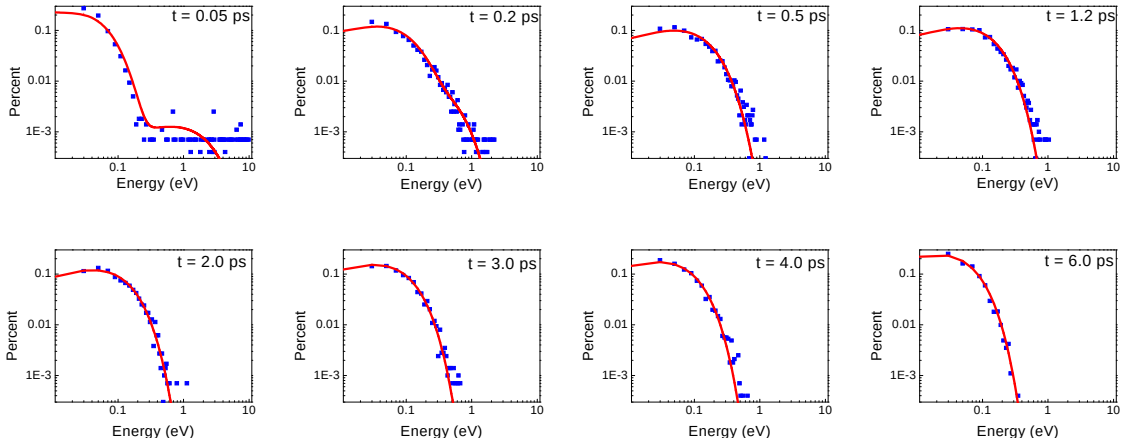

Silicon:

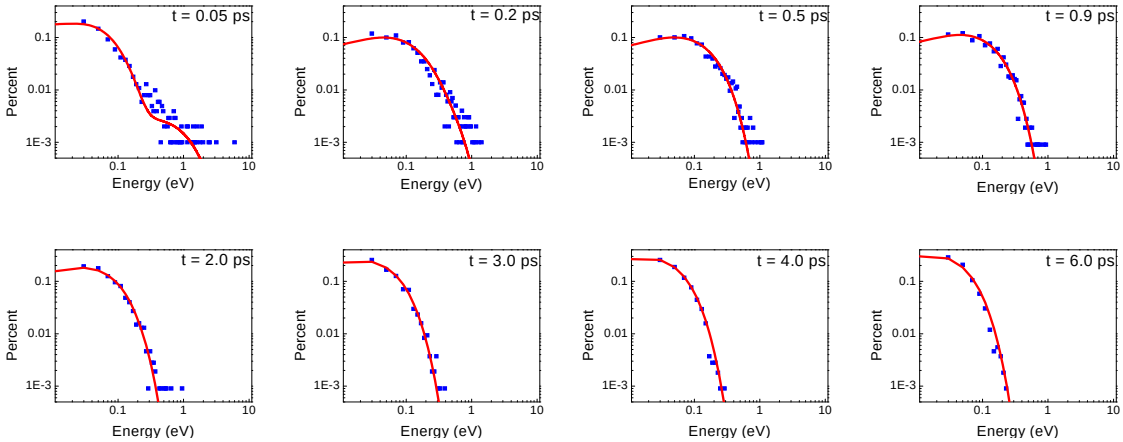

Argon:

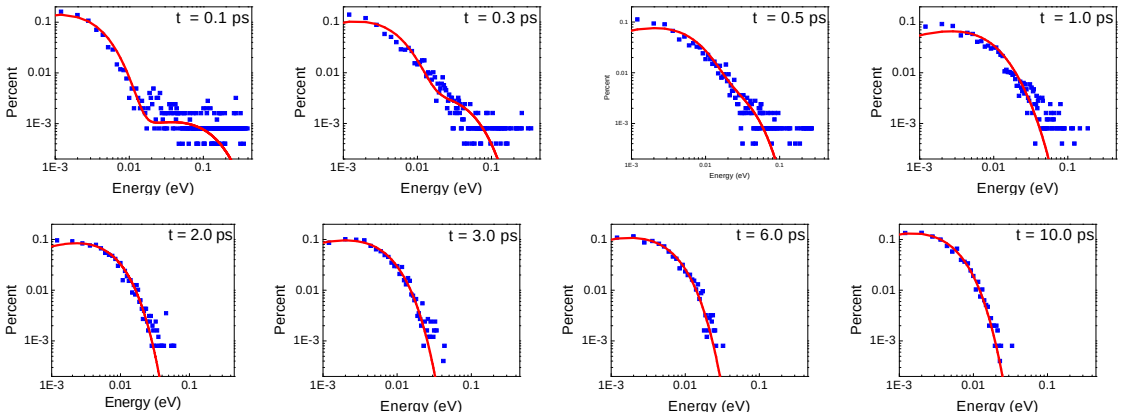

Figure 5.6 The evolution of the non-equilibrium energy distribution for Cu, Si and Ar at different times. The symbols connote data derived from the cascade MD simulations and the line denotes the prediction from the two-temperature (T, Θ) model. E_{PKA} = 3 keV for Cu and Si, and 100 eV for Ar.

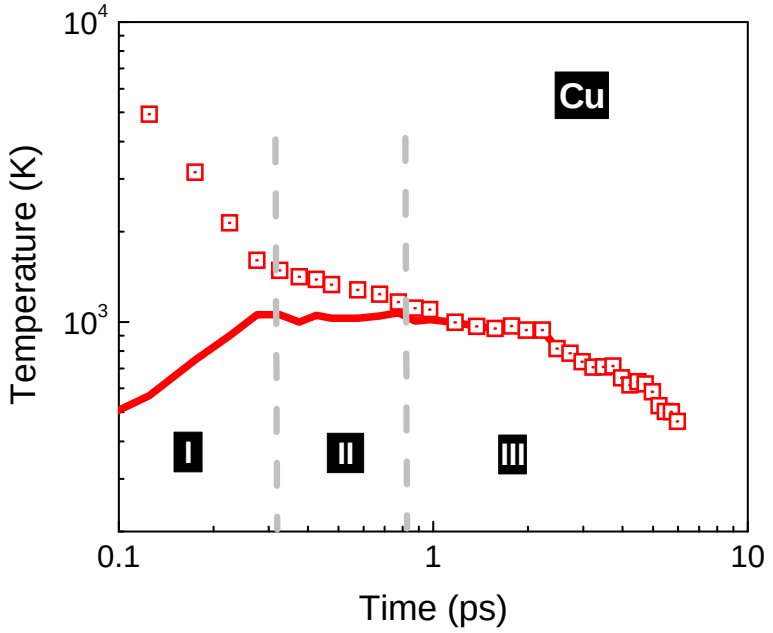

Figure 5.7 Bi-modal temperature variation for Cu (T – line, Θ – symbol). E_{PKA} = 3 keV.

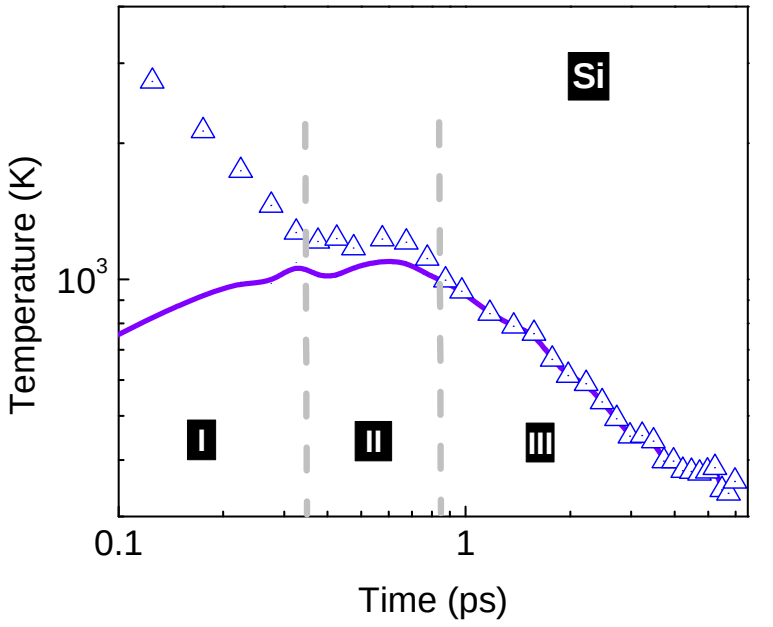

Figure 5.8 Bi-modal temperature variation for Si (T – line, Θ – symbol). E_{PKA} = 3 keV.

In Figures 5.7-5.9, we delineate the evolution of two temperatures – Θ, which is the temperature of the most mobile atoms and *T*, which corresponds to the 'bulk' region that receives the energy from the mobile atoms.

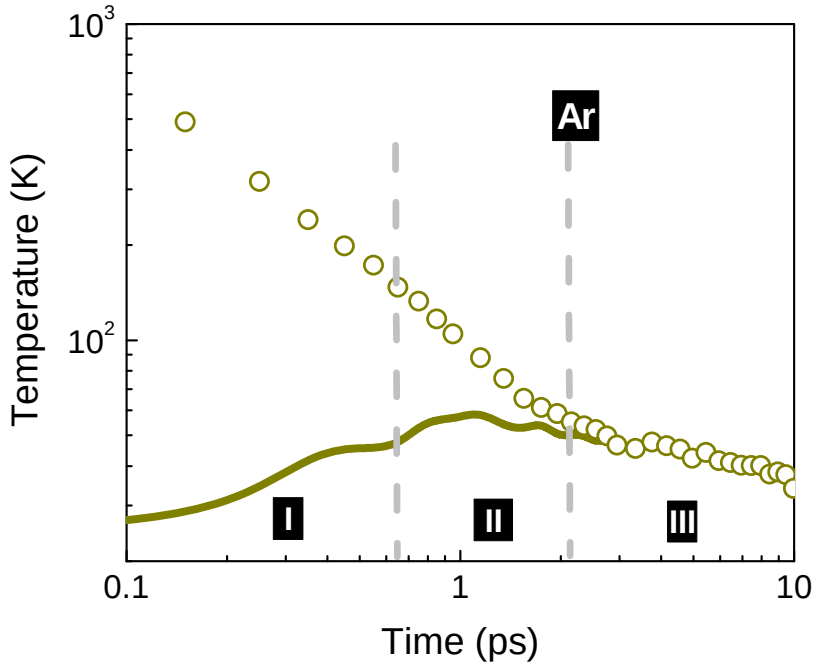

Figure 5.9 Bi-modal temperature variation for Ar (*T* – line, Θ – symbol). E_{PKA} = 100 eV.

In the first stage, Θ swiftly decreases with a power-law variation until ~0.3 ps for both Cu and Si, followed by a plateau-like variation. The bulk temperature *T*, on the other hand, increases in the first stage and approaches Θ gradually during the plateau (second stage) indicating a slower advance to local thermodynamic equilibrium; the approach, expectedly, is fastest for Cu and Si (~0.8 ps) and slowest for Ar (~2 ps). In the third stage, Θ and *T* are indistinguishable from each other and they decay with different rates for different materials. Inspection of the atomic configuration, also inferred from Figure 5.10, reveals that atoms are most displaced when local thermodynamic equilibrium is attained (Θ≈*T*). Thus the dynamic recovery advances under *local thermodynamic equilibrium*. Since the local temperatures during recovery are in the vicinity of the melting point for all the materials – the melting point of Cu, Si and Ar are 1358 K, 1687 K and 84 K, respectively, at zero pressure – the disordered, liquid-like region displays a fascinating recovery progression that gives rich clues to the

structural rearrangement at longer times. We also note that collective dynamics and the emergence of a discernible liquid-like disordered state coincide with the cessation of the PKA motion, which is $O(0.1)$ ps for the strongly bonded materials, Cu and Si. Additionally, the first evidence for a collective behavior that leads to shock propagation and spatial fields, which are low- order moments of the N-atom distribution, is observed in a local region where the PKA motion is arrested; for the softly bonded Ar, sub-cascades drive the eye of the spatial fields further away from the PKA rest location.

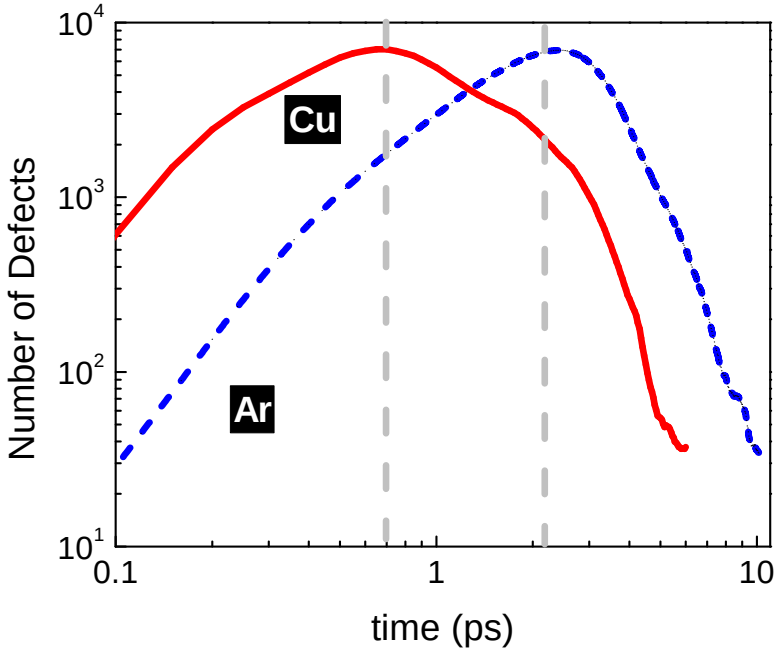

Figure 5.10 Displaced atoms as a function of time with the peaks appearing at $\Theta \approx T$ indicating that the dynamic recovery advances under local thermodynamic equilibrium.

5.4 Radial Distribution Function following Radiation

Figures 5.11-5.13 depict the radial distribution function (RDF) of the local inner region following radiation for Cu, Si, and Ar, respectively. In all the materials, the peaks reduce, which is an indication of partial melting in the local region upon radiation impact. As time progresses, the peaks intensifies again indicating the dynamical recovery process. For the copper, the lowest peak magnitudes are observed around 1 ps, which is consistent with the defect plot. In the silicon the static structural

changes are minimal; however, as shown later, its dynamic structure indicates a supercooled liquid-like state, which is not observed in Cu or Ar.

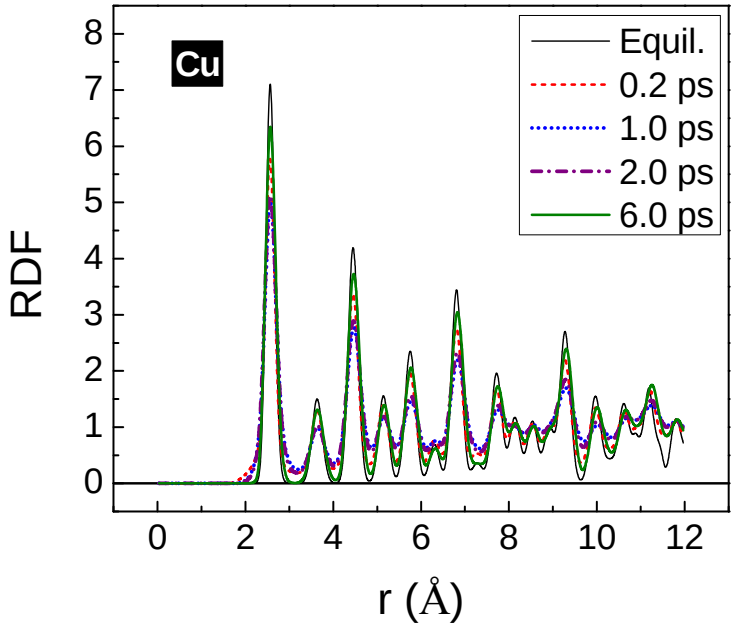

Figure 5.11 RDF of Cu following radiation. $E_{PKA} = 3$ keV.

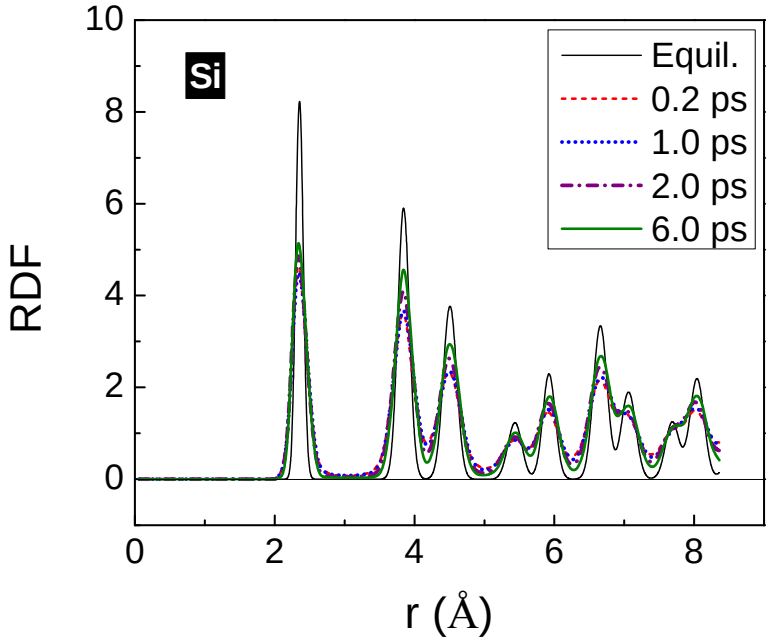

Figure 5.12 RDF of Si following radiation. $E_{PKA} = 3$ keV.

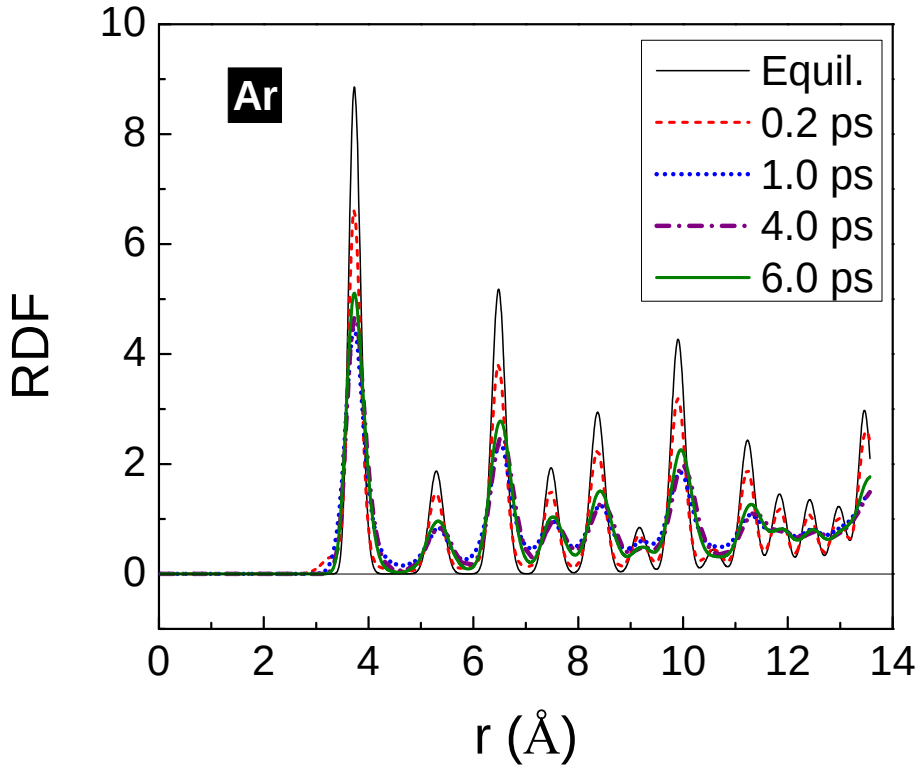

Figure 5.13 RDF of Ar following radiation. E_{PKA} = 100 eV.

5.5 Interplay between the Shock Fields and the Transient Defects

In this section, we delineate the thermodynamic, hydrodynamic and defect fields for Cu, Si and Ar. Two thin slivers are chosen to illustrate the propagation of the fields. The first sliver is parallel to the knock direction (*yx* plane) while the second is normal to the knock direction (*yz* plane). Figure 5.14 shows the spatial fields for temperature (*K*), pressure (*GPa*), the displaced atoms (transient defects), and the advection or macroscopic velocity ($u \cdot m/s$) in the *yx* plane for copper, while Figure 5.15 depicts the fields in the *yz* plane for copper.

Copper (*yx*–plane)

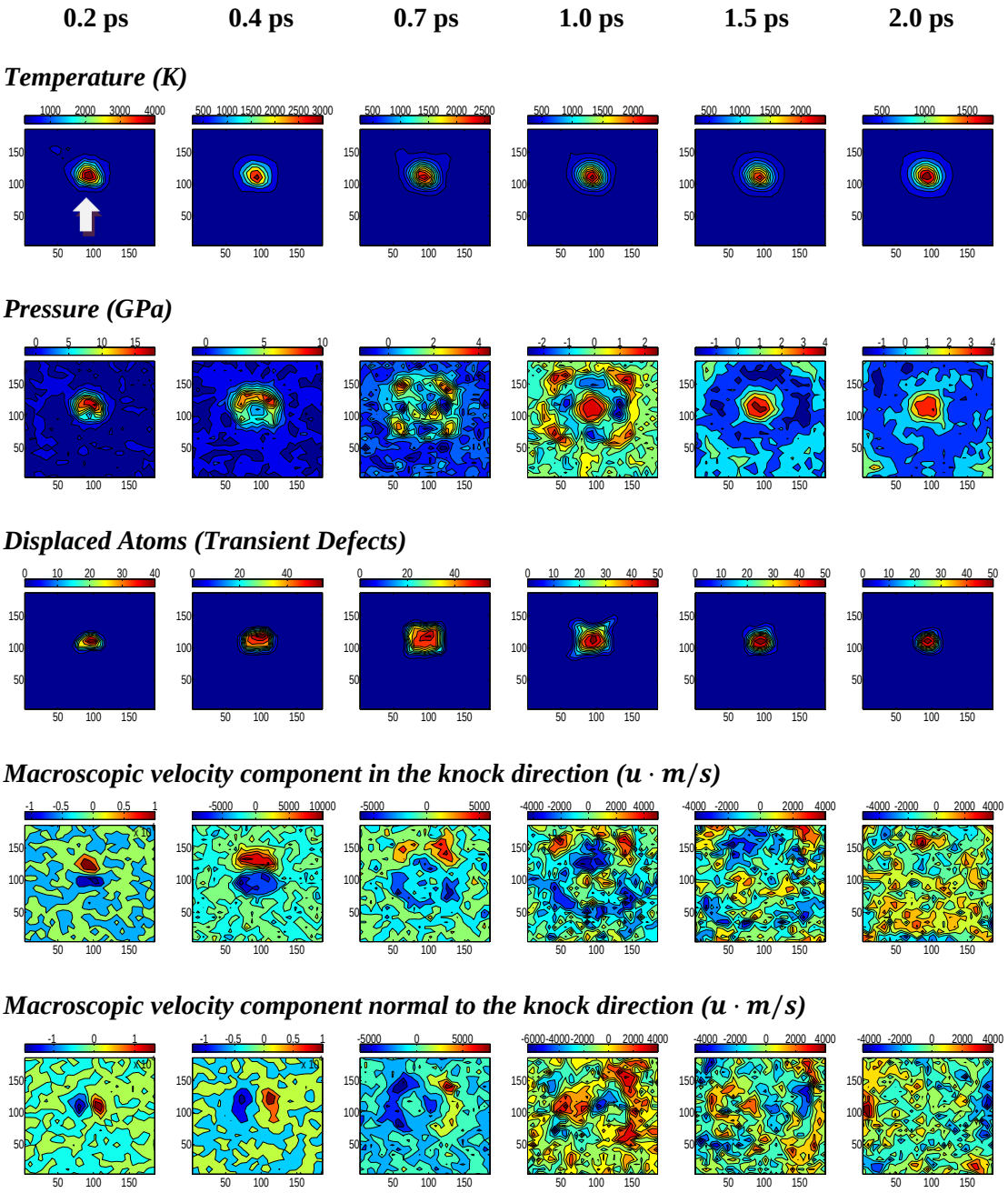

Figure 5.14 The temporal evolution of the spatial fields for Cu in the *yx* plane. The radiation impact is along the *x* direction (shown by an arrow in the top-left sub-panel) at the center of the plane. $E_{PKA} = 3$ keV.

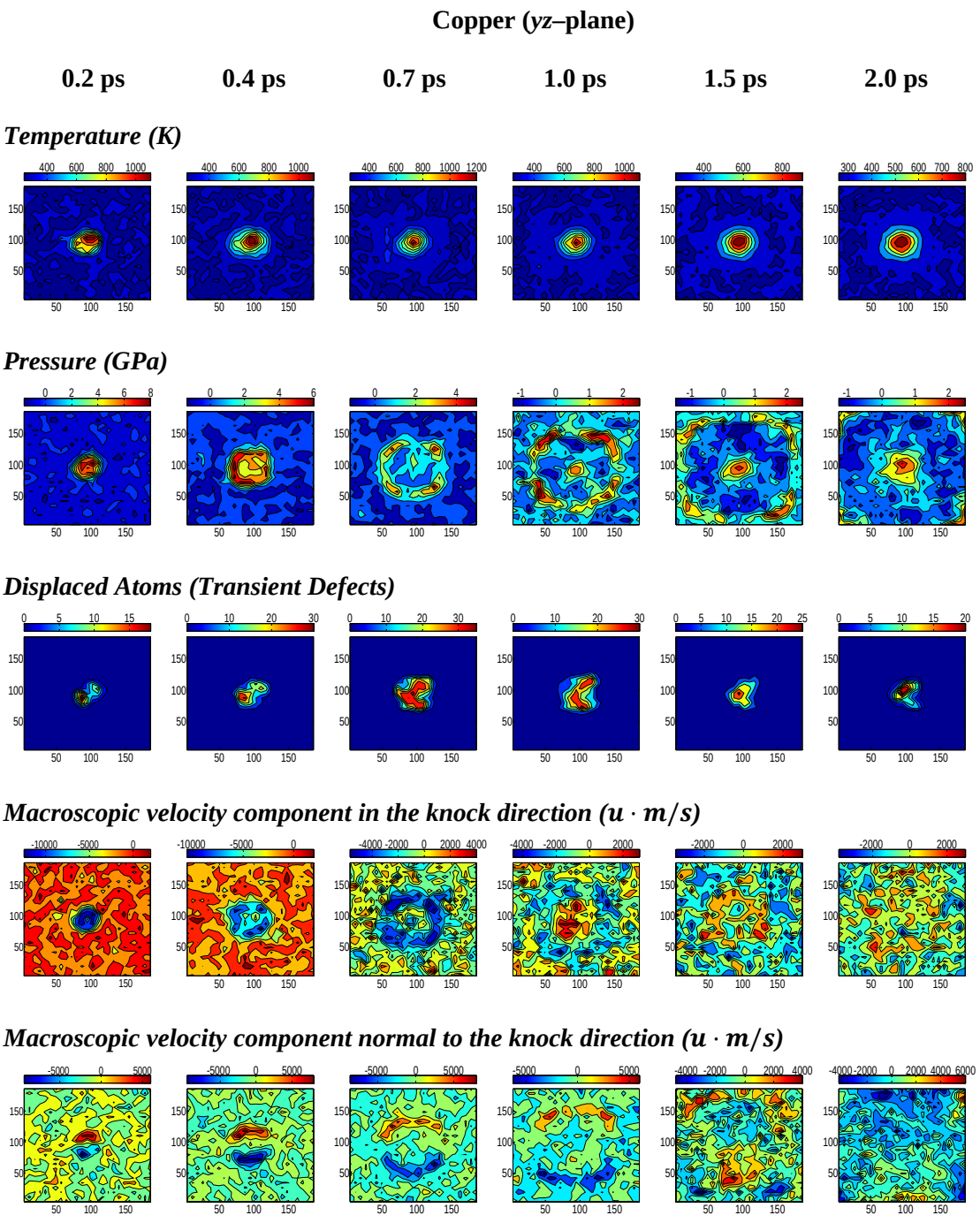

Figure 5.15 The evolution of spatial fields in the *yz* plane (normal to the knock) for Cu. E_{PKA} = 3 keV.

After the PKA comes to rest, which is at the end of the ballistic/hyperfast phase (~0.1 ps), macroscopic spatial fields germinate and become reasonably well-defined by 0.2 ps in Cu. The top two panels in Figure 5.14 depict the evolution of temperature and pressure, respectively. The first

striking aspect is that the eye or the core of the cascade gets displaced in the direction of the impact and it coincides with the displacement of the PKA itself. At 0.2 ps, a well-developed shock field emerges and propagates into the surrounding region. In the early stages, the temperature and pressure are closely coupled and at ~0.7 ps, the pressure wave decouples from the temperature and propagates – indicating its hyperbolic nature – to the boundaries. The propagation is not isotropic for Cu – the shock/pressure wave preferentially chooses the (111) slip planes, also observed in shocked FCC systems [154], resulting in transient slipping and recovery along the <111> directions. As the shock wave detaches, it leaves behind a compressive core region in Cu. Unlike the pressure, the temperature field is dissipative or quasi-diffusional. We have observed that the spatio-temporal evolution of the temperature in Cu can be reasonably described by a diffusive equation, however, only with time-dependent coefficients.

In the thermal spike models, the defects are assumed to be correlated to the temperature field – our simulations show that the transient defect formation (third panel from the top) and recovery are intimately tied to several shock variables as well as to the crystal structure. In particular, the defect panel portrays a strikingly correlation to the pressure propagation and a lack of strong correlation to the temperature field during the dynamic recovery period. More details will be presented in a later publication. The bottom-most 2 panels shows the manifestation of nanoscale vortices, which are generated primarily by the sub-cascades. The macroscopic velocity fields demonstrate that the sub-cascades generate correlated hydrodynamic-like fields, albeit at hyperfast timescales. The macroscopic motion, however, quickly ceases and the transport of momentum and energy continues through the propagation of pressure/shock waves and quasi-diffusion of the heat energy.

Similar behavior is observed in the *yz* plane, which is perpendicular to the knock. It is interesting to note again the near Gaussian profile for the temperature and the detachment of shock waves at ~0.7 ps leaving behind a central core having a positive pressure.

Silicon (*yx*–plane)

0.1 ps	0.2 ps	0.5 ps	0.8 ps	1.0 ps	2.0 ps

Temperature (K)

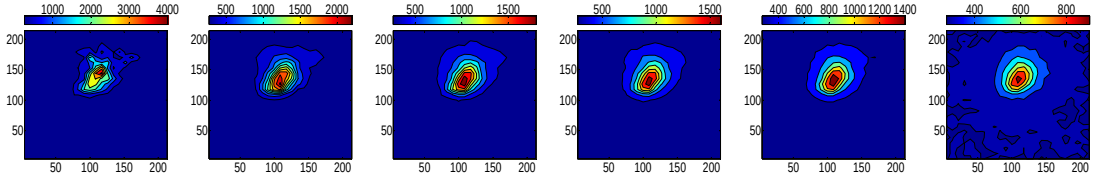

Pressure (GPa)

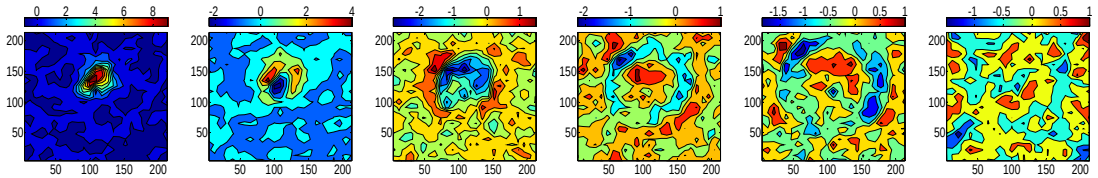

Displaced Atoms (Transient Defects)

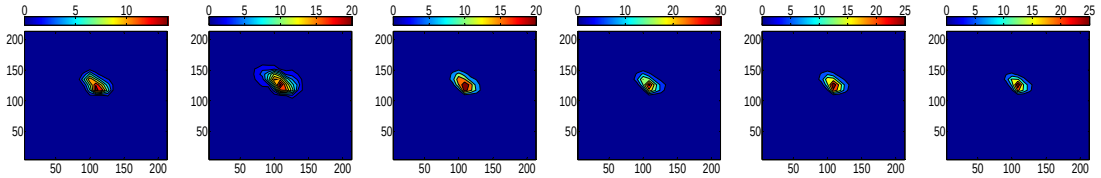

Macroscopic velocity component in the knock direction ($u \cdot m/s$)

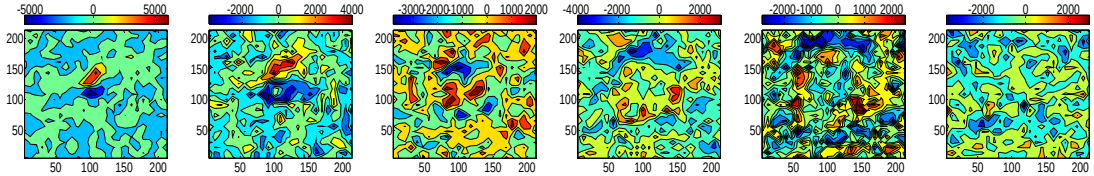

Macroscopic velocity componentnormal to the knock direction ($u \cdot m/s$)

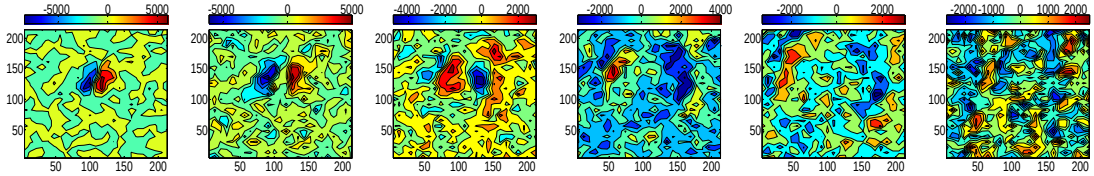

Figure 5.16 The temporal evolution of the spatial fields for Si in the *yx* plane. The radiation impact is along the *x* direction at the center of the plane. E_{PKA} = 3 keV.

Silicon (*yz*–plane)

0.1 ps	0.2 ps	0.5 ps	0.8 ps	1.0 ps	2.0 ps

Temperature (K)

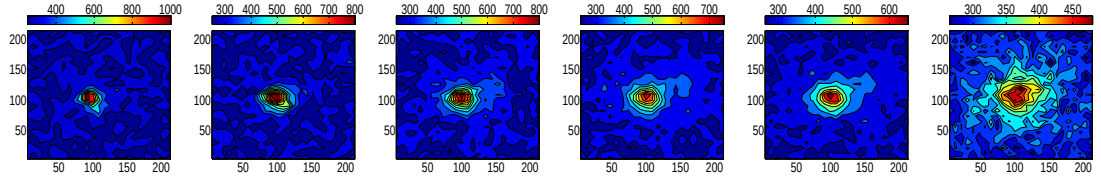

Pressure (GPa)

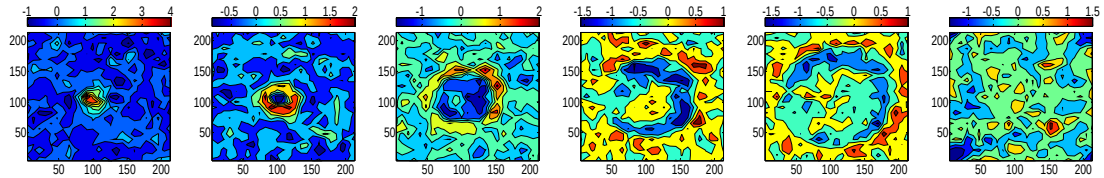

Displaced Atoms (Transient Defects)

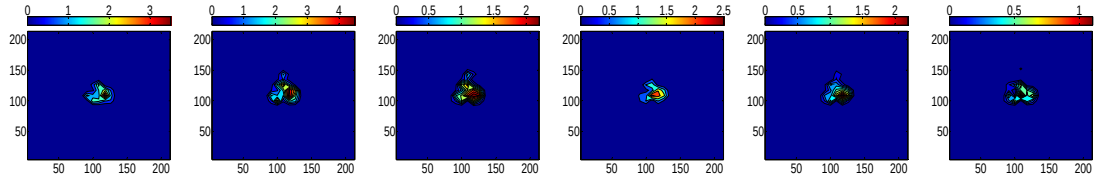

Macroscopic velocity component in the knock direction ($u \cdot m/s$)

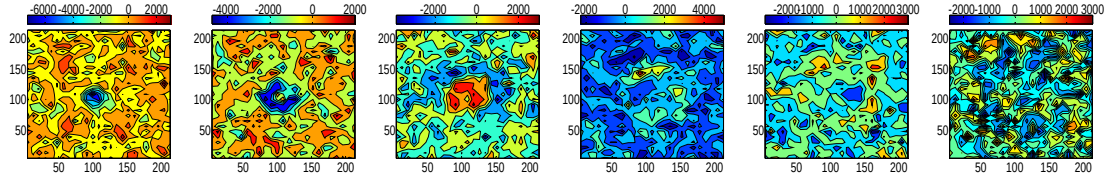

Macroscopic velocity componentnormal to the knock direction ($u \cdot m/s$)

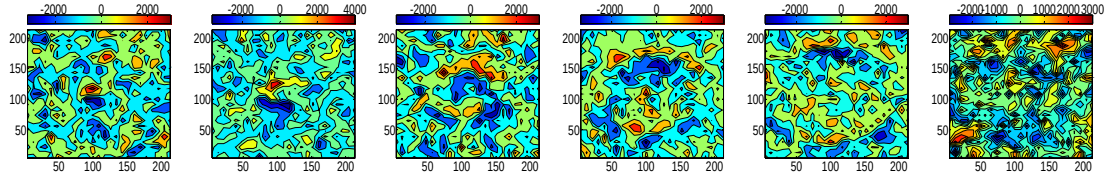

Figure 5.17 The evolution of spatial fields in the *yz* plane (normal to the knock) for Si. E_{PKA} = 3 keV.

In Si, the shock fields are less defined and more fleeting without any directional dependence; they also create less number of displaced atoms though the defects survive for longer time as shown below. The saturation of defects (also see Figure 5.18 below) is consistent with the dynamical peculiarities for Si.

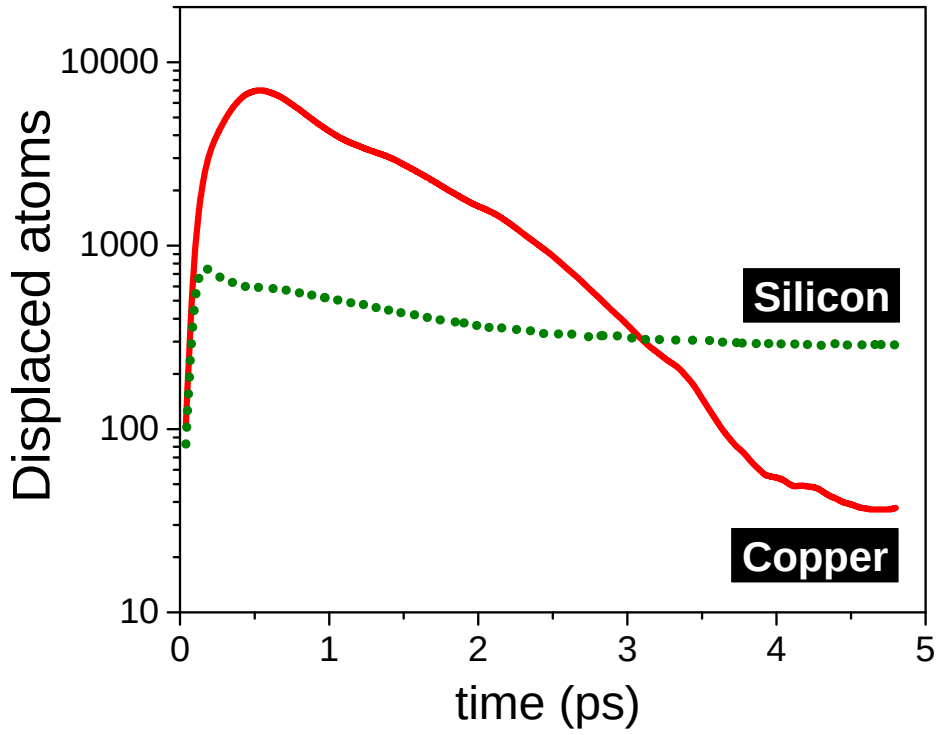

Figure 5.18 Defect evolution in Si and Cu. E_{PKA} = 3 keV for Cu and Si.

The correlation of the transient defects to the pressure propagation can be further evinced in Ar; in Figure 5.19-5.20, we portray the fields in both *yx* and *yz* planes. The defect field in Ar, as in Cu, is not isotropic and it shows a stronger dependence on the pressure/shock field than the temperature field.

Argon (*yx*–plane)

0.2 ps	0.4 ps	1.0 ps	1.5 ps	2.0 ps	4.0 ps

Temperature (K)

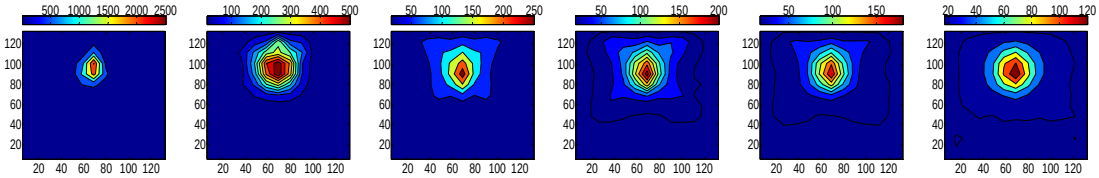

Pressure (GPa)

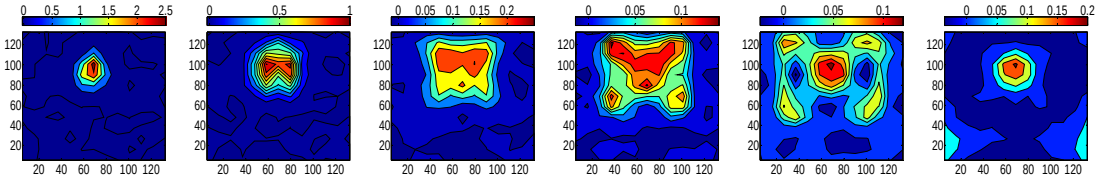

Displaced Atoms (Transient Defects)

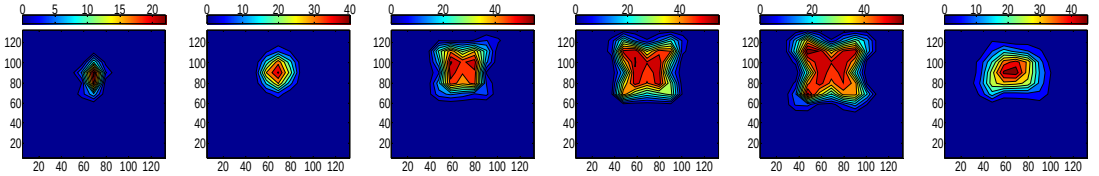

Macroscopic velocity component in the knock direction ($u \cdot m/s$)

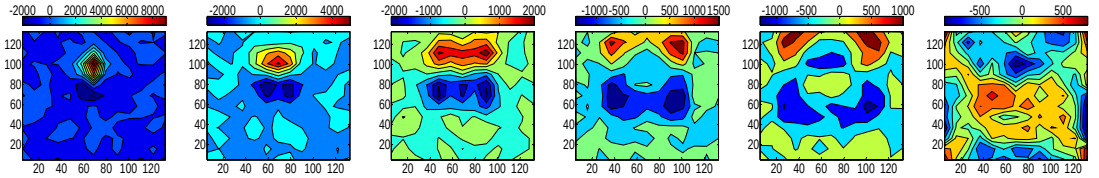

Macroscopic velocity component normal to the knock direction ($u \cdot m/s$)

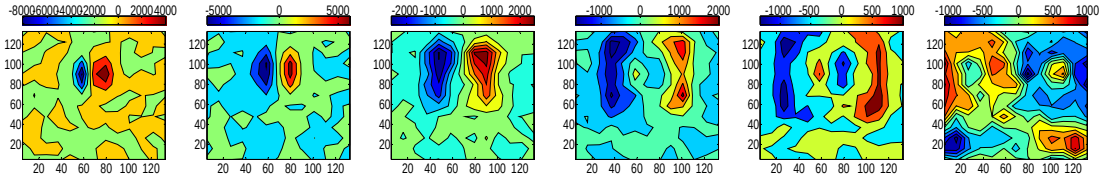

Figure 5.19 The temporal evolution of the spatial fields for Ar in the *yx* plane. The radiation impact is along the *x* direction at the center of the plane. E_{PKA} = 100 eV.

Argon (*yz*–plane)

0.2 ps	0.4 ps	1.0 ps	1.5 ps	2.0 ps	4.0 ps

Temperature (K)

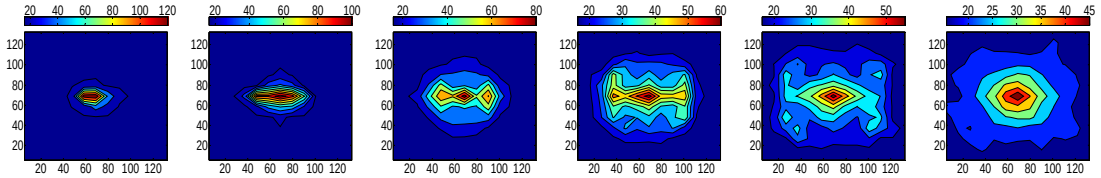

Pressure (GPa)

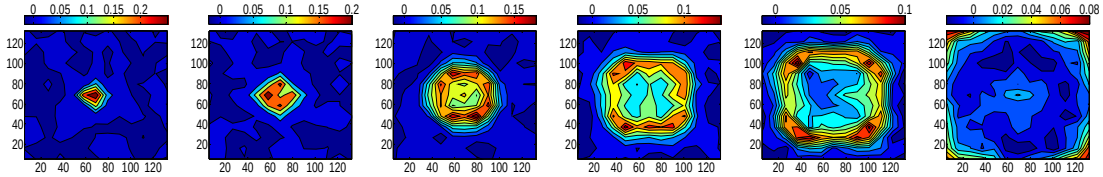

Displaced Atoms (Transient Defects)

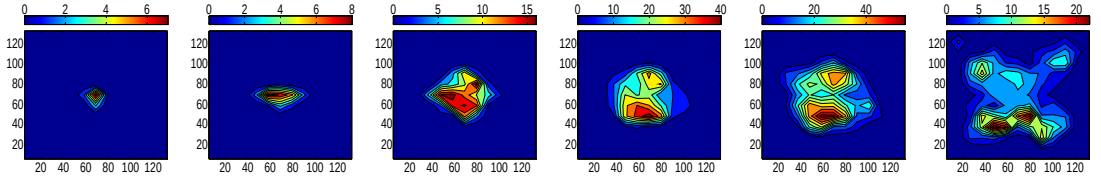

Macroscopic velocity component in the knock direction ($u \cdot m/s$)

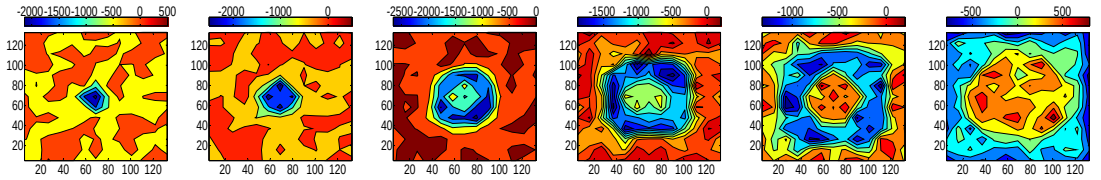

Macroscopic velocity component normal to the knock direction ($u \cdot m/s$)

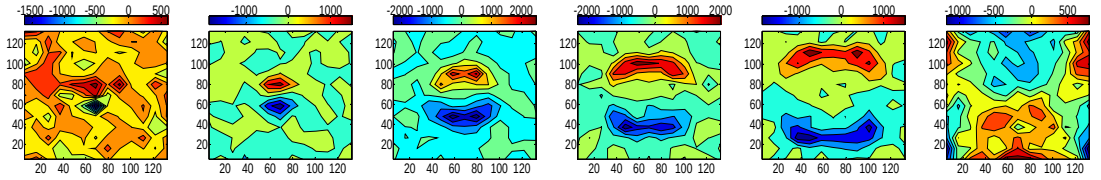

Figure 5.20 The evolution of spatial fields in the *yz* plane (normal to the knock) for Ar. E_{PKA} = 100 eV.

5.6 Stress and Temperature Relaxations

In Section 5.3, we showed the evolution of two temperatures from a model energy distribution. In this section, we compute the temperature and stresses in the fore and wake regions of the inner box – the fore region corresponds to the spatial location ahead of the knock while the wake region connotes the region behind the PKA. The temperature of the fore region, which is plotted in the top right panel of Figure 5.21, shows the general features of the three stages described earlier with the two-temperature model; a power law variation, followed by a plateau-like period and then a slightly faster relaxation. The temperature in the wake region registers only a small increase for all the materials.

Interestingly, the pressure shows a dramatically different behavior; in the fore region, the pressure increases steadily, in fact logarithmically, with time for Cu followed by a sharp drop around 3 ps. In contrast, the pressure does not increase significantly for Si – instead, it goes negative for a brief period of time before relaxing to zero pressure. The final pressure in Cu is positive suggesting the presence of large number of vacancies in the displacement core. Even though the wake regions do not experience a significant temperature change, the pressures change significantly. The pressure in Cu is most pronounced reaching a maximum of ~1.5 GPa followed by a significant reduction. Interestingly, the pressure increases in the wake region for Si but not for the fore region.

At short times following radiation, we have discussed earlier that equipartition may not hold true. In Figure 5.22 we have delineated the three components of the temperatures for Cu, Si and Ar. In the fore region, the deviation between the components for Cu and Si lasts only for ~0.1 ps; in Ar, full equilibration takes place only by 1 ps, approximately, indicating that soft bonds are not very efficient for fast momentum relaxation. It is interesting to see that even though the temperatures do not change significantly in the wake region, there is a discernible difference between the temperature components.

In Figure 5.23 we have portrayed the directional stresses as a function of time. For the fore region, the directional dependence quickly vanishes, within 0.1 ps for Cu and Si. In the wake region, there is evidence for slower relaxation among the components. As with the temperature, Ar, in both regions shows sluggish directional recovery.

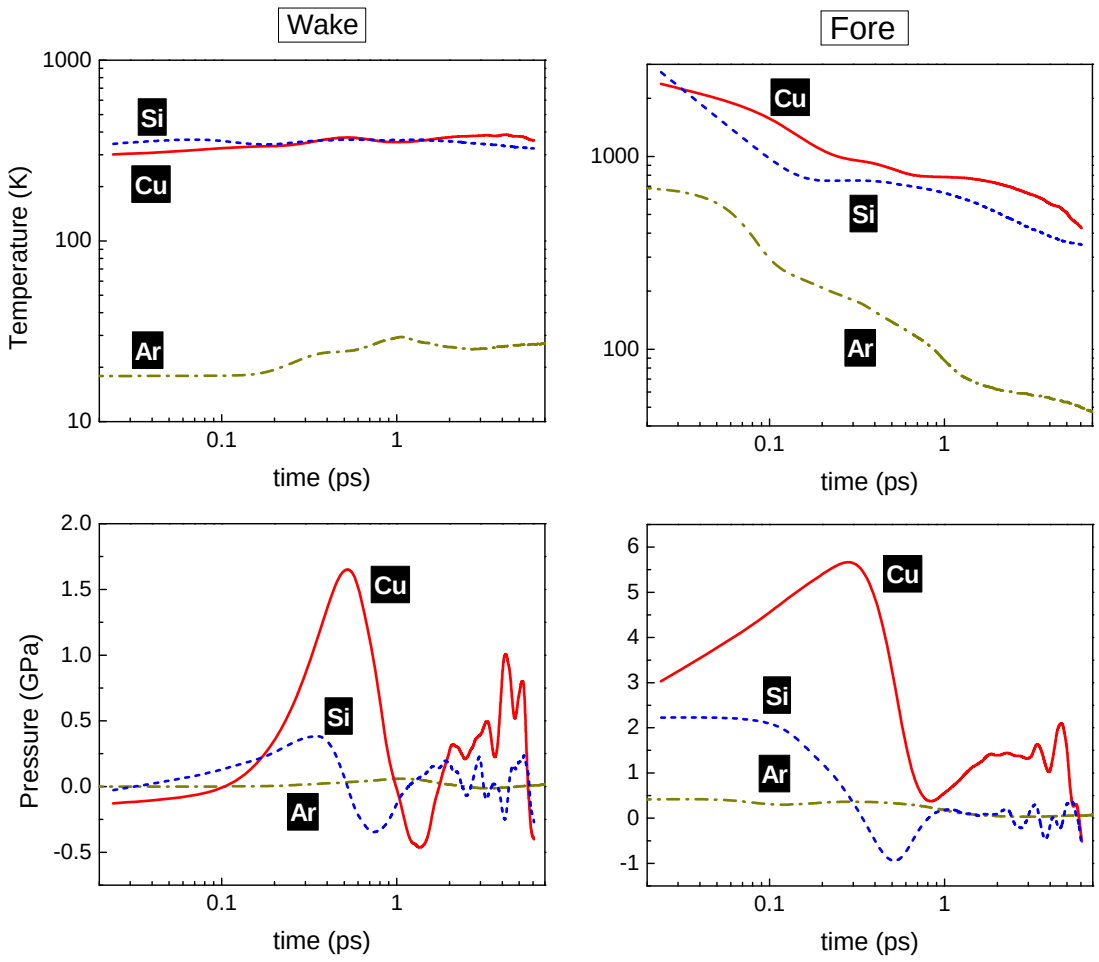

Figure 5.21 Relaxations of temperature (top), and pressure (bottom) following radiation impact. The left and right panels correspond to the wake region behind the PKA and the fore region ahead of the PKA, respectively. Red solid curve is for Cu, blue short dash curve is for Si, and dark yellow dash dot curve is for Ar.

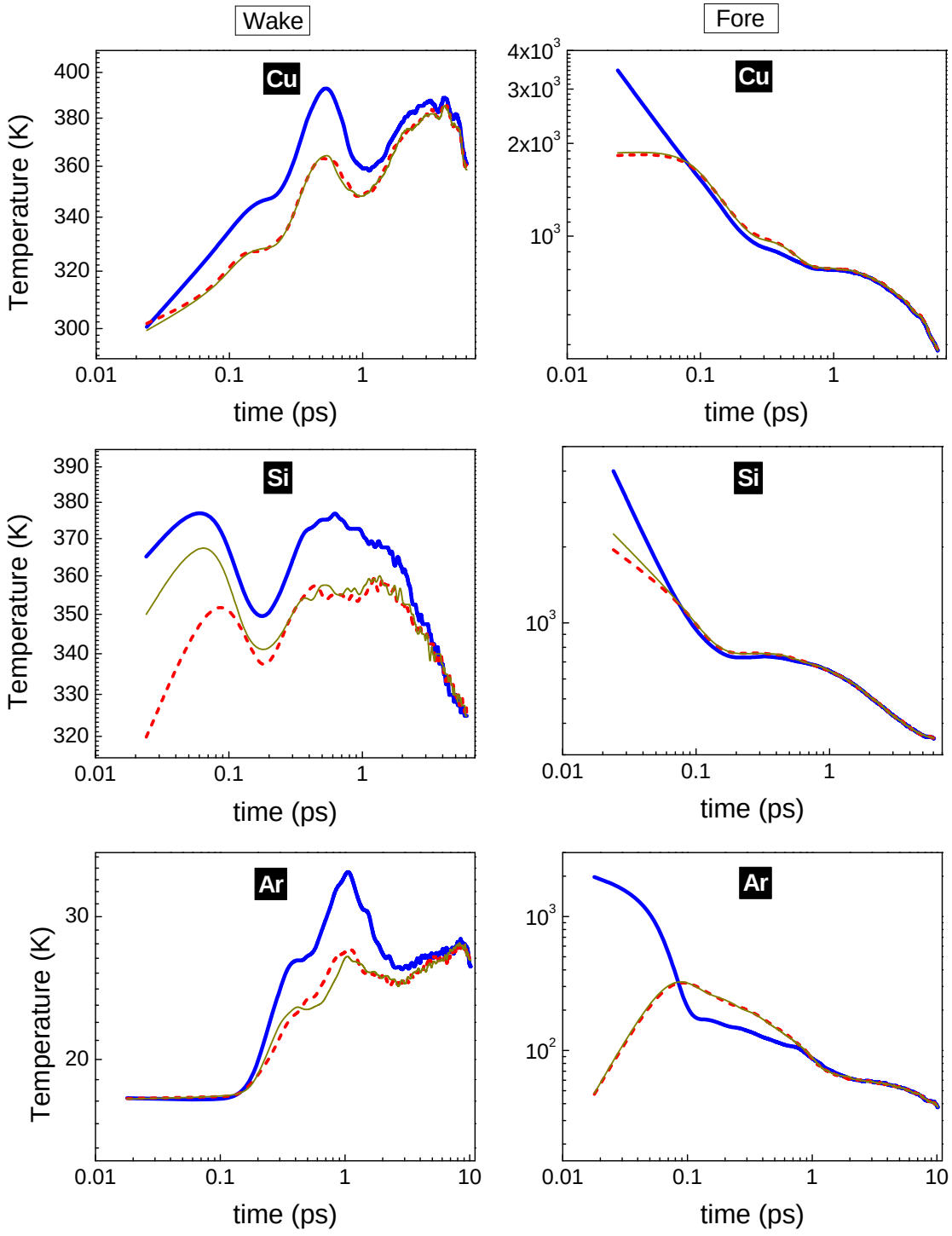

Figure 5.22 Directional temperature relaxations. Blue solid curve is for T_{xx}, red short dash and dark yellow solid curves are for T_{yy}, and T_{zz}, respectively.

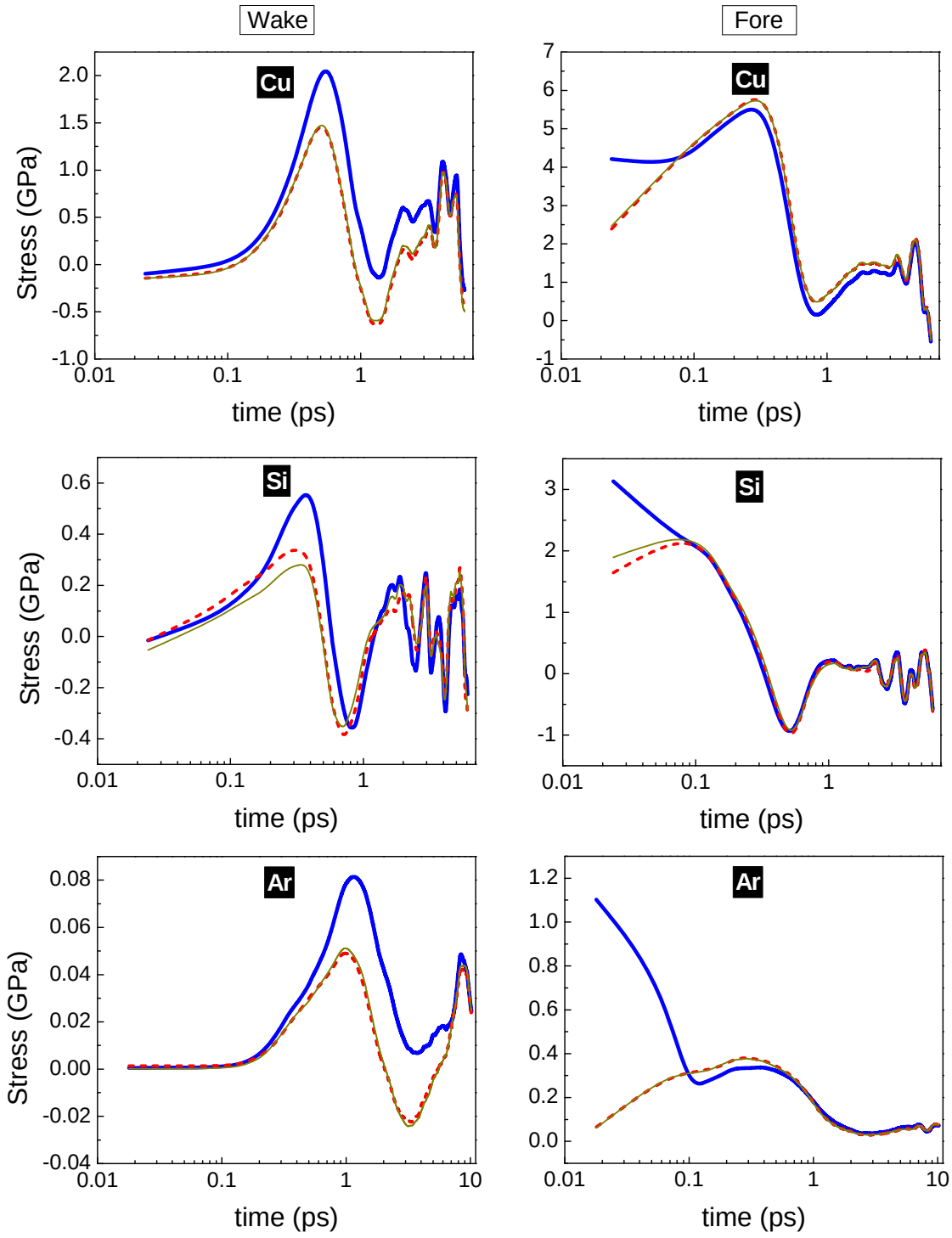

Figure 5.23 Directional Pressure (Diagonal Stress) relaxations. Blue solid curve is for P_{xx}, red short dash and dark yellow solid curves are for P_{yy}, and P_{zz}, respectively.

5.7 Dynamical Heterogeneity via the Evolution of Time-Resolved Van Hove Self-Correlation

In Figure 5.24 we depict the evolution of time-resolved van Hove self-correlation $G_s(\mathbf{r},t)$ for Cu, Si and Ar at different times following radiation impact. The region ahead of the impact (fore) absorbs a significant proportion of the energy from the PKA and hence, becomes most disordered, unlike the wake region behind the knocked atom. The dynamics corresponding to defect initiation and recovery, as shown in Figure 5.24, is markedly different for the fore and wake regions. Two fascinating features can be gleaned from the time evolution: (*i*) $G_s(\mathbf{r},t)$ develops an exponential tail in the fore region for all the three materials, and (*ii*) discernible peaks become prominent in the $G_s(\mathbf{r},t)$ tail at longer times. First, we will discuss the implication of the exponential tail. It has been recently established that $G_s(\mathbf{r},t)$ is a reliable indicator for dynamical heterogeneity (DH) [60] – the manifestation of spatially correlated regions of mobile and immobile atoms in highly frustrated states, typically associated with supercooled and glassy states [43, 56-59]. As indicated in Figure 5.24, the exponential tail in the fore regions becomes well-developed at ~1 ps, which is approximately the time needed to attain a local thermodynamic equilibrium corresponding to the most number of displaced atoms. The exponential tail in $G_s(\mathbf{r},t)$, therefore, establishes a *dynamically heterogeneous recovery* in the fore regions for all the materials. The evolution in the wake regions, in contrast, is conspicuously different; the lack of a prominent exponential tail evinces a homogeneous recovery. The generation of a dynamically heterogeneous region with a large number of mobile and immobile atoms following radiation is not surprising; however, the exponential tail indicates that the subsequent condensation in the fore regions proceeds through a spatially separated, but correlated dynamics.

We will now focus on the peaks – distinct maximas appear in the $G_s(\mathbf{r},t)$ tail when the atoms hop from one site to another [155]. It is interesting to observe that the recovery in Cu, and to some extent in Ar, is punctuated by several identifiable peaks, the locations of which match identically with the nearest neighbor positions before the knock. The more mobile atoms in Cu, therefore, move cooperatively in clusters as they hop between the lattice positions; in contrast, the recovery in Si proceeds through small displacements without prominent lattice hopping. We also observe that the tail characteristics are preserved to longer times illustrating the relative slowness of the recovery processes.

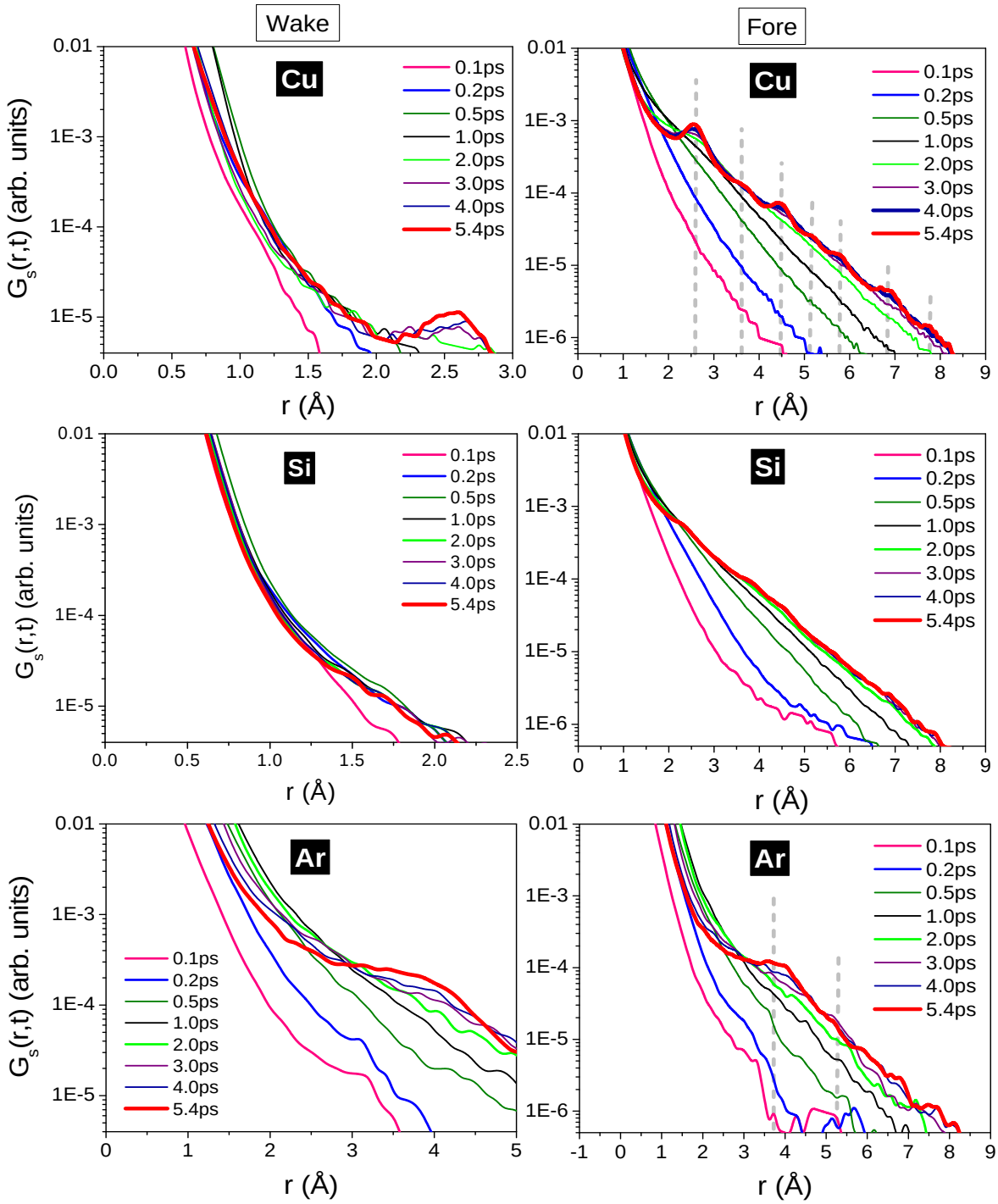

Figure 5.24 van Hove self-correlation function for Cu (top), Si (middle) and Ar (bottom) following radiation impact. The left and right panels correspond to the wake region behind the PKA and the fore region ahead of the PKA, respectively. The exponential tail in the fore regions signifies a dynamically heterogeneous recovery; the peaks in the tail indicate hopping of atoms. The grey broken lines in Cu and Ar (fore) panels indicate the nearest neighbor positions.

5.8 Displacement Distribution

Using the isoconfiguration ensemble, we portray the distribution of the directional displacements following radiation knock in the fore and the wake regions of the inner box – see Figures 5.25 and 5.26. Note that the radiation impact is along the *x* direction.

As illustrated before, the directional displacement metric is expressed as:

$$\langle D_{i,x}(t)\rangle_{ic} = \frac{1}{M}\sum_{k=1}^{M}[x_i(k,t) - x_i(k,0)] \tag{5.8}$$

where, $x_i(k,t)$ is the position in one of the three directions of atom i in ensemble k at time t. We have observed that the displacement distributions do not differ significantly with different starting configurations. Typically, one hundred isoconfigurational copies having different momenta are needed to generate statistically significant displacements in radiation cascade simulations.

At short times following radiation, the displacement distribution is nearly Gaussian and centered at origin, but changes its character as time progresses. Very interestingly, for Cu and Ar in the wake region, the atoms move *backwards*, opposite to the direction of the knock (+*x* direction). At the same time, there is bi-modal distribution in the transverse directions (*y* and *z* directions). Thus atoms move away from the core leaving behind a region which is rich in voids. In contrast, there is a only a small backscattering effect in Si, which is consistent with the number of defects that have been identified before.

The displacement peaks, plotted in Figure 5.27, show an interesting relationship that mirrors the change for temperature at early times. At very short times, a power-law is manifested followed by a plateau-like stage. No significant directional asymmetry is observed in the displacement peaks.

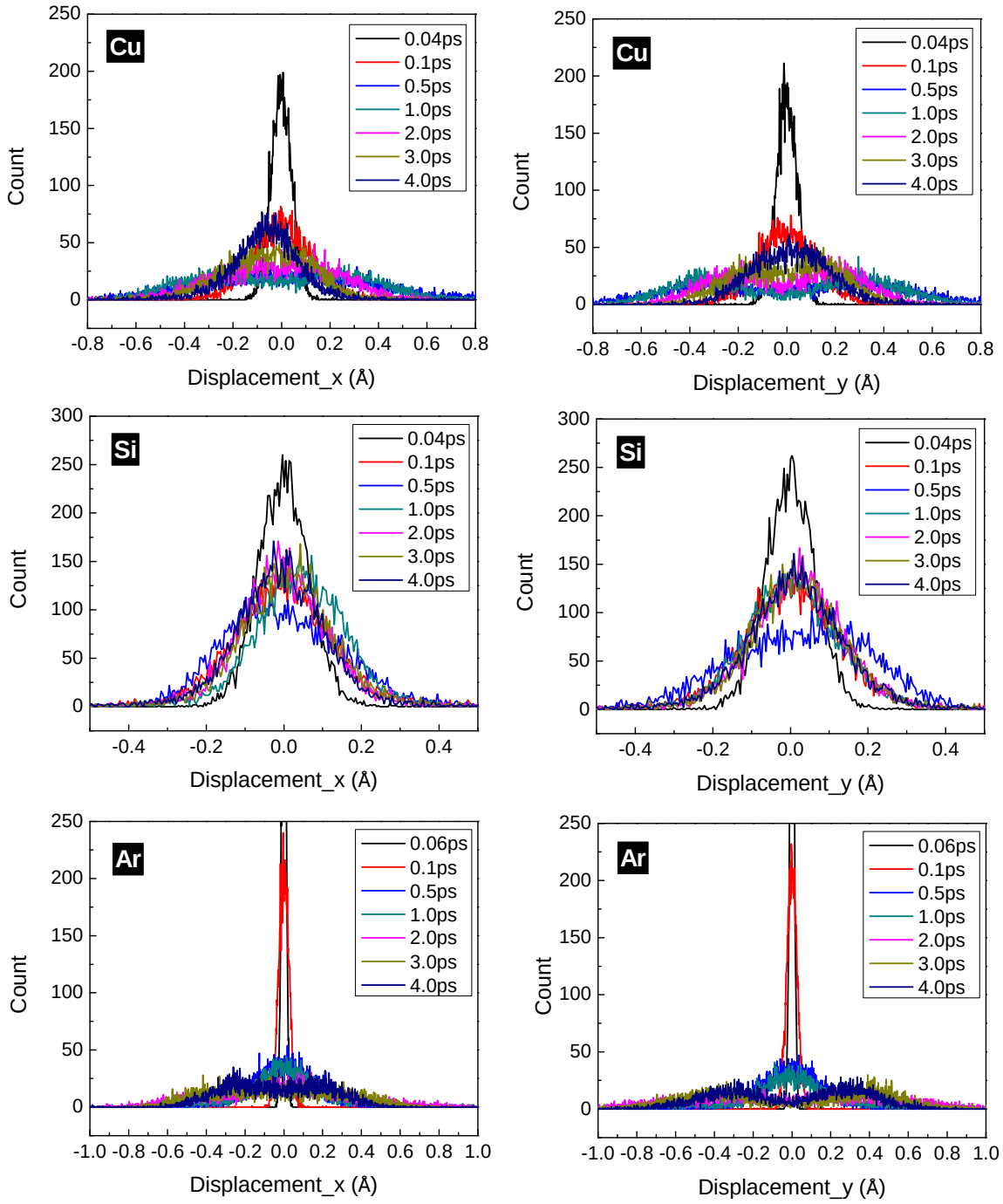

Figure 5.25 Directional displacement distribution in the fore region following radiation impact. The left panel depicts the displacement in the knock (x) direction while the right panel shows the displacement in a transverse (y) direction.

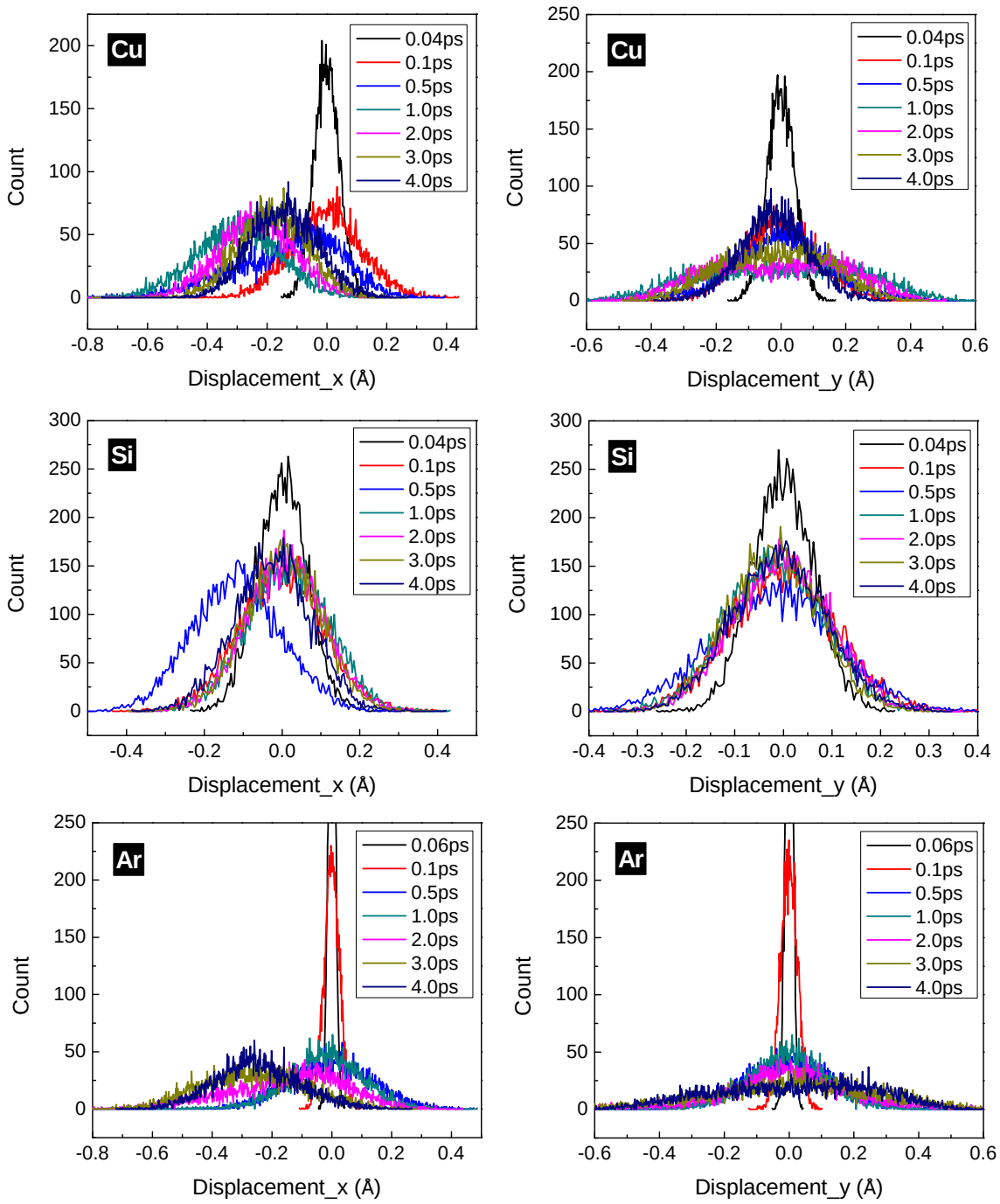

Figure 5.26 Directional displacement distribution in the wake region following radiation impact. The left panel depicts the displacement in the knock (x) direction while the right panel shows the displacement in a transverse (y) direction.

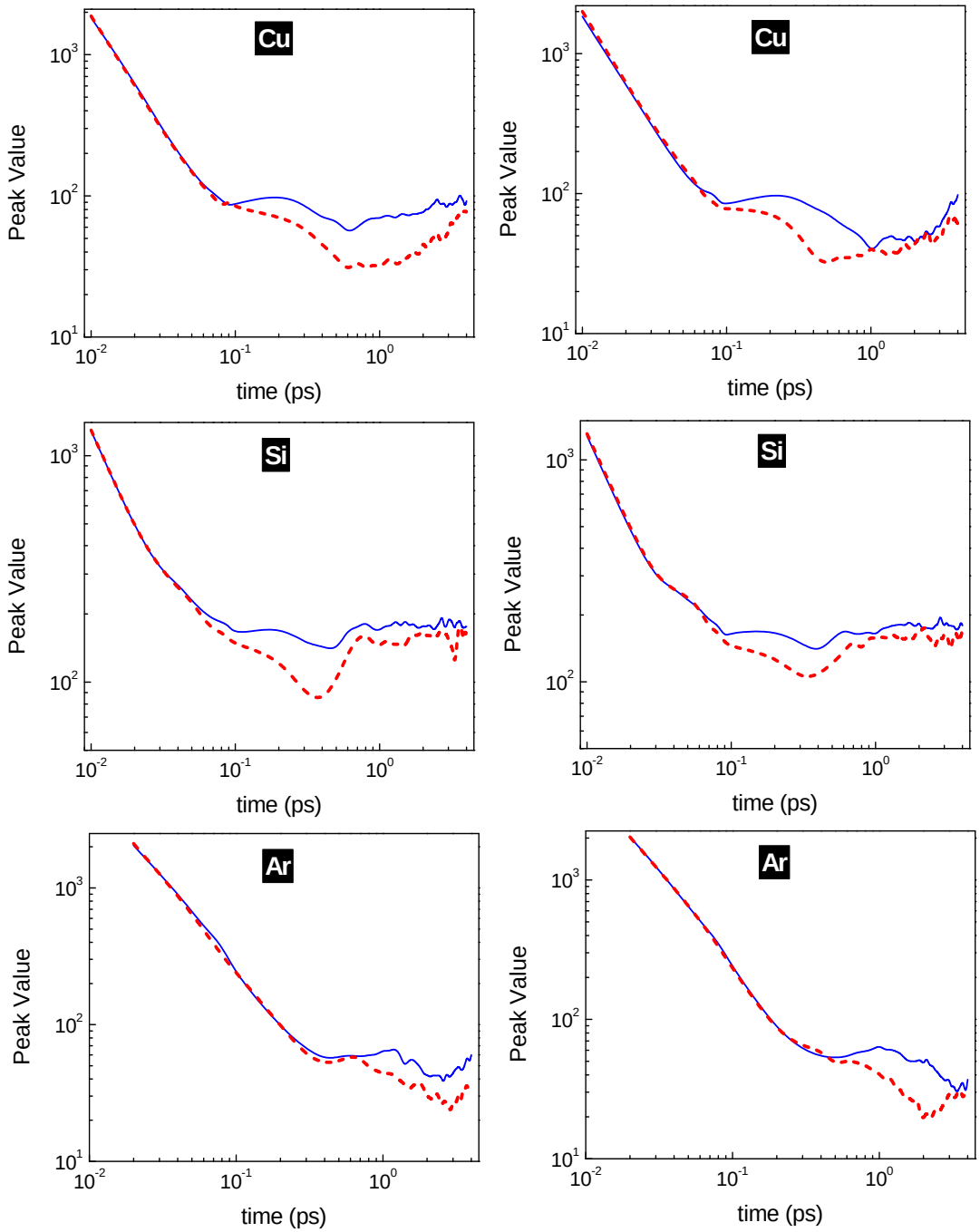

Figure 5.27 Displacement peak value as a function of time following radiation impact. Blue solid curve is for the wake region, while the red short dash curve is for the fore region. The left panel depicts the displacement in the knock (x) direction while the right panel shows the displacement in a transverse (y) direction.

5.9 Dynamical Recovery

The fascinating dissimilitude between the dynamical recovery in Cu, Ar, and Si is further portrayed in Figure 5.28 through an isoconfigurational analysis in which M identical copies of the same configuration are allowed to evolve after radiation impact followed by averaging the displacement of each atom over the M copies. In Figure 5.28, the red spheres/dots correspond to the most mobile atoms (top 20%) that are generated by radiation impact, while the green spheres represent the most immobile atoms (bottom 20%). It is intriguing to observe that the more mobile atoms in Cu become less mobile through a percolating, fractal-like dynamic front that advances through a hopping mechanism as evidenced from $G_s(\mathbf{r},t)$, while in Si, the mobile and immobile atoms form spatial clusters that show large amplitude oscillations. The mean fractal dimension of the most mobile atoms in Cu is less than 2, whereas it is ~2.8 for Si indicating a striking fractal or dendritic condensation front in Cu.

The dynamic response of Cu, Si and Ar is further drawn out through the time-resolved density correlator in Figures 5.29-5.31; the equilibrium variation is depicted in Figure 5.32. An interesting directional anisotropy is observed in the relaxation behavior – the density correlator in Cu and Ar relaxes slower in the knock direction, which is along [1,0,0], relative to the transverse directions. Nevertheless, the relaxation in all the directions decays to near zero for Cu within a few picoseconds, similar to that of typical liquids. In comparison, Ar has a relative slower relaxation.

Remarkably, the density correlator for Si does not decay connoting a supercooled liquid-like behavior. It is known that Si will be amorphized under continued irradiation, unlike Cu, and it is quite remarkable that we have observed vastly different dynamical correlations in Si, even at short timescales, that portend the transition to an amorphous phase. Interestingly, the knock direction oscillations are somewhat out-of-phase to those in the transverse directions, which suggests the presence of an anisotropic 'breathing' mode as the system recovers.

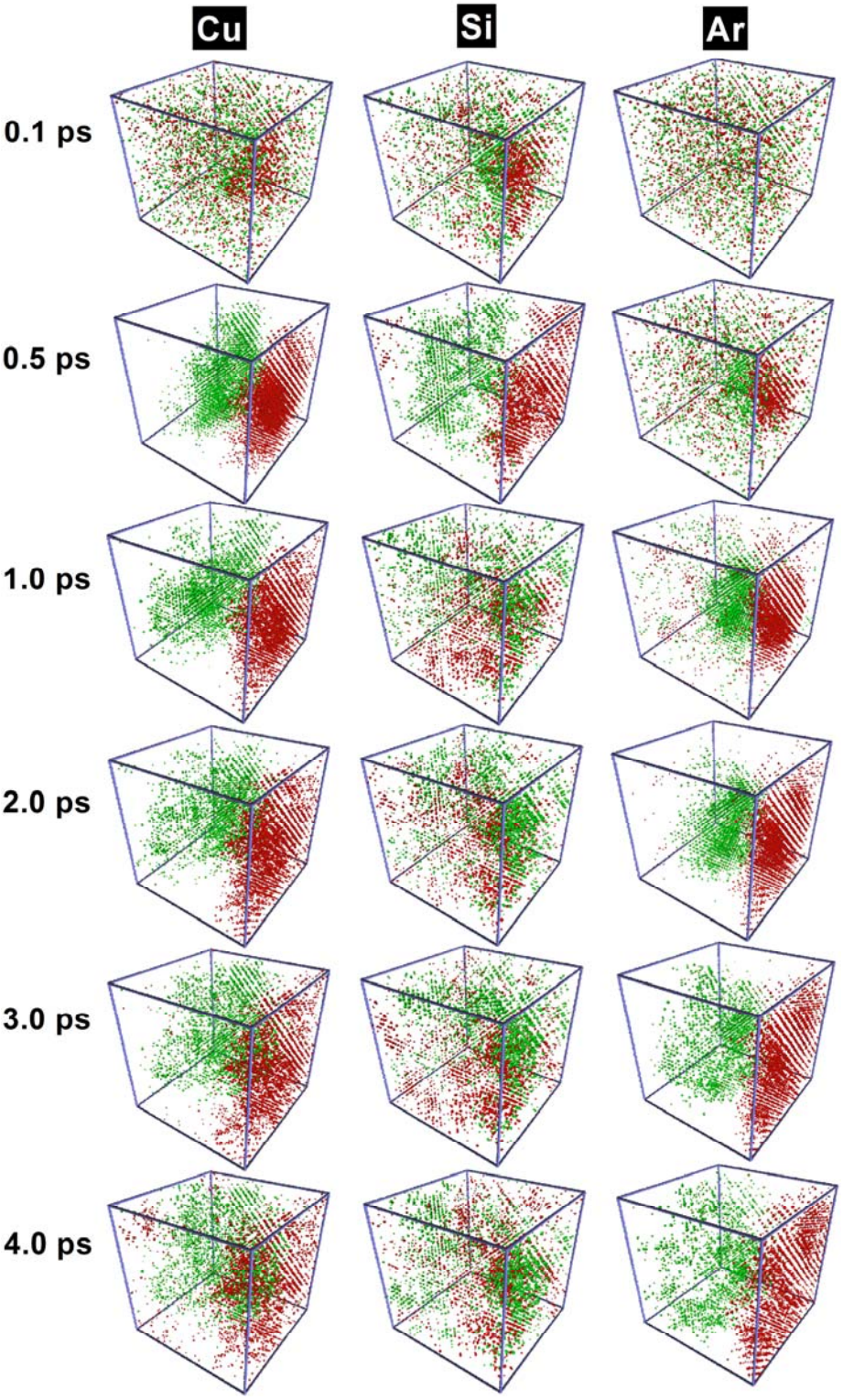

Figure 5.28 Most mobile (top 20%, red) and most immobile (bottom 20%, green) atoms at different times for Cu and Si following radiation impact.

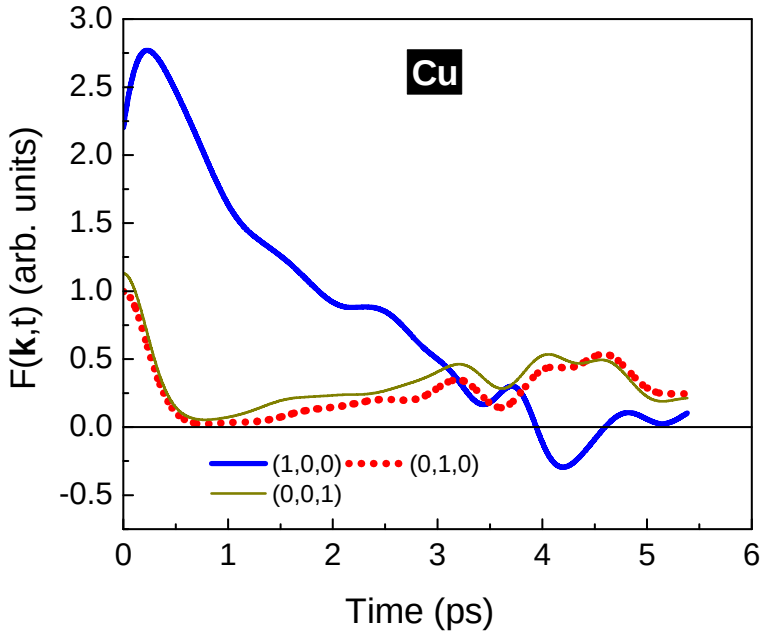

Figure. 5.29 Time-resolved density correlator for Cu following radiation impact.

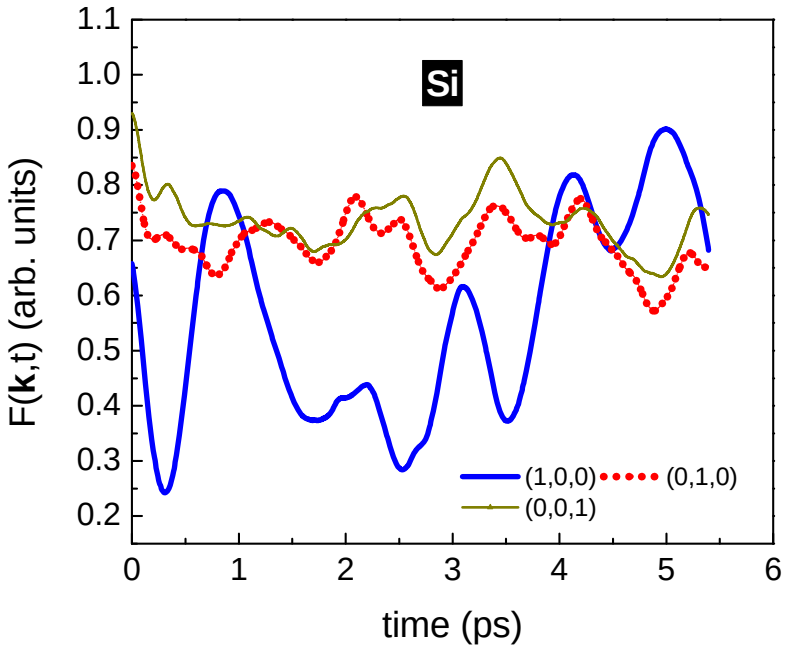

Figure. 5.30 Time-resolved density correlator for Si following radiation impact.

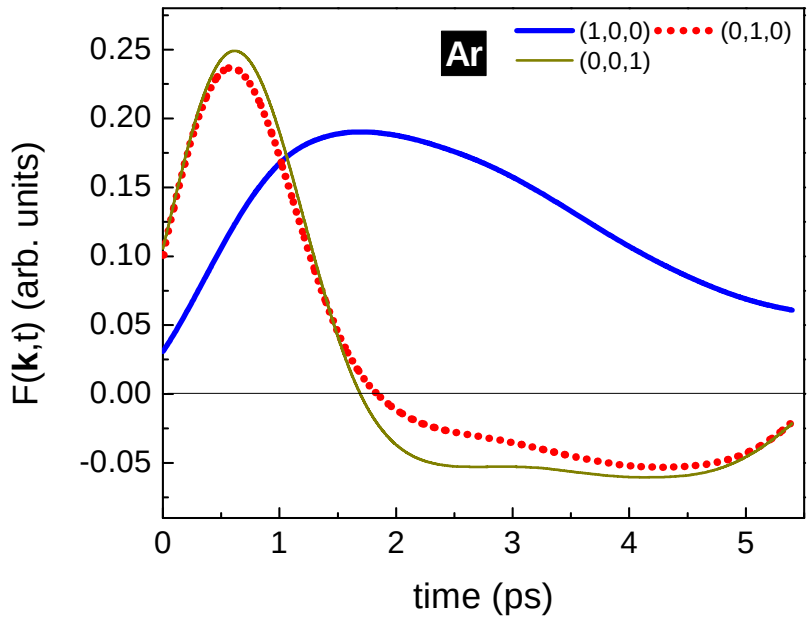

Figure. 5.31 Time-resolved density correlator for Ar following radiation impact.

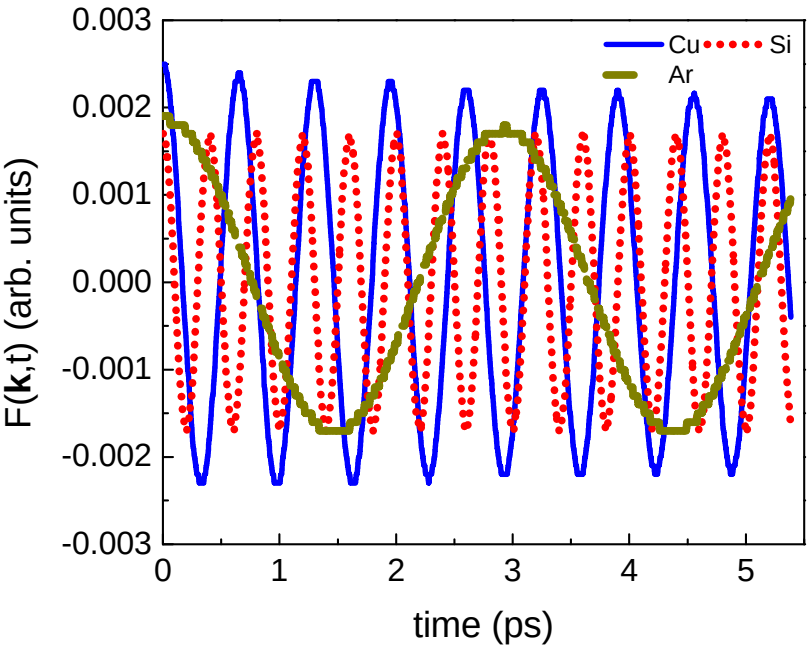

Figure. 5.32 Time-resolved density correlator for the equilibrium state.

Chapter 6. Conclusions

Radiation impact generates a transient disordered phase, which in the past has been considered generically as liquid-like. While the evidence for a metastable liquid-like state has been compelling before, its dynamical characteristics have been unknown thus far. A liquid state has rich and defining attributes that primarily manifest from strongly correlated dynamics; recent evidence from metastable supercooled liquids portray an intriguing structural arrest emerging from spatially correlated regions of mobile and immobile atoms, which is defined as dynamical heterogeneity [63, 156]. The objective of the current work has been to identify metrics that bring out the complex dynamical correlations in materials as they respond to radiation.

In this investigation, we make quantitative predictions on correlated dynamical motion of the atoms as the liquid-like state is formed and condensed following an ion or neutron impact – our simulations on three materials (copper, silicon and argon) having very different bond structures reveal an anisotropic and heterogeneous dynamical structure. Of utmost importance are *dynamical correlations during the recovery period*, which corresponds to the condensation of the liquid-like state that determines the final defected state.

Using molecular dynamics (MD) simulations and with the appropriate non-equilibrium shock physics formalism, we have reported the first evaluations of the dynamical metrics of the liquid-like state through the intermediate scattering function or density correlator and van Hove self- correlation function, along with a host of defect, thermodynamic and hydrodynamic field data following a confined ion/neutron impact; the correlation functions can also be experimentally accessed or inferred from state-of-the-art ultrafast pump-probe experimental methods [32, 62]. The hopping mechanism from the van-Hove self-correlation, the fractal-like condensation and the fast decay of the density correlator attest to a rapid defect recovery in Cu. In contrast, silicon portrays spatially-separated regions that resist recovery to the underlying lattice structure, and exhibits a non-decaying density correlator that is strikingly similar to a supercooled liquid.

Evidence from ion hammering [107] and pump-probe experiments [35] suggests the occurrence of a liquid-liquid phase transition in Si – from a high density liquid to a low density liquid [63, 84] – before Si is amorphized; the inference, however, is based on indirect interpretations [116]. Our

simulations demonstrate a transitioning to a more complex and rich dynamical structure with a fascinating directional anisotropy that is very different from that in quasi-equilibrium conditions. Thus large-scale simulations, as presented in this work, would be of immense value in interpreting the state-of-the-art pump-probe experiments at ultra/hyperfast timescales [32, 33, 62, 157, 158].

Lastly, a fundamental understanding of the dynamical attributes of defect recovery is generally unknown; the various defect models currently in use do not account for the dynamical recovery. Insights garnered from our work, however, can be advantageously employed in developing realistic models for defect recovery. Although the structural aspects of tolerance of materials to radiation have been elucidated before [159, 160], the current work throws light on the incipient dynamical interactions that control the structural transformation in a radiation environment.

References

[1] G. S. Was, *Fundamentals of Radiation Materials Science*. New York: Springer, 2007.

[2] R. J. M. Konings (Ed.), *Comprehensive Nuclear Materials*. Elsevier, 2012.

[3] M. N. Ashfold, F. Claeyssens, G. M. Fuge, and S. J. Henley, "Pulsed laser ablation and deposition of thin films.," *Chem. Soc. Rev.,* vol. 33, p. 23, 2004.

[4] W. M. Steen, "Laser material processing - an overview," *J. Opt. A: Pure Opt.,* vol. 5, S3, 2003.

[5] J. G. Han, "Recent progress in thin film processing by magnetron sputtering with plasma diagnostics," *J. Phys. D: Appl. Phys,* p. 043001, 2009.

[6] S. Reyntjens and R. Puers, "A review of focused ion beam applications in microsystem technology," *J. Micromech. Microeng,* vol. 11, p. 287, 2001.

[7] L. B. Freund and S. Suresh, *Thin Film Materials: Stress, Defect Formation and Surface Evolution*. Cambridge: Cambridge University Press, 2003.

[8] "Basic Research Needs for Materials Under Extreme Environments," *Basic Energy Sciences Workshop Report,* 2007.

[9] "Basic Research Needs for Solar Energy Utilization," *Basic Energy Sciences Workshop Report,* 2005.

[10] C. E. Kennedy, "Review of Mid- to High- Temperature Solar Selective Absorber Materials," *Technical Report: NREL/TP-520-31267 - National Renewable Energy Laboratory,* 2002.

[11] T. Markvart, "Review: Radiation damage in solar cells," *J. Materials Science: Materials in Electronics,* vol. 1, p. 1, 1990.

[12] A. R. Peaker, V. P. Markevich, and L. Dobaczewski, "Recombination and radiation damage in crystalline silicon solar cell material," *Phys. Stat. Sol. (C),* vol. 1, p. 2274, 2004.

[13] W.-L. Chan, K. Zhao, N. Vo, Y. Ashkenazy, D. G. Cahill, and R. S. Averback, "Stress evolution in platinum thin films during low-energy ion irradiation," *Phys. Rev. B,* vol. 77, p. 205405, 2008.

[14] C. Anders, E. M. Bringa, G. Ziegenhain, G. A. Graham, J. F. Hansen, N. Park, N. E. Teslich, and H. M. Urbassek, "Why Nanoprojectiles Work Differently than Macroimpactors: The Role of Plastic Flow," *Phys. Rev. Lett.,* vol. 108, p. 027601, 2012.

[15] A. A. Correa, J. Kohanoff, E. Artacho, D. Sánchez-Portal, and A. Caro, "Nonadiabatic Forces in Ion-Solid Interactions: The Initial Stages of Radiation Damage," *Phys. Rev. Lett.,* vol. 108, p. 213201, 2012.

[16] L. V. Zhigilei, Z. Lin, and D. S. Ivanov, "Atomistic Modeling of Short Pulse Laser Ablation of Metals: Connections between Melting, Spallation, and Phase Explosion," *J. Phys. Chem. C,* vol. 113, p. 11892, 2009.

[17] M. Gill-Comeau and L. J. Lewis, "Ultrashort-pulse laser ablation of nanocrystalline aluminum," *Phys. Rev. B,* vol. 84, p. 224110, 2011.

[18] A. F. Calder, D. J. Bacon, A. V. Barashev, and Y. N. Osetsky, "On the origin of large interstitial clusters in displacement cascades," *Phil. Mag. ,* vol. 90, p. 863, 2010.

[19] J. Samela and K. Nordlund, "Atomistic Simulation of the Transition from Atomistic to Macroscopic Cratering," *Phys. Rev. Lett.,* vol. 101, p. 027601, 2008.

[20] E. M. Bringa and R. E. Johnson, "Coulomb Explosion and Thermal Spikes," *Phys. Rev. Lett.,* vol. 88, p. 165501, 2002.

[21] S. G. Mayr, Y. Ashkenazy, K. Albe, and R. S. Averback, "Mechanisms of Radiation-Induced Viscous Flow: Role of Point Defects," *Phys. Rev. Lett.,* vol. 90, p. 055505, 2003.

[22] S. G. Mayr and R. S. Averback, "Surface Smoothing of Rough Amorphous Films by Irradiation-Induced Viscous Flow," *Phys. Rev. Lett.,* vol. 87, p. 196106, 2001.

[23] D. S. Ivanov and L. V. Zhigilei, "Effect of Pressure Relaxation on the Mechanisms of Short-Pulse Laser Melting," *Phys. Rev. Lett.,* vol. 91, p. 105701, 2003.

[24] D. Perez and L. J. Lewis, "Ablation of Solids under Femtosecond Laser Pulses," *Phys. Rev. Lett.,* vol. 89, p. 255504, 2002.

[25] B. J. Demaske, V. V. Zhakhovsky, N. A. Inogamov, and I. I. Oleynik, "Ablation and spallation of gold films irradiated by ultrashort laser pulses," *Phys. Rev. B,* vol. 82, p. 064113, 2010.

[26] B. Chimier and V. T. Tikhonchuk, "Liquid-vapor phase transition and droplet formation by subpicosecond laser heating," *Phys. Rev. B,* vol. 79, p. 184107, 2009.

[27] P. Lorazo, L. J. Lewis, and M. Meunier, "Short-Pulse Laser Ablation of Solids: From Phase Explosion to Fragmentation," *Phys. Rev. Lett.,* vol. 91, p. 225502, 2003.

[28] M. E. Povarnitsyn, T. E. Itina, K. V. Khishchenko, and P. R. Levashov, "Suppression of Ablation in Femtosecond Double-Pulse Experiments," *Phys. Rev. Lett.,* vol. 103, p. 195002, 2009.

[29] W.-L. Chan, R. S. Averback, D. G. Cahill, and A. Lagoutchev, "Dynamics of femtosecond laser-induced melting of silver," *Phys. Rev. B,* vol. 78, p. 214107, 2008.

[30] Z. Lin, E. Leveugle, E. M. Bringa, and L. V. Zhigilei, "Molecular Dynamics Simulation of Laser Melting of Nanocrystalline Au†," *J. Phys. Chem. C,* vol. 114, p. 5686, 2009.

[31] "Basic Research Needs for Advanced Nuclear Energy Systems," *Basic Energy Sciences Workshop Report,* 2006.

[32] A. M. Lindenberg, S. Engemann, K. J. Gaffney, K. Sokolowski-Tinten, J. Larsson, P. B. Hillyard, D. A. Reis, D. M. Fritz, J. Arthur, R. A. Akre, M. J. George, A. Deb, P. H. Bucksbaum, J. Hajdu, D. A. Meyer, M. Nicoul, C. Blome, T. Tschentscher, A. L. Cavalieri, R. W. Falcone, S. H. Lee, R. Pahl, J. Rudati, P. H. Fuoss, A. J. Nelson, P. Krejcik, D. P. Siddons, P. Lorazo, and J. B. Hastings, " X-Ray Diffuse Scattering Measurements of Nucleation Dynamics at Femtosecond Resolution," *Phys. Rev. Lett.,* vol. 100, p. 135502, 2008.

[33] A. M. Lindenberg, J. Larsson, K. Sokolowski-Tinten, K. J. Gaffney, C. Blome, O. Synnergren, J. Sheppard, C. Caleman, A. G. MacPhee, D. Weinstein, D. P. Lowney, T. K. Allison, T. Matthews, R. W. Falcone, A. L. Cavalieri, D. M. Fritz, S. H. Lee, P. H. Bucksbaum, D. A. Reis, J. Rudati, P. H. Fuoss, C. C. Kao, D. P. Siddons, R. Pahl, J. Als-Nielson, S. Duerster, R. Ischebec, H. Schlarb, H. Schulte-Schrepping, T. Tschentscher, J. Schneider, D. v. d. Linde, O. Hignette, F. Sette, H. N. Chapman, R. W. Lee, T. N. Hansen, S. Techert, J. S. Wark, M. Bergh, G. Huldt, D. v. d. Spoel, N. Timneanu, J. Hajdu, R. A. Akre, E. Bong, P. Krejcik, J. Arthur, S. Brennan, L. K, and J. B. Hastings, "Atomic-scale visualization of inertial dynamics," *Science,* vol. 308, p. 392, 2005.

[34] F. Dorchies, A. Lévy, C. Goyon, P. Combis, D. Descamps, C. Fourment, M. Harmand, S. Hulin, P. M. Leguay, S. Petit, O. Peyrusse, and J. J. Santos, "Unraveling the Solid-Liquid-Vapor Phase Transition Dynamics at the Atomic Level with Ultrafast X-Ray Absorption Near-Edge Spectroscopy," *Phys. Rev. Lett.,* vol. 107, p. 245006, 2011.

[35] M. Beye, F. Sorgenfrei, W. F. Schlotter, W. Wurth, and A. Fohlisch, "The liquid-liquid phase transition in silicon revealed by snapshots of valence electrons," *Proc. Natl. Acad. Sci.,* vol. 107, p. 16772, 2010.

[36] D. S. Ivanov and L. V. Zhigilei, "Combined atomistic-continuum modeling of short-pulse laser melting and disintegration of metal films," *Phys. Rev. B,* vol. 68, p. 064114, 2003.

[37] D. S. Ivanov and L. V. Zhigilei, "Kinetic Limit of Heterogeneous Melting in Metals," *Phys. Rev. Lett.,* vol. 98, p. 195701, 2007.

[38] K. Nordlund, L. Wei, Y. Zhong, and R. S. Averback, "Role of electron-phonon coupling on collision cascade development in Ni, Pd, and Pt," *Phys. Rev. B,* vol. 57, R13965, 1998.

[39] D. M. Duffy and A. M. Rutherford, "Including the effects of electronic stopping and electron–ion interactions in radiation damage simulations," *J. Phys.: Condens. Matter,* vol. 19, p. 016207, 2007.

[40] T. D. de la Rubia, R. S. Averback, R. Benedek, and W. E. King, "Role of thermal spikes in energetic displacement cascades," *Phys. Rev. Lett.,* vol. 59, p. 1930, 1987.

[41] S. G. Mayr and R. S. Averback, "Effect of ion bombardment on stress in thin metal films," *Phys. Rev. B,* vol. 68, p. 214105, 2003.

[42] K. Nordlund, J. Keinonen, M. Ghaly, and R. S. Averback, "Coherent displacement of atoms during ion irradiation," *Nature,* vol. 398, p. 49, 1999.

[43] M. D. Ediger, "Spatially heterogeneous dynamics in supercooled liquids," *Annu. Rev. Phys. Chem.,* vol. 51, p. 99, 2000.

[44] D. J. Evans and G. P. Morriss, *Statistical mechanics of nonequilibrium liquids*, 2nd ed. Cambridge: Cambridge University Press, 2008.

[45] M. H. Peters, *Molecular thermodynamics and transport phenomena: Complexities of scales in space and time*: McGrwa-Hill, 2005.

[46] R. Balescu, *Equilibrium and nonequilibrium statistical mechanics*. New York: Wiley, 1975.

[47] J.-P. Hansen and I. R. McDonald, *Theory of simple liquids*, 3rd ed. Amsterdam ; Boston: Elsevier / Academic Press, 2007.

[48] D. Chandler, *Introduction to modern statistical mechanics*. New York: Oxford University Press, 1987.

[49] J. A. McLennan, *Introduction to non-equilibrium statistical mechanics*: Prentice-Hall, Inc., 1989.

[50] D. A. McQuarrie, *Statistical Mechanics* California: University Science Books, 2000.

[51] D. J. Evans and G. P. Morriss, *Statistical Mechanics of Non-equilibrium Liquids*. London: Academic Press, 1990.

[52] J. P. Boon and S. Yip, *Molecular Hydrodynamics*. New York: Dover, 1991.

[53] J.-P. Hansen and I. R. McDonald, "Theory of Simple Fluids," in *Theory of Simple Fluids*, ed London: Elsevier, 1986.

[54] J. M. Haile, *Molecular dynamics simulation : elementary methods*. New York: Wiley, 1992.

[55] D. C. Rapaport, *The art of molecular dynamics simulation*, 2nd ed. Cambridge, UK ; New York, NY: Cambridge University Press, 2004.

[56] L. Berthier and G. Biroli, "Theoretical perspective on the glass transition and amorphous materials," *Rev. Mod. Phys.,* vol. 83, p. 587, 2011.

[57] G. Biroli and J. P. Garrahan, "Perspective: The glass transition," *J. Chem. Phys.,* vol. 138, p. 12A301, 2013.

[58] D. Chandler and J. P. Garrahan, "Dynamics on the Way to Forming Glass: Bubbles in Space-Time," *Ann. Rev. Phys. Chem.,* vol. 61, p. 191, 2010.

[59] M. D. Ediger and P. Harrowell, "Perspective: Supercooled liquids and glasses," *J. Chem. Phys.,* vol. 137, p. 080901, 2012.

[60] P. Chaudhuri, L. Berthier, and W. Kob, "Universal Nature of Particle Displacements close to Glass and Jamming Transitions," *Phys. Rev. Lett.,* vol. 99, p. 060604, 2007.

[61] L. Berthier, G. Biroli, J.-P. Bouchaud, L. Cipelletti, and W. v. Saarlo, *Dynamical Heterogeneities in Glasses, Colloids, and Granular Media*: Oxford Scholarship Online, 2011.

[62] M. Beye, P. Wernet, C. Schüßler-Langeheine, and A. Föhlisch, "Time resolved resonant inelastic X-ray scattering: A supreme tool to understand dynamics in solids and molecules," *J. Elect. Spect. Phen.,* vol. 188, p. 172, 2013.

[63] X. Mei and J. Eapen, "Dynamic transitions in molecular dynamics simulations of supercooled silicon," *Phys. Rev. B,* vol. 87, p. 134206, 2013.

[64] B. L. Holian, M. Mareschal, and R. Ravelo, "Test of a new heat-flow equation for dense-fluid shock waves," *J. Chem. Phys.,* vol. 133, p. 114502, 2010.

[65] J. Eapen, J. Li, and S. Yip, "Statistical field estimators for multiscale simulations," *Phys. Rev. E,* vol. 72, p. 056712, 2005.

[66] H. J. M. Hanley, *Transport Phenomena in Fluids*. New York: Marcel Dekker, 1969.

[67] W. G. Hoover and C. G. Hoover, "Tensor temperature and shock-wave stability in a strong two-dimensional shock wave," *Phys. Rev. E,* vol. 80, p. 011128, 2009.

[68] H. M. Mott-Smith, "The Solution of the Boltzmann Equation for a Shock Wave," *Phys. Rev.,* vol. 82, p. 885, 1951.

[69] B. L. Holian and M. Mareschal, "Heat-flow equation motivated by the ideal-gas shock wave," *Phys. Rev. E,* vol. 82, p. 026707, 2010.

[70] B. L. Holian, M. Mareschal, and R. Ravelo, "Burnett-Cattaneo continuum theory for shock waves," *Phys. Rev. E,* vol. 83, p. 026703, 2011.

[71] W. G. Hoover and C. G. Hoover, "Well-posed two-temperature constitutive equations for stable dense fluid shock waves using molecular dynamics and generalizations of Navier-Stokes-Fourier continuum mechanics," *Phys. Rev. E,* vol. 81, p. 046302, 2010.

[72] D. C. Rapaport, *The Art of Molecular Dynamics Simulation, II ed.* Cambridge: Cambridge University Press, 2004.

[73] M. P. Allen and D. J. Tildesley, *Computer Simulation of Liquids*. Oxford: Oxford University Press, 2003.

[74] D. Frenkel and B. Smit, *Understanding Molecular Simulation*. New York: Academic Press, 2002.

[75] L. Verlet, "Computer "Experiments" on Classical Fluids. I. Thermodynamical Properties of Lennard-Jones Molecules," *Phys. Rev.,* vol. 159, p. 98, 1967.

[76] M. P. Allen and D. J. Tildesley, *Computer Simulations of Liquids*. Oxford: Clarendon Press, 1991.

[77] M. R. Fellinger, H. Park, and J. W. Wilkins, "Force matched embedded atom method potential for niobium," *Phys. Rev. B,* vol. 81, p. 144119, 2010.

[78] M. S. Daw and M. I. Baskes, "Semiempirical, quantum mechanical calculation of hydrogen embrittlement in metals," *Phys. Rev. Lett.,* vol. 50, p. 1285, 1983.

[79] F. H. Stillinger and T. A. Weber, "Computer simulation of local order in condensed phases of silicon," *Phys. Rev. B,* vol. 31, p. 5262, 1985.

[80] J. Q. Broughton and X. P. Li, "Phase diagram of silicon by molecular dynamics," *Phys. Rev. B,* vol. 35(17), p. 9120, 1987.

[81] Y. Kadiri, N. Jakse, J.-F. Wax, and J.-L. Bretonnet, "Structure factor and atomic dynamics of stable and supercooled liquid silicon by molecular dynamics," *J. Non. Cryst. Sol.,* vol. 312-314, p. 143, 2002.

[82] M. D. Kluge, J. R. Ray, and A. Rahman, "Amorphous-silicon formation by rapid quenching: A molecular-dynamics study," *Phys. Rev. B,* vol. 36, p. 4234, 1987.

[83] W. D. Luedtke and U. Landman, "Preparation and melting of amorphous silicon by molecular-dynamics simulations," *Phys. Rev. B,* vol. 37, p. 4656, 1988.

[84] S. Sastry and C. Austen Angell, "Liquid-liquid phase transition in supercooled silicon," *Nat. Mater.,* vol. 2, p. 739, 2003.

[85] N. Jakse and A. Pasturel, "Dynamics of liquid and undercooled silicon: an ab inito molecular dynamics study," *Phys. Rev. B,* vol. 79, p. 144206, 2009.

[86] A. Delisle, D. J. González, and M. J. Stott, "Structural and dynamical properties of liquid si: an orbital-free molecular dynamics study," *Phys. Rev. B,* vol. 73, p. 064202, 2006.

[87] P. Mitev, G. A. Evangelakis, and E. Kaxiras, "Embedded atom method potential: employing a faithful density representation," *Modelling Simul. Mater. Sci. Eng.,* vol. 14, p. 721, 2006.

[88] U. V. Waghmare, H. Kim, I. J. Park, N. Modine, P. Maragakis, and E. Kaxiras, "Hares: an efficient method for first principle electronic structure calculations of complex systems," *Phys. Commun.,* vol. 137, p. 341, 2001.

[89] D. G. Papageorgiou, I. N. Demetropoulos, and I. E. Lagaris, "MERLIN-3.0 A multidimensional optimization environment," *Comput. Phys. Commun.,* vol. 109, p. 227, 1998.

[90] J. B. Sturgeon and B. B. Laird, "Adjusting the melting point of a model system via gibbs-duhem integration: application to a model of aluminum," *Phys. Rev. B,* vol. 62, p. 14720, 2000.

[91] M. I. Mendelev, M. J. Kramer, C. A. Becker, and M. Asta, "Analysis of semi-empirical interatomic potentials appropriate for simulation of crystalline and liquid Al and Cu," *Phil. Mag.,* vol. 88, p. 1723, 2008.

[92] J. F. Ziegler, J. P. Biersack, and U. Littmark, *The stopping and range of ions in solids.* Oxford: Pergamon, 1985.

[93] R. Devanathan and W. J. Weber, "Simulation of collision cascades and thermal spikes in ceramics," *Nucl. Instr. Meth. Phys. Res. B,* vol. 268, p. 2857, 2010.

[94] N. Juslin, P. Erhart, P. Träskelin, J. Nord, K. O. E. Henriksson, K. Nordlund, E. Salonen, and K. Albe, "Analytical interatomic potential for modeling nonequilibrium processes in the W–C–H system," *Journal of Applied Physics,* vol. 98, p. 123520, 2005.

[95] A. Widmer-Cooper, P. Harrowell, and H. Fynewever, "How reproducible are dynamic heterogeneities in a supercooled liquid?," *Phys. Rev. Lett.,* vol. 93, p. 135701, 2004.

[96] M. S. Razul, G. S. Matharoo, and P. H. Poole, "Spatial correlation of the dynamic propensity of a glass-forming liquid," *J. Phys.: Condens. Matter,* vol. 23, p. 235103, 2011.

[97] A. Widmer-Cooper and P. Harrowell, "Predicting the long-time dynamic heterogeneity in a supercooled liquid on the basis of short-time heterogeneities," *Phys. Rev. Lett.,* vol. 96, p. 185701, 2006.

[98] A. Widmer-Cooper, H. Perry, P. Harrowell, and D. R. Reichman, "Irreversible reorganization in a supercooled liquid originates from localized soft modes," *Nat. Phys. Lett.,* vol. 4, p. 711, 2008.

[99] L. Berthier and R. L. Jack, "Structure and dynamics of glass formers: predictability at large length scales," *Phys. Rev. E,* vol. 76, p. 041509, 2007.

[100] A. Widmer-Cooper, H. Perry, P. Harrowell, and D. R. Reichman, "Localized soft modes and the supercooled liquid's irreversible passage through its configuration space," *J. Chem. Phys.,* vol. 131, p. 194508, 2009.

[101] A. Widmer-Cooper and P. Harowell, "On the way of collective dynamics in supercooled liquids through the statistics of the isoconfigurational ensemble," *J. Chem. Phys.,* vol. 126, p. 154503, 2007.

[102] A. Widmer-Cooper and P. Harrowell, "On the relationship between structure and dynamics in a supercooled liquid," *J. Phys.: Condens. Matter,* vol. 17, p. 4025, 2005.

[103] G. S. Matharoo, M. S. Razul, and P. H. Poole, "Structural and dynamical heterogeneity in a glass-forming liquid," *Phys. Rev. E,* vol. 74, p. 050502, 2006.

[104] S. Nose, "A unified formulation of the constant temperature molecular-dynamics methods," *J Chem. Phys.,* vol. 81, p. 151, 1984.

[105] W. G. Hoover, "Canonical dynamics: Equilibrium phase-space distributions," *Phys Rev A,* vol. 31, p. 1695, 1985.

[106] J. M. Thijssen, *Computational physics*: Cambridge University Press, 2007.

[107] A. Hedler, S. L. Klaumunzer, and W. Wesch, "Amorphous silicon exhibits a glass transition," *Nat. Mater.,* vol. 3, p. 804, 2004.

[108] P. H. Poole, T. Grande, C. A. Angell, and P. F. McMillan, "Polymorphic phase transitions in liquids and glasses," *Science,* vol. 275, p. 322, 1997.

[109] C. A. Angell, "Glass-formers and viscous liquid slow down since david turnbull: enduring puzzlesand new twists," *MRS Bulletin,* vol. 33, 2008.

[110] E. Rapoport, "Model for melting-curve maxima at high pressure," *J. Chem. Phys.,* vol. 46, p. 2891, 1967.

[111] Y. Katayama, T. Mizutani, W. Utsumi, O. Shimomura, M. Yamakata, and K. Funakoshi, "A first-order liquid-liquid phase transition in phosphorus," *Nature,* vol. 403, p. 170, 2000.

[112] G. N. Greaves, M. C. Wilding, S. Fearn, D. Langstaff, F. Kargl, S. Cox, Q. V. Van, O. Majerus, C. J. Benmore, R. Weber, C. M. Martin, and L. Hennet, "Detection of first-order liquid/liquid phase transitions in yttrium oxide-aluminum oxide melts," *Science,* vol. 322, p. 566, 2008.

[113] F. Mallamace, M. Broccio, C. Corsaro, A. Faraone, D. Majolino, V. Venuti, L. Liu, C. Y. Mou, and S. H. Chen, "Evidence of the existence of the low-density liquid phase in supercooled, confined water," *Proc Natl Acad Sci U S A,* vol. 104, p. 424, 2007.

[114] C. Huang, K. T. Wikfeldt, T. Tokushima, and D. Nordlund, "The inhomogeneous structure of water at ambient conditions," *Proc. Nat. Acad. Sci.,* vol. 106, p. 15214, 2009.

[115] F. Mallamace, "The liquid water polymorphism," *Proc. Natl. Acad. Sci.,* vol. 106, p. 15097, 2009.

[116] S. Sastry, "Illuminating liquid polymorphism in silicon," *Proc. Natl. Acad. Sci.,* vol. 107, p. 17063, 2010.

[117] T. E. Angelini, E. Hannezo, X. Trepat, M. Marquez, J. J. Fredberg, and D. A. Weitz, "Glass-like dynamics of collective cell migration," *Proc. Natl. Acad. Sci.,* vol. 108, p. 4714, 2011.

[118] J. P. Garrahan, "Dynamic heterogeneity comes to life," *Proc. Nat. Acad. Sci.,* vol. 108, p. 4701, 2011.

[119] T. H. Kim, G. W. Lee, B. Sieve, A. K. Gangopadhyay, R. W. Hyers, T. J. Rathz, J. R. Rogers, D. S. Robinson, K. F. Kelton, and A. I. Goldman, "In situ high-energy x-ray diffraction study of the local structure of supercooled liquid Si," *Phys. Rev. Lett.,* vol. 95, p. 085501, 2005.

[120] K. Higuchi, K. Kimura, A. Mizuno, M. Watanabe, Y. Katayama, and K. Kuribayashi, "Precise measurement of density and structure of undercooled molten silicon by using synchrotron radiation combined with electromagnetic levitation technique," *Meas. Sci. and Tech.,* vol. 16, p. 381, 2005.

[121] H. Kimura, M. Watanabe, K. Izumi, and T. Hibiya, "X-ray diffraction study of undercooled molten silicon," *App. Phys. Lett.,* vol. 78, p. 604, 2001.

[122] N. Jakse, L. Hennet, D. L. Price, S. Krishnan, T. Key, E. Artacho, B. Glorieux, A. Pasturel, and M.-L. Saboungi, "Structural changes on supercooling liquid silicon," *App. Phys. Lett.,* vol. 83, p. 4734, 2003.

[123] S. Ansell, S. Krishnan, J. J. Felten, and D. L. Price, "Structure of supercooled liquid silicon," *Phys.: Condens. Matter,* vol. 10, p. 73, 1998.

[124] J. T. Okada, P. H. Sit, Y. Watanabe, Y. J. Wang, B. Barbiellini, T. Ishikawa, M. Itou, Y. Sakurai, A. Bansil, R. Ishikawa, M. Hamaishi, T. Masaki, P. F. Paradis, K. Kimura, and S. Nanao, "Persistence of covalent bonding in liquid silicon probed by inelastic x-ray scattering," *Phys. Rev. Lett.,* vol. 108, p. 067402, 2012.

[125] V. V. Vasisht, S. Saw, and S. Sastry, "Silicon in silico," *Nat. Phys.,* vol. 7, p. 549, 2011.

[126] N. Jakse and A. Pasturel, "Liquid-liquid phase transformation in silicon: evidence from first-principles molecular dynamics simulations," *Phys. Rev. Lett.,* vol. 99, p. 205702, 2007.

[127] P. Ganesh and M. Widom, "Liquid-liquid transition in supercooled silicon determined by first-principles simulation," *Phys. Rev. Lett.,* vol. 102, p. 075701, 2009.

[128] F. Mallamace, C. Branca, C. Corsaro, N. Leone, J. Spooren, S.-H. Chen, and H. E. Stanley, "Transport properties of glass-forming liquids suggestthat dynamic crossover temperature is as importantas the glass transition temperature," *Proc. Nat. Acad. Sci.,* vol. 107, p. 22457, 2010.

[129] W. Kob, "Computer simulations of supercooled liquids and glasses," *J. Phys.: Condens. Matter,* vol. 11, R85, 1999.

[130] K. N. Lad, N. Jakse, and A. Pasturel, "Signatures of fragile-to-strong transition in a binary metallic glass-forming liquid," *J. Chem. Phys.,* vol. 136, p. 104509, 2012.

[131] C. A. Angell, "Formation of Glasses from Liquids and Biopolymers," *Science,* vol. 267, p. 1924, 1995.

[132] S. A. Kivelson and G. Tarjus, "In search of a theory of supercooled liquids," *Nat Mater,* vol. 7, p. 831, 2008.

[133] W. Götze, *Complex dynamics of glass-forming liquids: a mode-coupling theory*. New York: Oxford University Press, 2009.

[134] P. Scheidler, W. Kob, A.Latz, J. Horbach, and K. Binder, "Frequency-dependent specific heat of viscous silica," *Phys. Rev. B,* vol. 63, p. 104204, 2001.

[135] H. Sasaki, E. Tokizaki, X. M. Huang, K. Terashima, and S. Kimura, "Temperature dependence of the viscosity of molten silicon measured by the oscillating cup method," *Jpn. J. Appl. Phys.,* vol. 34, p. 3432, 1995.

[136] Y. Sato, Y. Kameda, T. Nagasawa, T. Sakamoto, S. Moriguchi, T. Yamamura, and Y. Waseda, "Viscosity of molten silicon and the factors affecting measurement," *J. Cryst. Growth,* vol. 249, p. 404, 2003.

[137] K. Kakimoto, M. Eguchi, H. Watanabe, and T. Hibiya, "Natural and forced convection of molten silicon during czochralski single crystal growth," *J. Cryst. Growth,* vol. 94, p. 412, 1989.

[138] W.-K. Rhim and K. Ohsaka, "Thermophysical properties measurement of molten silicon by high-temperature electrostatic levitator: density, volume expansion, specific heat capacity, emissivity, surface tension and viscosity," *J. Cryst. Growth,* vol. 208, p. 313, 2000.

[139] H. R. Wendt and F. F. Abraham, "Empirical criterion for the glass transition region based on monte carlo simulations," *Phys. Rev. Lett.,* vol. 41, p. 1244, 1978.

[140] Z. Y. Hou, L. X. Liu, Z. A. Tian, R. S. Liu, Y. Shu, and J. G. Wang, "Atomic mechanism of liquid-glass transition for Ca_7Mg_3 alloy," *J. Phys. Chem. B,* vol. 116, p. 7746, 2012.

[141] B. V. R. Tata and S. S. Jena, "Ordering, dynamics and phase transitions in charged colloids," *Solid State Comm.,* vol. 139, p. 562, 2006.

[142] Y. Zhang, L. Wang, and W. Wang, "Thermodynamic, dynamic and structural relaxation in supercooled liquid and glassy Ni below the critical temperature," *J. Phys.: Condens. Matter,* vol. 19, p. 196106, 2007.

[143] G. Duan, D. Xu, Q. Zhang, and G. Zhang, "Molecular dynamics study of the binary $Cu_{46}Zr_{54}$ metallic glass motivated by experiments: glass formation and atomic-level structure," *Phys. Rev. B,* vol. 71, p. 224208, 2005.

[144] Y. Benin, K. Hirao, and N. Soga, "Evaluation of structural inhomogeneity by molecular dynamics method. structural variation of silica glass," *J. Non-Crystal. Solids,* vol. 183, p. 22, 1995.

[145] S. Sanyal and A. K. Sood, "Brownian dynamics simulation of dense binary colloidal mixtures. I. Structural evolution and dynamics," *Phys. Rev. E,* vol. 52, p. 4154, 1995.

[146] N. Jakse and A. Pasturel, "Dynamic aspects of the liquid-liquid phase transformation in silicon," *J. Chem. Phys.,* vol. 129, p. 104503, 2008.

[147] A. Annamareddy, X. Mei, W. Mohamed, and J. Eapen, "(Unpublished)."

[148] M. I. Mendelex, M. J. Kramer, C. A. Becker, and M. Asta, "Analysis of semi-empirical interatomic potentials appropriate for simulation of crystalline and liquid Al and Cu," *Phil. Mag.,* vol. 88, No. 12, p. 1723, 2008.

[149] R. G. Palmer, D. L. Stein, E. Abrahams, and P. W. Anderson, "Models of Hierarchically Constrained Dynamics for Glassy Relaxation," *Phys. Rev. Lett.,* vol. 53, p. 958, 1984.

[150] O. B. Tsiok, V. A. Sidorov, V. V. Bredikhin, L. G. Khvostantsev, V. N. Troitskiy, and L. I. Trusov, "Relaxation effects during the densification of ultrafine powders at high hydrostatic pressure," *Phys. Rev. B,* vol. 51, p. 12127, 1995.

[151] H. M. Jaeger, C.-H. Liu, and S. R. Nagel, "Relaxation at the Angle of Repose," *Phys. Rev. Lett.,* vol. 62, p. 40, 1989.

[152] O. B. Tsiok, V. V. Brazhkin, A. G. Lyapin, and L. G. Khvostantsev, "Logarithmic Kinetics of the Amorphous-Amorphous Transformations in SiO_2 and GeO_2 Glasses under High Pressure," *Phys. Rev. Lett.,* vol. 80, p. 999, 1998.

[153] J. J. Brey and A. Prados, "Slow logarithmic relaxation in models with hierarchically constrained dynamics," *Phys. Rev. E,* vol. 63, p. 021108, 2001.

[154] B. L. Holian and P. S. Lomdahl, "Plasticity Induced by Shock Waves in Nonequilibrium Molecular-Dynamics Simulations," *Science,* vol. 280, p. 2085, 1998.

[155] W. Kob and H. C. Andersen, "Testing mode-coupling theory for a supercooled binary Lennard-Jones mixture I: The van Hove correlation function," *Phys. Rev. E,* vol. 51, p. 4626, 1995.

[156] M. D. Ediger, "Spatialy Heterogeneous Dynamics in Supercooled Liquids," *Ann. Rev. Phys. Chem.,* vol. 51, p. 99, 2000.

[157] Y. M. Sheu, S. H. Lee, J. K. Wahlstrand, D. A. Walko, E. C. Landahl, D. A. Arms, M. Reason, R. S. Goldman, and D. A. Reis, "Thermal transport in a semiconductor heterostructure measured by time-resolved x-ray diffraction," *Phys. Rev. B,* vol. 78, p. 045317, 2008.

[158] D. A. Reis and A. M. Lindenberg, "Ultrafast x-ray scattering in solids," *Light Scattering in Solids IX, Topics in Applied Physics,* vol. 108, p. 371, 2007.

[159] K. E. Sickafus, R. W. Grimes, J. A. Valdez, A. Cleave, M. Tang, M. Ishimaru, S. M. Corish, C. R. Stanek, and B. P. Uberuaga, "Radiation-induced amorphization resistance and radiation tolerance in structurally related oxides," *Nature Mater.,* vol. 6, p. 217, 2007.

[160] A. Chartier, C. Meis, J.-P. Crocombette, W. J. Weber, and L. R. Corrales, "Molecular Dynamic Simulation of Disorder Induced Amorphization in Pyrochlores," *Phys. Rev. Lett.,* vol. 94, p. 025505, 2005.